



Parametric modelling of shrinkage effects on industrial floors

David Klusener
MSc Thesis, Civil Engineering
June, 2020

MSc Thesis Report
Master Civil Engineering, Building Engineering, Structural Design

Parametric modelling of shrinkage effects on industrial floors

By

D.L. (David) Klusener

in partial fulfilment of the requirements for the degree of

Master of Science

in Civil Engineering

at the Delft University of Technology,

to be defended publicly on Friday June 19, 2020 at 10:00 AM.

Thesis committee:	Prof. Ir. R. Nijse	TU Delft
	Ir. S. Pasterkamp	TU Delft
	F. Messali	TU Delft
	Ing. N. Loonen	ABT BV

An electronic version of this thesis is available at <http://repository.tudelft.nl/>.



Abstract

Drying shrinkage can cause structural damage to concrete industrial floors. Shrinkage is caused by evaporation of moisture from the drying material. In the design- and construction-standards, this complex process is not described on a fundamental level. Using finite element modelling to simulate the flow of moisture through the concrete, it is possible to simulate drying shrinkage. The research question of this thesis is: 'How can a parametric FEM model efficiently simulate drying shrinkage in industrial concrete floors?'.
Verification of the produced model is performed. The outcome is compared to shrinkage measurements of concrete prisms.

The theoretical framework presented in this thesis is based on the fact that the relative pore humidity is changing during drying. In a finite element model, the changing relative pore humidity (pore-RH) over time is calculated. Drying is caused by internal diffusion of moisture, which is driven by differences in concentration. The moisture flow is modelled using the transient heat equation. The resulting pore-RH values are used to determine the hydrostatic capillary pressure based on the equations of Kelvin and Laplace. The material response of cement paste subjected to the capillary pressure is calculated using Bentz law. At last, the models of Pickett and Neville are used to include the restraining effect of aggregates and determine the absolute deformation of concrete subjected to drying. The initial conditions of the material are determined based on HYMOSTRUC cement simulation and Powers' volumetric model.

The results of the presented theoretical framework are reasonable. Usage of the framework and the heat equation for modelling drying in FEM, proved to be successful.

A significant uncertainty is found in the restraining effect of aggregates. The theoretical model is based on material modelling of drying cement paste. However, the deformation of concrete is only 16%~23% of the total deformation of cement paste. Recommended is to further research the (local) effect of aggregates on drying shrinkage.

Drying shrinkage has been calculated according to the construction standards and compared to the measured drying shrinkage of the concrete prisms. From this, it can be concluded that calculations by structural engineers on drying shrinkage are preferably done according to the 'Model code 2010'.

Preface

An interesting research into the fundamentals of concrete has led to a theoretical framework capable of simulating drying shrinkage. The report is constructed of a main body and appendices. The appendices support the main body by theoretical substantiation.

It has been an interesting journey through concrete theory, material fundamentals and lots of finite element simulations. For their loyal support and guidance I would like to thank my graduation committee, existing of the chair Prof.ir. R. Nijse, ir. S. Pasterkamp and F. Messali from Delft University of Technology and Ing. N. Loonen from ABT BV. Furthermore, I want to thank ABT for offering a graduation position.

This work would not have been possible without the additional support of Prof. G. Ye on micromechanical modelling of cement. Thanks for the support of PhD J. Chen in cement hydration simulation, PhD R. Mors and E. Rossi for sharing their expertise on shrinkage.

From ABT, I would like to thank ing. N. Loonen and ing. M. Menting for sharing their knowledge on concrete structures and cement technology. Ir. K. Riemens and dr.ir. L.J. van der Meer for their help on FEM simulations and C. Smulders for her tips on programming.

My fellow ABT graduates, I want to thank you for your support and help during the daily coffee breaks, so thank you ir. Y. Paauwe, G. Hoogerwaard, A. Aarts and J. Feij.

Lastly, I want to thank my family and friends for their support.

Enjoy reading the report

David Klusener

07-06-2020, Rotterdam

Table of content

Abstract.....	3
Preface	4
Table of content.....	6
List of figures and tables.....	8
1 Introduction	11
1.1 Shrinkage of industrial floors.....	12
2 Theory of drying	14
2.1 The scale of drying	15
2.2 Physics of drying	16
2.3 Method of Kelvin – Laplace	19
2.3.1 Kelvin equation.....	19
2.3.2 Laplace equation.....	21
2.4 Bentsz deformation law.....	23
2.4.1 Powers’ volumetric model.....	24
2.4.2 Degree of hydration.....	26
2.4.3 Bulk modulus of the system	27
2.5 Drying shrinkage at equilibrium.....	28
2.6 Diffusion.....	29
2.6.1 Fick’s 2 nd law – diffusion	30
2.6.2 Fick’s 1 st law - flux	32
3 Finite element modelling	33
3.1 Model setup	33
3.1.1 Finite elements	34
3.1.2 Mesh size.....	34
3.2 Equations used.....	36
3.2.1 Method of solving: Transient Heat Analysis.....	37
3.3 Finite element results.....	38
3.3.1 Drying in FE simulation	38
3.3.2 Drying shrinkage strain.....	41
3.3.2 Boundary flux	43
4 Discussion of results.....	45
5 Conclusions and recommendations	49
5.1 Conclusions.....	49
5.2 Recommendations	50
6 References	51
7 Appendix.....	57
Appendix I: Response of materials	57
I.1 Cement.....	57
I.2 Shrinkage.....	61

I.3 Swelling of young hardening concrete	66
I.4 Creep.....	67
I.5 Relaxation	68
I.6 Mitigation methods for shrinkage in reinforced concrete	71
I.7 Concluding remarks on response of materials	81
Appendix II: Codes & Structural conditions.....	82
II.1 Eurocode 2 and Model code 2010	82
II.2 Structural conditions.....	83
II.3 Shrinkage calculation based on the Eurocode 2	85
II.4 Shrinkage calculation based on the Mode code 2010.....	86
II.5 Concluding remarks on Codes & Structural conditions	88
Appendix A.....	89
Appendix B.....	90
Appendix C.....	92
Appendix D	98
Appendix E.....	100
Appendix F	101
Appendix G	102
Appendix H.....	104
Appendix I	106
Appendix J	107

List of figures and tables

FIGURE 1. A) MOISTURE CONTAINING ELEMENTS IN HARDENED CEMENT PASTE. B) SCHEMATIZATION OF SURFACE TENSION IN THE ABSORPTION LAYER (VERVOORT, 2015).	16
FIGURE 2. DISJOINING PRESSURE DISTRIBUTION ALONG A SURFACE OF HINDERED ABSORPTION. TAKEN FROM (LURA, 2003) BASED ON (SOROKA, 1979).	17
FIGURE 3. FLOWCHART USED TO MODEL THE DRYING OF CONCRETE.	18
FIGURE 4. A) MICROSTRUCTURE OF CEMENT PASTE. B) CYLINDRICAL CAPILLARY PORE (LU, 2019).....	19
FIGURE 5. ILLUSTRATIVE FIGURE OF TWO DIMENSIONAL MOISTURE LOSS IN A PORE (L. LIU ET AL., 2016).	20
FIGURE 6. EQUILIBRIUM INTERFACE AT WATER-AIR MENISCUS (PARK ET AL., 2011).	21
FIGURE 7. RADII AND CONTACT ANGLE OF (A) MERCURY-GAS AND (B) WATER-GAS INTERFACES (PICHLER ET AL., 2007)	21
FIGURE 8. RADIUS OF THE WATER-AIR MENISCUS TO KELVIN-LAPLACE.....	22
FIGURE 9. CAPILLARY PRESSURE RELATED TO RADIUS OF PORE.	22
FIGURE 10. POWERS' MODEL.	25
FIGURE 11. VISUALISATION OF PARTICLES IN YOUNG CEMENT PASTE. IMAGING PERFORMED IN PARAVIEW, BASED ON HYMOSTRUC DATA. LEFT) PARTICLE DISTRIBUTION. RIGHT) CAPILLARY WATER.	26
FIGURE 12. DIFFUSION COEFFICIENT FOR CONCRETE OF DIFFERENT W/C-RATIO'S (HOLMES & WEST, 2003).	29
FIGURE 13. DIFFUSION COEFFICIENT USED IN FICK'S 2 ND LAW. BASED ON THE MODEL CODE 2010 AND FROM STUDIES OF KANG ET AL. FOR W/C=0.50 AND DRYING AT 20°C.....	31
FIGURE 14. LEFT) TWENTY-NODE SOLID BRICK ELEMENT. RIGHT) FOUR-NODE POTENTIAL FLOW BOUNDARY ELEMENT	34
FIGURE 15. MESH DISTRIBUTION OF TEST BEAM MODEL AND ASSOCIATED SLICE MODEL.	35
FIGURE 16. INTERNAL RELATIVE HUMIDITY OF CONCRETE PORE DURING DRYING BASED ON THE FEM MODEL. TIME PERIOD 28 DAYS – 112 DAYS AND $RH_{EXTERNAL}=65\%$	38
FIGURE 17. INTERNAL RELATIVE HUMIDITY OF CONCRETE PORES DURING DRYING, BASED ON FEM MODEL. TIME PERIOD 28 DAYS - 10 YEARS AND $RH_{EXTERNAL}=65\%$	39
FIGURE 18. INTERNAL RELATIVE HUMIDITY OF CONCRETE PORES DURING DRYING, BASED ON FEM MODEL. TIME PERIOD 28 DAYS - 112 DAYS AND $RH_{EXTERNAL}=50\%$	40
FIGURE 19. INTERNAL RELATIVE HUMIDITY OF CONCRETE PORES DURING DRYING, BASED ON FEM MODEL. TIME PERIOD 28 DAYS - 10 YEARS AND $RH_{EXTERNAL}=50\%$	40
FIGURE 20. DRYING SHRINKAGE STRAIN OF CEMENT PASTE AND CONCRETE. 112-DAYS FOR $RH_{EXTERNAL}=65\%$ AND $RH_{EXTERNAL}=50\%$. 41	
FIGURE 21. NORMALISED DRYING SHRINKAGE OF CONCRETE. $RH_{EXTERNAL}=65\%$	42
FIGURE 22. DRYING SHRINKAGE STRAIN OF CEMENT PASTE AND CONCRETE. 10-YEARS FOR $RH_{EXTERNAL}=65\%$ AND $RH_{EXTERNAL}=50\%$. 42	
FIGURE 23. AVERAGE MOISTURE FLUX AT THE CONCRETE SURFACE DURING DRYING. $RH_{EXTERNAL}=65\%$	43
FIGURE 24. AVERAGE MOISTURE FLUX AT THE CONCRETE SURFACE DURING THE FIRST 48 HOURS OF DRYING. $RH_{EXTERNAL}=65\%$	43
FIGURE 25. CHANGE OF WEIGHT OVER A TIME PERIOD OF 10 YEARS. CONCRETE EXPOSED TO $RH_{EXTERNAL}=65\%$	44
FIGURE 26. SHRINKAGE STRAIN PLOTTED AGAINST CHANGE IN WEIGHT BASED ON FEM RESULTS.	45
FIGURE 27. FEM RESULT AND SHRINKAGE MEASUREMENT OF THE TEST BEAMS.	46
FIGURE 28. FEM RESULTS OF CEMENT PASTE AND CONCRETE WITH DIFFERENT LEVELS OF AGGREGATE RESTRAINT.	47
FIGURE 29. CONCRETE DRYING SHRINKAGE OF THE DEVELOPED MODELS, THE MEASURED STRAIN AND THE DESIGN CODES.	47
FIGURE 30. HYDRATED CEMENT PARTICLES IN CONCRETE. (SOURCE: BETONLEXICON.NL)	57
FIGURE 31. HEAT EVOLUTION OF HYDRATING CEMENT PASTE (VAZQUEZ & PIQUE, 2016).....	59
FIGURE 32. STAGES OF HYDRATION OF A SINGLE CEMENT GRAIN (DOMONE & ILLSTON, 2010)	60
FIGURE 33. TYPES OF SHRINKAGE.	61
FIGURE 34. SHRINKAGE TYPES DEVELOPING OVER TIME. LOW-MEDIUM STRENGTH CONCRETE (A) AND HIGH STRENGTH CONCRETE (B) (KENJI SAKATA & SHIMOMURA, 2004).	62
FIGURE 35. ILLUSTRATION OF PLASTIC SHRINKAGE (DOMONE & ILLSTON, 2010).	62
FIGURE 36. AUTOGENOUS SHRINKAGE CAUSED BY HYDRATION OF CEMENT.	63
FIGURE 37. SHRINKAGE ACCORDING THE EUROCODE FOR C35/45. (TIBERTI, MINELLI, & PLIZZARI, 2015)	64
FIGURE 38. DISTRIBUTION OF DRYING SHRINKAGE OVER THE CROSS SECTION OF A 200MM THICK CONCRETE SLAB. (HEATH & ROESLER, 1999).....	65
FIGURE 39. CURLING EFFECT.....	65

FIGURE 40. CRACK DUE TO CURLING.....	65
FIGURE 41. REPRESENTATION OF MEASURED STRAINS (WITTMANN, 1982) COMPARED TO DRYING SHRINKAGE STRAIN AND BASIC CREEP.....	67
FIGURE 42. CREEP AND RELAXATION.	68
FIGURE 43. STRESSES IN A RESTRAINED CONCRETE MEMBER. A) STRESS DEVELOPMENT AND B) CONCEPTUAL DESCRIPTION OF RELAXATION. (GRIBNIAK, KAKLAUSKAS, & BACINSKAS, 2008)(WEISS, 1999).....	69
FIGURE 44. RELAXATION OF RESTRAINED TENSILE STRESSES IN PORTLAND CEMENT AND BLAST FURNACE CEMENT (VERVOORT, 2015).	70
FIGURE 45. INTERNAL RELATIVE HUMIDITY FOR PORTLAND AND BFS CEMENT PASTE (LURA, 2003).	72
FIGURE 46. EFFECT OF THE BLAINE SPECIFIC SURFACE VALUE. A) RH (%) B) AUTOGENOUS MICROSTRAIN (MM/M) (L. WU ET AL., 2017).....	72
FIGURE 47. SHEAR-KEY FORCE EFFECT. (NARIN & WIKLUND, 2012)	75
FIGURE 48. BEKEART FIBRES. PULL-OUT TENSION. (RCR INDUSTRIAL FLOORING, 2019)	76
FIGURE 49. A) EFFECT OF STEEL FIBRES ON HARDENED CONCRETE (CUR - COMMISSIE STAALVEZELBETON, 2012) B) EFFECT OF STEEL FIBRES IN MACRO-, AND MICROCRACKING.	76
FIGURE 50. CMOD GRAPH SHOWING TENSION SOFTENING MATERIAL BEHAVIOUR. (CUR - COMMISSIE STAALVEZELBETON, 2012) 77	
FIGURE 51. A) CEMENT PASTE WITH 6 MM GLASS SPHERICAL INCLUSIONS. MICROCRACKING IN RADIAL DIRECTION AND AT THE SPHERE SURFACE. (BISSCHOP & MIER, 2002)(IDIART, 2006) B) INTERFACIAL TRANSITION ZONE SEEN THROUGH A FIELD EMISSION SCANNING ELECTRON MICROSCOPE (FE-SEM) C) GAP IS SEEN BETWEEN THE AGGREGATE AND THE CEMENT MATRIX. (R. LIU ET AL., 2019).....	78
FIGURE 52. SECTION OF INDUSTRIAL FLOOR. (A) SLAB-ON-PILE (B) SLAB-ON-GRADE.....	80
FIGURE 53. INTERFACE STRESSES BETWEEN CONCRETE SLAB AND SUBGRADE (WIMSATT, MCCULLOUGH, & BURNS, 1987).	80
FIGURE 54. DIMENSION OF THE CONCRETE PRISM.	83
FIGURE 55. SHRINKAGE STRAIN OF CONCRETE PRISM. ACCORDING TO THE EUROCODE (NEN, 2011).	86
FIGURE 56. SHRINKAGE STRAIN OF CONCRETE PRISM. CALCULATED USING THE MODEL CODE 2010 AND THE EUROCODE 2.....	87
FIGURE 57. CRACKS IN JOINTLESS CONCRETE FLOOR, ORIGINATING FROM SHRINKAGE.	89
FIGURE 58. WORLD'S GROWTH OF MINERALS AND MANUFACTURING PRODUCTS (1970=1) (UNEP; WMO, 2014).	90
FIGURE 59. GREENHOUSE GAS EMISSIONS PER INDUSTRY. (1970-2010) (UNEP; WMO, 2014).	91
FIGURE 60. A VOLUME V BOUNDED BY THE SURFACE S AND THE SURFACE NORMAL N.	92
FIGURE 61. CROSS-SECTIONAL DISTRIBUTION OF TEMPERATURE OR MOISTURE DUE TO DIFFUSION OVER TIME.....	95
FIGURE 62. FLUX DUE TO DIFFERENCES IN CONCENTRATION	96
FIGURE 63. FINITE DIFFERENCE METHOD FOR NUMERICAL ANALYSIS	101
FIGURE 64. MESH OPTIMISATION.	102
FIGURE 65. T=1 HOUR	103
FIGURE 66. T=7 DAYS.....	103
FIGURE 67. T=28 DAYS	103
FIGURE 68. T=112 DAYS	103
FIGURE 69. TEMPERATURE DISTRIBUTION AT CROSS-SECTIONAL NODES. THE NODES ARE LOCATED ON THE STRAIGHT SECTION-CUT AS SEEN IN FIGURE 71 (TOP).....	104
FIGURE 70. TEMPERATURE DISTRIBUTION AT MEAN NODES ON CROSS-SECTIONS.	104
FIGURE 71. POSITION OF NODES ON THE STRAIGHT- AND DIAGONAL-CROSS-SECTION. TOP) ALL NODES ON THE CUTTING-PLANE, MIDDLE ELEMENT ON THE PLANE IS USED. BOTTOM) POSITION OF THE FOUR MEAN NODES USED TO ILLUSTRATE THE MEAN DISTRIBUTION OF RELATIVE HUMIDITY THROUGH THE CROSS SECTION. THE GENERAL AVERAGE RH OF THE CROSS SECTION IS THE AVERAGE OF THE TWO MEAN NODES 230964 AND 226558. THIS VALUES IS USED TO CALCULATED THE DRYING SHRINKAGE STRAIN OVER TIME.	105
TABLE 1. MULTI-SCALE MODELLING (E. KOENDERS, 2015).	15
TABLE 2. MULTI-SCALE APPROACH OF CEMENTITIOUS MATERIALS.	15
TABLE 3. CATEGORIZATION OF PORES IN HYDRATED CEMENT PASTE (JENNINGS, 2004) AND AS USED BY G. YE (YE, 2003).	17
TABLE 4. MESH SIZE OF FEM MODEL.	35
TABLE 5. DRYING SHRINKAGE AT THE 112TH DAY. AFTER 28-DAYS OF SEALED HYDRATION AND 84-DAYS OF DRYING.	48
TABLE 6. CEMENT NOMENCLATURE (DOMONE & ILLSTON, 2010)(L. WU ET AL., 2017).	58

TABLE 7. VALUES OF SHRINKAGE IN CONCRETE. PRISMS WITH A SQUARED CROSS SECTION OF 127MM ² , EXPOSED TO 50% RH AT A TEMPERATURE OF 21 °C. (NEVILLE & BROOKS, 1991)	79
TABLE 8. PARAMETERS FOR EUROCODE SHRINKAGE STRAIN CALCULATION.	83
TABLE 9. CONCRETE MIX DESIGN ABT PRISMS.	84
TABLE 10. COORDINATES OF MEAN NODES USED FOR RH-DISTRIBUTION.	107

1 Introduction

Concrete industrial floors can be found in almost every distribution and warehouse facility. These floors are heavily loaded by distributed loads and point loads caused by storage racking. For logistic vehicles in a warehouse, a flat surface of the floor is needed. These requirements combined require a required floor that is strong and durable.

A cast-in-situ jointless reinforced concrete floor is often the preferred construction type to avoid local deterioration of the floor slab. Consequently, the area subject to shrinkage is larger. Hence, the effect of shrinkage increases in this construction type, compared to floors with dilatation joints.

Time- and stress-dependent responses of a concrete structure can cause the following deformations:

- Due to drying over time, the material can deform caused by shrinkage. This is a time-dependent response.
- By (external) loading a structure, it will deform proportional to the stiffness of the material. This is a stress-dependent response.
- Prolonged loading will cause creep and relaxation, these effect are both time- and stress dependent.

Shrinkage is the predominant time-dependent phenomena in concrete structures. Shrinkage is a volume change over time. This form of structural deformation on micro-, and macroscopic scale can lead to unwanted crack formations and loss of water tightness. Repair works on shrinkage induced cracks is costly and therefore preferable avoided by logistic real estate owners.

Reduction in volume over time is the result of multiple mechanisms. Beside shrinkage, the other concrete time-dependent mechanisms are creep and relaxation. Focus in this study is on shrinkage. The here-mentioned other structural and material effects are addressed in brief.

This research focusses on industrial jointless concrete slab floors. These cast-in situ floors are poured on a granulate subbase working floor. These type of flooring is well known by ABT BV.; in their annual order repertoire several projects on industrial floors are present. These projects can be in the nature of advising, engineering or inspection (Adviesgroep Civiele Techniek, ABT, 2015).

The goal of this master thesis is to improve the design of industrial floors, compared to the normative design code, the Eurocode. This is done by incorporating the effects of shrinkage better into the design by using the possibilities of numerical analysis of the finite element software DIANA and compare the outcomes with the current used analytical models.

The main research question is formulated as:

[How can a parametric FEM model efficiently simulate drying shrinkage in industrial concrete floors?](#)

To answer this research question, a theoretical understanding of shrinkage is gained and a modelling strategy for finite element modelling is developed. All the essential modelling theory is covered in chapter [2 'Theory of drying'](#) and chapter [3 'Finite element modelling'](#), discussion of the results is found in chapter [4 'Discussion of results'](#).

The theoretical background of shrinkage is introduced in [1.1 Shrinkage of industrial floors](#) and substantiated in [Appendix I: Response of materials](#). Where after the construction standards and structural conditions are covered in [Appendix II: Codes & Structural conditions](#).

1.1 Shrinkage of industrial floors

Industrial floors are large areas of thin slabs on a continuous support (slab-on-grade) or supported on piles. These floors are subjected to two types of loading: *externally*, predominantly loaded by point-forces by pallet racking and foundation piles and *internally*, by restrained shrinkage.

Concrete is a complex composed material, containing cement, additional binder, aggregates, additives and admixtures. In [Appendix I: 'Response of materials'](#) the material properties of these elements are explained and how they are related to shrinkage deformation.

Shrinkage is caused by deformation of cement paste in the concrete matrix. This deformation is restrained by internal and external restraints. Internal restraints are caused by elements in the mix design which contribute to the concrete strength, as aggregates and fibres. External restraints are caused by support conditions and loadings.

The effect of restraints will be dealt with in [I.6.4 Structural restraints](#).

Strain in a concrete member $\varepsilon_c(t)$ is composed of time-, and stress-(in)dependent strains.

For a uniaxial loaded element at t_0 with a constant stress $\sigma_c(t_0)$ the total strain is:

$$\varepsilon_c(t) = \varepsilon_{ci}(t_0) + \varepsilon_{cc}(t) + \varepsilon_{cs}(t) + \varepsilon_{cT}(t)$$

This strain formula has two parts:

$$\varepsilon_c(t) = \varepsilon_{c\sigma}(t) + \varepsilon_{cn}(t)$$

with:

$$\varepsilon_{c\sigma}(t) = \varepsilon_{ci}(t_0) + \varepsilon_{cc}(t) \quad \text{stress-dependent strain}$$

$$\varepsilon_{cn}(t) = \varepsilon_{cs}(t) + \varepsilon_{cT}(t) \quad \text{stress-independent strain}$$

$\varepsilon_{ci}(t_0)$ = initial strain at loading

$\varepsilon_{cc}(t)$ = creep strain at $t > t_0$

$\varepsilon_{cs}(t)$ = shrinkage strain

$\varepsilon_{cT}(t)$ = thermal strain

Separation is made in stress-dependent and stress-independent strains. Initial strain due to external loading and creep strain are stress-dependent strains. Whereas shrinkage and thermal strain are causing stress-independent strains (Fib bulletin 65, 2012).

In this research the focus is on shrinkage. Thermal strain should not be classified as shrinkage but as a dilation process. This differs from shrinkage based on changes due to internal moisture levels.

In structural applications, reinforcement is embedded in concrete for better resistance of tensile stresses. Reinforcement can be in the form of reinforcement bars or fibres. The use of steel fibres makes Steel Fibre Reinforced Concrete (SFRC). A combination of these two types of reinforcement makes a so called hybrid design. In [I.6.4.1 Internal restraint](#) this topic will be addressed.

The floors designed by ABT BV, are generally based on a 40~50 kN/m² distributed load and a point load by the pallet racking of 70~90 kN. The design parameters will be covered in detail in [Appendix II: Codes & Structural conditions](#).

In this research a theoretical approach is chosen to determine the amount of shrinkage. At ABT the shrinkage strain of several concrete prisms was measured. Goal is to simulate the deformation of these prisms, based on the theoretical approach. By simulating the practical measurements the outcome of the FEM model can be validated.

These concrete prisms were made at ABT in 2005. Concrete to make the prisms came from project sites. The change in length and weight over a time period of 84 days was measured.

Measurements started after the prisms stayed for 28 days in a climate chamber. During these 28 days, the relative humidity and temperature were fixed.

Drying shrinkage is a visual macroscopic result of deformations originating from changes in pressure at a microscale. Modelling these time dependent actions of the material combined with the other material responses as creep and relaxation can be done through a variety of models.

The exact mechanisms responsible for shrinkage are still topic of debate (Lu, 2019)(Lura, 2003).

There are many testing methods to measure shrinkage, also differences in terminology in cement technology are present. From modelling perspective, there exist multiple strategies and theories.

Models deriving the material parameters are based on the concrete age, cement composition, hydration, saturation and external environmental conditions. Advanced models contain all of these parameters. These models are classified as coupled-multiphase models. An example of this is the hygro-thermo-chemo-mechanical model (Gamnitzer, Brugger, Drexel, & Hofstetter, 2019) (Gawin, Pesavento, & Schrefler, 2006). It should be noted that these models are very complex and difficult to interpret. Their workability is limited due to the required amount of input parameters that should be known.

Methods describing the material mechanics are based on viscoelastic or viscoplastic models using springs-dashpot relations. These are described by Maxwell and Kelvin chain models, Voigt or Burgers (Z P Bažant & Wittmann, 1982).

Goal of this thesis research is therefore, to develop an efficient model. A model that reflects the development of drying shrinkage sufficient. As said, there exists very complex models, that are claimed to be accurate. However, these models are not general applicable by a structural engineer.

One of the known and proven methods to determine (drying) shrinkage is the theory of Kelvin and Laplace. By their theory, shrinkage is calculated by determining the capillary pressure in the cement microstructure. Capillary pressure is a hydraulic tensile force on the pore walls. Due to drying, the moisture concentration in the pores changes and so does the internal pore pressure. This theory is based on the formation of a concave menisci in the pores at the water-air interface. The radius of the menisci is related to the internal relative humidity.

This approach, based on capillary pressure, has a sound relation with thermodynamics and is proven by multiple researchers (Lura, Jensen, & Breugel, 2003)(Jensen & Hansen, 1999)(Lu, 2019)(Chen, Zhu, Zong, & Xiang, 2019)(L. Liu, Wang, Chen, & Wan, 2016)(L. Wu, Farzadnia, Shi, Zhang, & Wang, 2017)(Pichler, Lackner, & Mang, 2007).

The capillary tension is related to the changing internal pore relative humidity (RH). RH-levels in the pore is determined by the diffusion equation. This equation is known as Fick's 2nd law. Also this is a proven method by latter mentioned researchers.

The theory of Kelvin-Laplace and moisture diffusion are covered in detail in part [2.3 Method of Kelvin – Laplace](#). Numerical modelling and simulation of the drying concrete are described in part [3 Finite element modelling](#).

With the chosen working strategy, a parametric shrinkage model is developed based on a proven theory. By verifying the finite element model to the test data of the concrete prisms, a parametric model for shrinkage is created. After all these steps, it will be possible to answer the research question.

2 Theory of drying

Drying shrinkage can be calculated in multiple ways. The most common method is to follow the calculation-steps as described in the leading construction standards. For concrete structures these are the Eurocode 2 and the Model Code 2010. In the codes, drying shrinkage can be calculated according prescribed formulas. A detailed explanation of the codes can be found in [Appendix II: Codes & Structural conditions](#).

However, in order to understand the underlying mechanisms behind drying shrinkage. A breakdown of the elements contributing to shrinkage is needed.

The shrinkage calculation based on the codes is available in the user interface of DIANA FEA. Modelling drying shrinkage through these models in the user interface of the FEM package has limitations. As the amount of shrinkage is calculated for a structural object and does not regard detailed material parameters and cross-sectional difference in a concrete member. Goal of this thesis is to develop a model with a higher accuracy of drying shrinkage compared to the codes. In this chapter, the 'theory of drying', these parameters will be substantiated. Followed by an implementation in chapter [3 Finite element modelling](#).

Verification of the model developed in this thesis is performed by comparing the outcome with actual measured shrinkage data of a concrete prism. The technical information about this concrete prism can be found in [II.2 Structural conditions](#).

Drying of concrete is the evaporation of excess water through the pores of the hardened concrete. The excess amount of water is the part that is not consumed during the hydration of cement. In this research, the *test beam* is analysed. This concrete element has been cured in a climate chamber for 28 days. Inside this climate chamber a temperature of 20 °C and a RH of 100% is maintained. Most of the hydration takes place during the first 28 days. In other words, the increase of degree of hydration is most significant in this phase.

The diffusivity of concrete is strongly related to the degree of hydration. In the study of Liu et al., it is shown that the diffusivity has a clear relation with the change in degree of hydration. As the cement paste in concrete is hardening, the (micro-)pore structure is changing and a densification takes place. This is due to a reduction in connectivity of the capillary pores. Therefore, the diffusivity is decreasing when the degree of hydration is evolving (C. Liu et al., 2019).

The level of saturation is the relation between the evaporable water content and the total volume of the pores. This is essential for the diffusivity and thus responsible for the speed of drying.

The present pore pressure is linked to internal RH, which changes due to diffusion and evaporation of water. To compose the RH distribution, the transient moisture flow, based on the theory of diffusion, needs to be understood.

This transient distribution of humidity is derived from the transient heat equation. The use of the heat analysis method as the humidity analysis was proved to be successful by Holmes and West. (Holmes & West, 2003). In their study, the nonlinear calculation was performed using the finite element package Diana FEA. In this thesis, the same finite element package will be used.

In chapter 4, The pore size affected by shrinkage is explained followed by the accompanied mechanism. Chapter 5 presents the finite element implementation of this theory, concluding with the results in chapter 6.

2.1 The scale of drying

Over time, the major cause of shrinkage strain is drying of concrete. Changing internal moisture levels, due to drying, affects a few mechanisms. These mechanisms relate to the content of moisture to hydrostatic pressure by constitutive relations. Pores in the cement paste which undergo these pressure changes are micro- and nanometers in size.

The aim of this thesis is having an useable parametric FEM model efficiently reflecting on drying shrinkage. To properly understand the source mechanisms of shrinkage, a different scope is needed than is used for structural analysis. Therefore, downscaling is needed before modelling. See Table 1 for the multi-scale modelling levels (E. Koenders, 2015).

Cement hydration forms a product measured on nanoscale. The structure that is formed by these products is the hardened cement matrix, which is analyzed on microscale. Therefore, in cement paste focused studies, the cementitious microstructure is of interest. Discontinuities in the paste are called (micro)cracks.

Drying related responses have their source on micro- and nano-level. The boundary conditions for modelling moisture diffusion in a finite element model, have their origin at these levels.

Once the source mechanisms are known, the response of the whole system can be found by upscaling. Mortar and concrete are measured on mesoscale. At this scale, the effects of sand and aggregates are included. Structural response to external loading is taking place at macroscale. External measurable deformations are therefore referred to as macroscopic deformation.

Scale	Property	Size range
Macro	Mechanical, Cracking, Volume stability, Durability	$10^{-1} \sim 10^2$ (m)
Meso	Compressive and tensile strength, Fracture energy and toughness	$10^{-5} \sim 10^{-1}$ (m)
Micro	Hydration, Chemistry, Pore pressure, (Intrinsic) Permeability, Diffusivity	$10^{-6} \sim 10^{-5}$ (m)
Nano	CSH-formation, CH-formation, Ca/Si-ratio, Al/Si-ratio	$10^{-10} \sim 10^{-6}$ (m)

Source / Boundary conditions = Downscaling (left arrow) Response = Upscaling (right arrow)

Table 1. Multi-scale modelling (E. Koenders, 2015).

The theoretical models for drying shrinkage used in this thesis are effective at nano- and microscale. The results obtained are translated to meso- and macroscale by including the effects of sand and aggregate particles. A refined material model for concrete, including drying shrinkage strain, can be used in a macroscopic structural analysis. When the scope of interest is on macroscale, concrete is treated as homogenous material. See Table 2 for the scale levels of concrete.

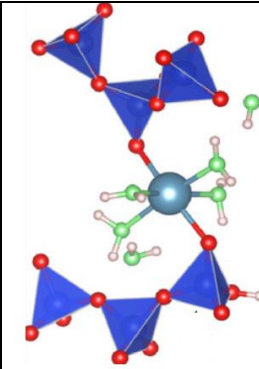
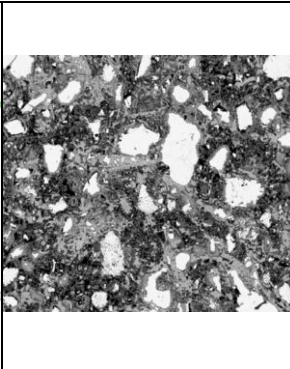


			
(A) Nanoscale	(B) Microscale	(C) Mesoscale	(D) Macroscale
CSH-formation	Cement paste	Mortar, Concrete	Structural component

Table 2. Multi-scale approach of cementitious materials.

The multi-scale approach is linked to the modelling strategy used in this thesis. Chapter 4 explains the mechanisms responsible for internal pressure and shrinkage strain. These theoretical models focus on processes taking place at a nano- and microscale. Chapter 5 explains the setup together with the results of the finite element model. The modelled elements are on a micro- and mesoscale. The found results are based on cement paste deformation and need to be corrected for the effect of aggregates. This results in a model valid for calculating macroscopic deformation due to drying shrinkage.

2.2 Physics of drying

Drying of concrete causes shrinkage mechanisms. Existence of a relation between changes of RH-levels in the pores and shrinkage is evident. The exact descriptions of these mechanisms, with mutual agreement by researchers, has not been reached yet (L. Liu et al., 2016) (Lura et al., 2003)(Lu, 2019).

As stated in the introduction of this thesis, one of the methods to determine (drying) shrinkage is based on the theory of Kelvin and Laplace. In principal, this is related to the capillary tension of the pore fluid. Proven by multiple researchers, this will be the leading theory for shrinkage modelling in this thesis (Lura et al., 2003)(Jensen & Hansen, 1999)(Lu, 2019)(Chen et al., 2019)(L. Liu et al., 2016)(L. Wu et al., 2017). The other important related shrinkage mechanisms are based on surface tension and disjoining pressure (Lura, 2003).

Surface tension is the relation between tensile stress and absorbed water molecules in the surface layer of solid particles. An illustration of the surface layer containing absorbed water can be seen in Figure 1 (a). When the relative humidity in the pores decreases, the thickness of the absorbed layer will also decrease. As a result of this, the surface tension in the absorption layer will increase. Surface tension at the surface of solid particles compared to pore pressure is seen in Figure 1 (b).

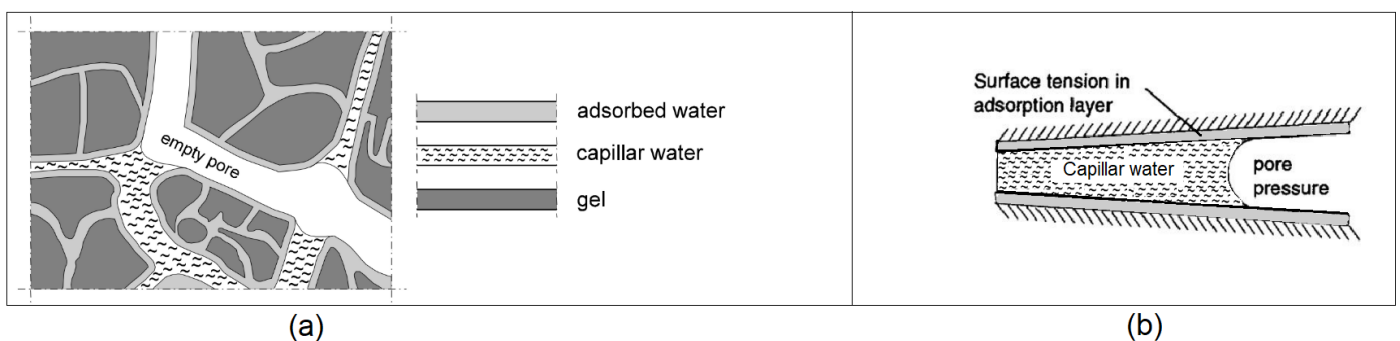


Figure 1. a) Moisture containing elements in hardened cement paste. b) Schematization of surface tension in the adsorption layer (Vervoort, 2015).

The approach of surface tension has been used in the past to model autogenous swelling and shrinkage. Due to absorption of water in the solid surface layer, swelling can occur. This was first documented by Bangham in 1931 (Bangham & Fakhoury, 1931). Autogenous shrinkage has been successfully related to the Bangham theory by Wittmann and Koenders (E. A. B. Koenders, 1997). This relation is the same as self-desiccation during the autogenous phase (described in [1.2.2 Autogenous shrinkage](#)). Self-desiccation is based on the surface tension theory. The moisture present in the absorption layer is not of interest for normal drying shrinkage. Suggested by Wittmann, the Gibbs-Bangham mechanism is valid for drying shrinkage only when the relative humidity is below 40% (Wittmann, 1968). According to a more recent research, the surface tension approach based on the Bangham theory is valid for pores having an internal RH of 20% or lower (Jennings, 2004). The classification of shrinkage mechanisms related to pore RH as presented by Jennings, is given in Table 3.

Disjoining pressure is most relevant for very small pores, which are affected only by low pore RH being less than 40% (Jennings, 2004). When the surface of two solids are separated by less than

two times the thickness of the absorbed water layer, disjoining pressure comes into effect. These very closely packed particles form a local region of hindered absorption, see Figure 2. The built pressure is a result of van der Waals forces, double layer repulsion and structural forces (Lu, 2019) (Lura et al., 2003). This is based on a publication by Ferraris and Wittmann (Ferraris & Wittmann, 1987). Van der Waals forces are contractive while double layer repulsion and structural forces are repulsive. When the pore relative humidity decreases, the thickness of the absorbed water layer decreases too. Resulting in a lower disjoining pressure and therefore an increase of shrinkage.

The mechanism of disjoining pressure was presented in the 60's by Powers to explain shrinkage below 40% of pore relative humidity (Ye, 2003)(Idiart, 2006).

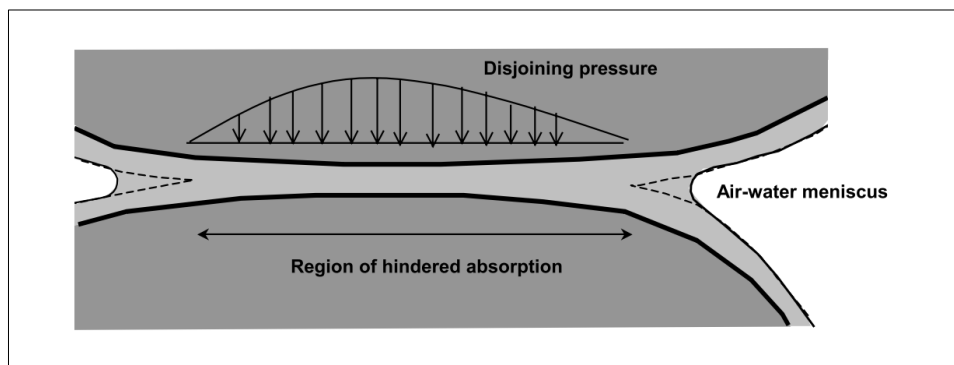


Figure 2. Disjoining pressure distribution along a surface of hindered absorption. Taken from (Lura, 2003) based on (Soroka, 1979).

When a concrete specimen is dried up to a RH lower than 10%, interlayer water is unbound and start to evaporate. Interlayer water is strongly bound in the hardened cement paste. Furthermore, water that is chemically bound in cement is regarded as 'non-evaporable' water. A specimen needs to be dried at 1000 °C to determine the amount of chemical bound water (Lura, 2003).

The types of mechanisms and their corresponding pore size are found in Table 3. Each level of pore relative humidity is related to the pore diameter by the Kelvin equation (Jennings, 2004).

Pore category	Diameter of pore	RH (%) in pores at start mechanism	Reversible shrinkage mechanism
Capillary	75 nm	90	Capillary tension
Meso	2-5 nm	40	Disjoining pressure
Micro	1.2-2 nm	20	Gibbs-Bangham
Nano	<0.5 nm	0	Interlayer

Table 3. Categorization of pores in hydrated cement paste (Jennings, 2004) and as used by G. Ye (Ye, 2003).

There is no mutual agreement among scientist for an exact effective pore size per mechanism (Treval Clifford Powers, 1948)(Jennings, 2004)(Xi, Bažant, Molina, & Jennings, 1994).

To include all the known mechanisms, a fully-coupled multi-phase model is needed. As described by Gamnitzer et al., the application of such a model surpasses the scope of this thesis and is not of additional value unless all needed parameters are fully understood and motivated (Gamnitzer et al., 2019) (Gawin et al., 2006).

However, for relative humidity values of 40% and higher, the capillary pressure is a valid theoretical mechanism. It can be used to analyse drying shrinkage up to pores as small as 2.5 nm in diameter (Ye, 2003)(D.P. Bentz & Jensen, 2004). The FEM model used in this thesis, is subjected to drying at 65% RH. This is well within the reach of the capillary pore tension approach. Therefore, this is the theory used to construct the FEM model. Other mechanism are not included in the research, as the scope is on drying shrinkage.

In Figure 3, the theoretical steps needed to model drying shrinkage of concrete are shown. The diagram has two separable equations for the flow of moisture. These are the internal moisture levels expressed in relative humidity and moisture loss at the surface due to evaporation. The driving internal force is the difference in moisture concentration resulting in diffusion. At the surface, the amount of evaporation is defined by the difference in relative humidity of the surface and the ambient air.

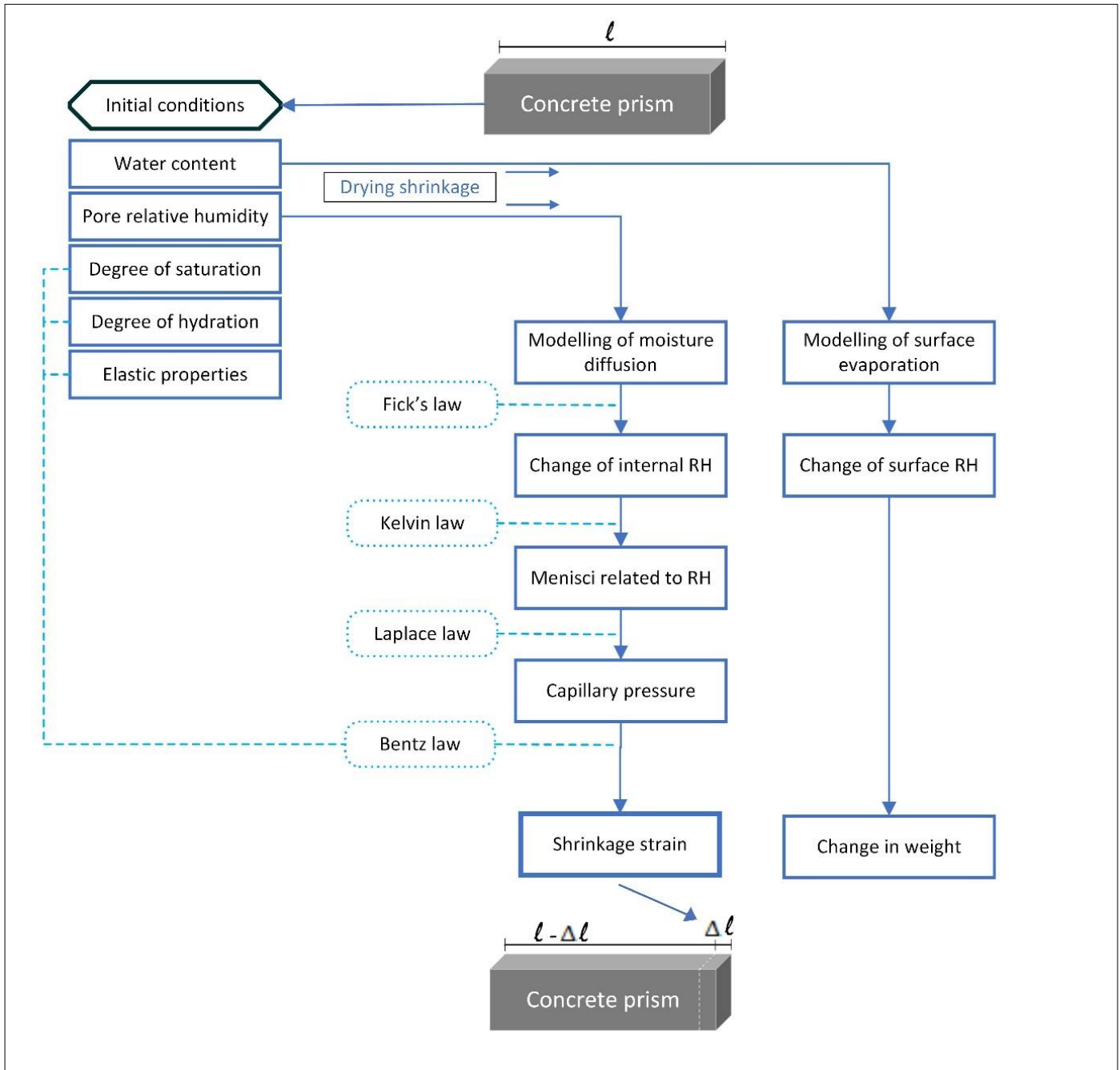


Figure 3. Flowchart used to model the drying of concrete.

The calculations for the drying shrinkage strain are performed in Microsoft Excel. In a single sheet, the outcomes of the Kelvin-Laplace and Bentz calculations are combined. The needed pore RH is produced by diffusion simulation in DIANA FEA which is based on Fick's law.

2.3 Method of Kelvin – Laplace

The Kelvin-Laplace method is based on the capillary tension approach. Compared to the other explained shrinkage mechanisms, this approach is most suitable. The range of ordinary drying lies with the theoretical range of the capillary tension approach (Table 3).

In the chart of Figure 3, it can be seen that the capillary pressure of the pore fluid is calculated using the method of Kelvin - Laplace. The most important input parameter is the relative humidity which is calculated by the use of Fick's law. At last, shrinkage strain is calculated by the use of Bentz law for which the degree of saturation and the stiffness properties of the paste needs to be known

2.3.1 Kelvin equation

Capillary pressure is a hydraulic tensile force on the pore walls. Due to drying, the moisture concentration in the pores change and so does the internal pore pressure. This theory is based on the formation of a concave menisci in the pores at the water-air interface. The radius of the menisci is related to the internal relative humidity. As the cement paste dries, the radius decreases. A schematisation is shown in Figure 4, where drying is caused by the differences of relative humidity in the pore system.

The drying is caused by differences of relative humidity in the pore system. Larger pores in the system will dry out first. As smaller and smaller pores are affected, the radius decreases further. A two dimensional illustration of this process is shown in Figure 5 (next page). At (a) the pores are fully saturated, drying evolves over (b),(c) and (d). This illustration is take from a paper in which every pore was modelled individually, based on 3D lattice approach (L. Liu et al., 2016).

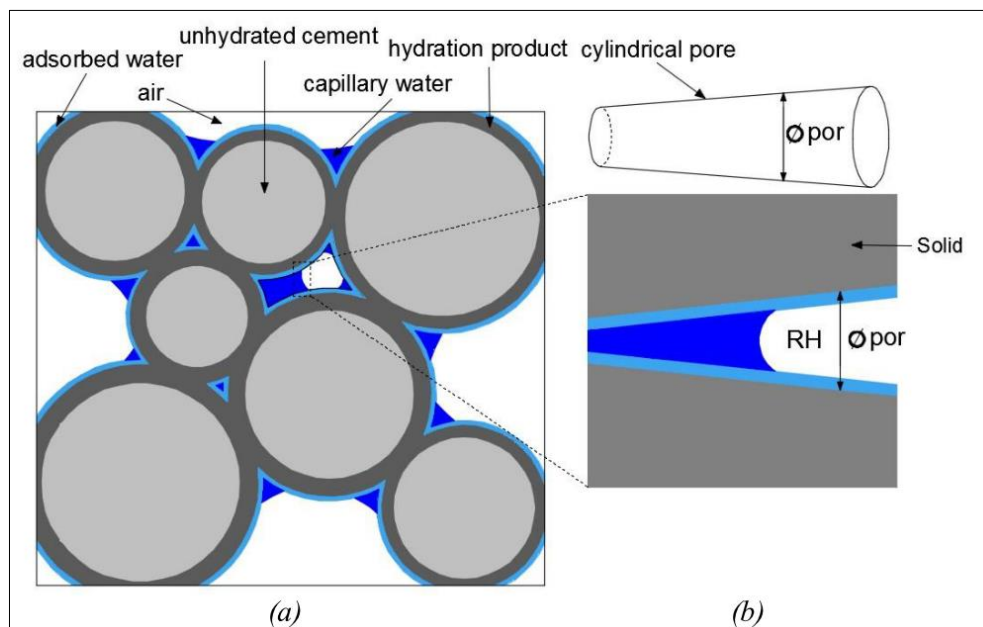


Figure 4. a) Microstructure of cement paste. b) Cylindrical capillary pore (Lu, 2019)

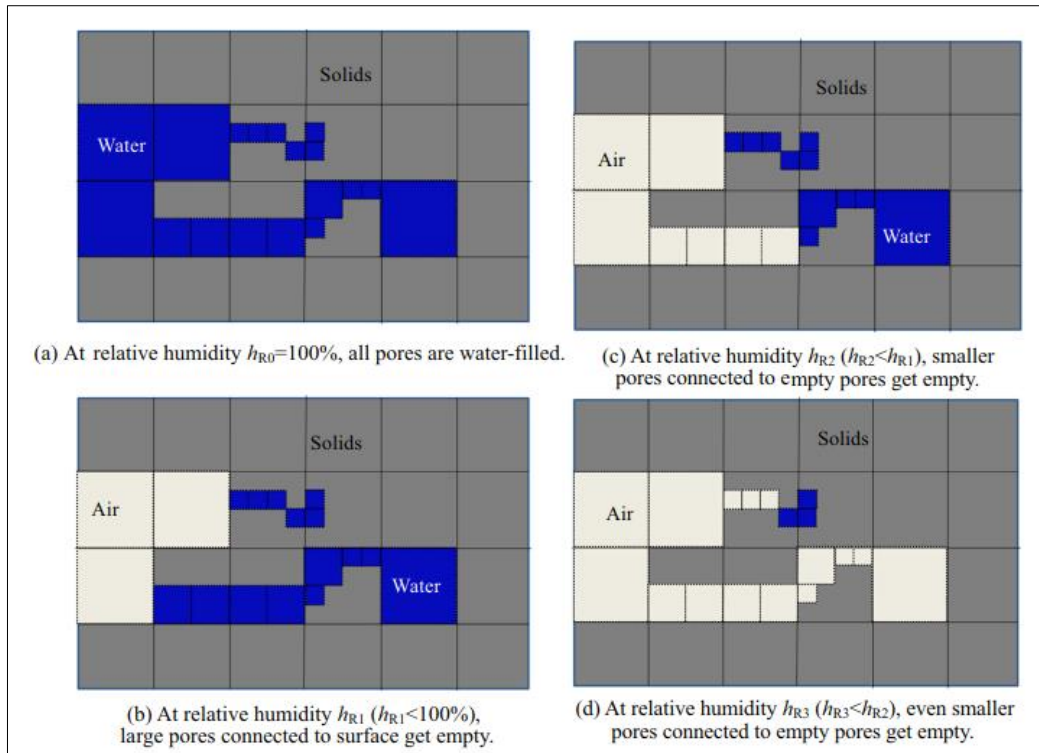


Figure 5. Illustrative figure of two dimensional moisture loss in a pore (L. Liu et al., 2016).

The capillary pressure (p_c) is calculated based on the relative humidity (RH) according to the Kelvin equation (Jensen, 1993). Capillary pressure is also denoted as σ_{cap} :

Kelvin's Law
$$p_c = P_g - P_l = -\frac{\rho RT}{M} \ln(RH)$$

$p_c = \sigma_{cap}$	Capillary pore pressure		MPa
$p_g =$	Pore gaseous pressure		MPa
$p_l =$	Pore fluid pressure		MPa
$RH =$	Relative humidity		$P/P_0(T)$
$\rho =$	Volumetric mass of water	= 1000	kg/m^3
$R =$	Universal gas constant	= 8.314	$J/mol \cdot K$
$T =$	Temperature	= 293.15	K
$M =$	Molecular weight	= 0.018	kg/mol

Where RH is the ratio of measured pressure of water vapor (P) over the saturated water pressure ($P_0(T)$), often expressed in percentage. The theory of Kelvin is based on relative humidity and not on the absolute humidity. This is due to the temperature dependency of relative humidity. Temperature affects the speed of moisture transmission through the porous medium. However, in this research the temperature is kept at 20 degrees (293.15 K). The concrete *test beam*, simulated in this thesis, was dried under the same ambient temperature. Molecular weight is the same as used in comparable studies. The same is valid for the temperature (Lura, 2003)(Chen et al., 2019)(Park, Kwon, & Song, 2011).

This formula is not time dependent. Internal changes of relative humidity over time is calculated in the finite element calculation.

2.3.2 Laplace equation

In Laplace's equation, the pressure is related to the dimension of the pore affected by drying. The principal radius (r) of the water-gas interface is calculated (Figure 6). The radius is based on an idealized spherical pore structure (Figure 4 (b)).

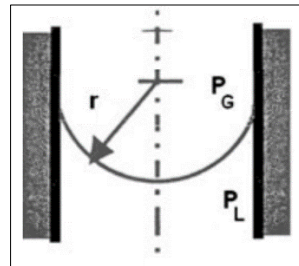


Figure 6. Equilibrium interface at water-air meniscus (Park et al., 2011).

Laplace's Law	$p_c = p_g - p_l = \frac{2 \cdot \gamma}{r}$	rewritten to \rightarrow	$r = \frac{2 \cdot \gamma}{p_c}$
$p_c = \sigma_{cap}$	Capillary pore pressure		MPa (from Kelvin's)
$p_g =$	Pore gaseous pressure		MPa
$p_l =$	Pore fluid pressure		MPa
$r =$	Radius of interface meniscus		m
$\gamma =$	Surface tension of water	= 0.07252	N/m

Surface tension at the liquid water interface is influenced by dissolved salts (ions). This can be caused by alkali hydroxide during the hydration phase. As a result of this, the measured pore RH can be lower than the measured RH. The difference is a couple of per cent and of influence mostly during the hardening phase (Lura et al., 2003). The dissolution of salts is not included in this thesis. The shrinkage strain calculation as presented here, do not need a Pore Size Distribution (PSD) nor a specific surface area of the pore walls on which the pressure is acting. The change in pore size, affected by drying, is indirectly accounted to the change in radius and degree of saturation during drying. The PSD can be determined by a Mercury Intrusion Porosimetry (MIP). In this test, mercury intrudes the specimen under an increasing pressure, the intruded volume is measured. MIP is only possible on samples without evaporable water in the pores. An contact angle of 0 degree between the water surface and the solid surface is assumed (Pichler et al., 2007)(D.P. Bentz & Jensen, 2004). See Figure 7: $\alpha_w \approx 0^\circ \rightarrow \cos(0^\circ) = 1$
 When another liquid is used, these assumptions are not valid and the contact angle should be included in the modified Laplace's formula.

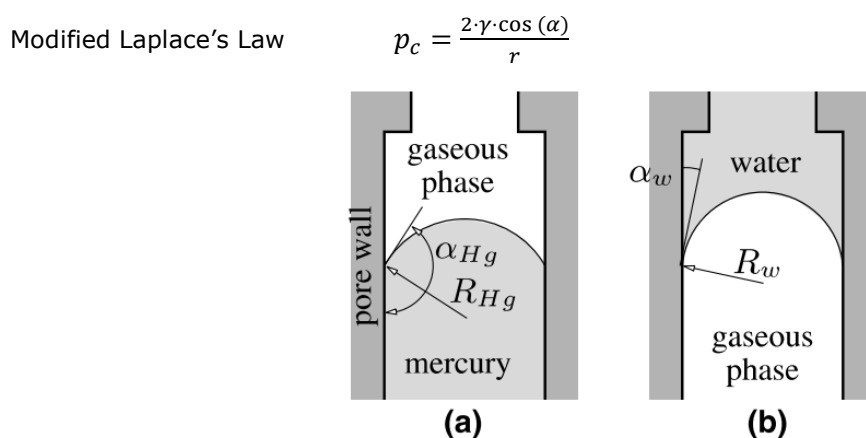


Figure 7. Radii and contact angle of (a) mercury-gas and (b) water-gas interfaces (Pichler et al., 2007)

Based on findings by I. Soroka in 1979, the Kelvin-Laplace method is reliable in the range of RH 45% and higher (written by P. Lura)(Soroka, 1979). This value gives a meniscus radius of 1.35 nm. Jennings published equal numbers in 2004, see Table 3 (Note the diameter of pores is used in the table). It should be mentioned that RH of 45% is classified as low and not common in the Netherlands, nor preferred for indoor conditions.

The *test beam* is subjected to 65% RH. When this level of RH is reached during drying, this would give a capillary tensile pore pressure of 58 MPa. The affected pore size has a radius of 2.5 nm at this level. The decrease of RH in the pores due to drying by diffusion is inherent to a decrease of water content in the microstructure. The water saturation factor in Bentz deformation law is correcting for this effect.

In Figure 8 and Figure 9, graphical representation of the Kelvin-Laplace formula are given. The practical range for this thesis lies between RH 95%-65%. As the specimen is assumed to have an initial internal relative humidity of 95%. Part of the water is consumed for hydration during the 28-days period in the climate chamber.

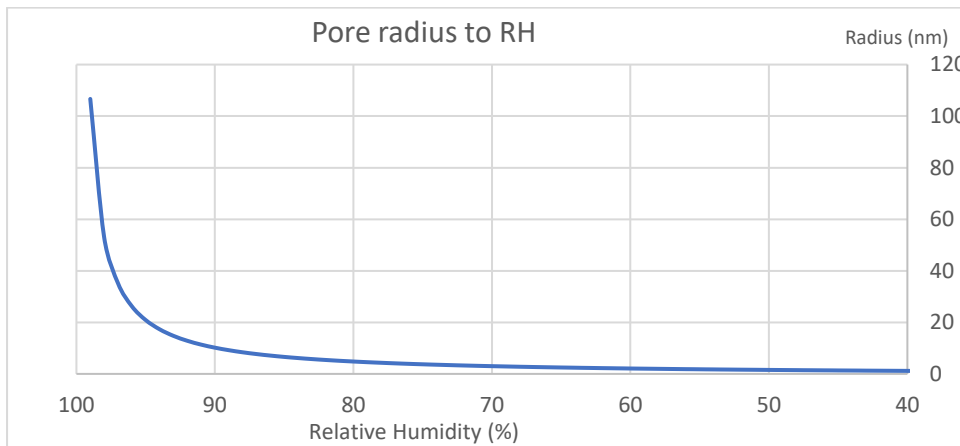


Figure 8. Radius of the water-air meniscus to Kelvin-Laplace.

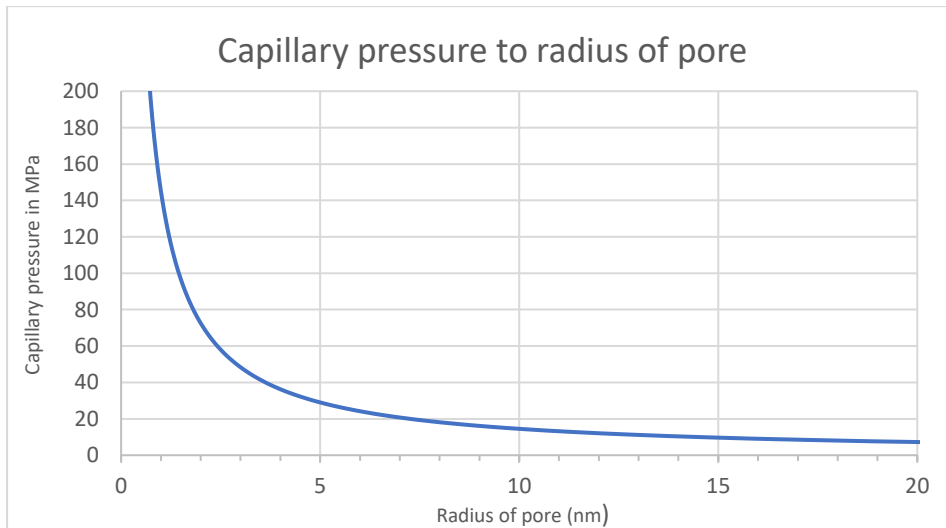


Figure 9. Capillary pressure related to radius of pore.

2.4 Bentz deformation law

The deformation in the cement paste is based on the pore pressure. It was Bentz et al. who first introduced this method (Dale P. Bentz, Garboczi, & Quenard, 1998).

The deformation of the cement paste based on Bentz law:

$$\varepsilon_{LIN} = \frac{S_w \sigma_{cap}}{3} \left(\frac{1}{K_p} - \frac{1}{K_s} \right) \text{ with } P_c = \sigma_{cap} \quad (\text{Dale P. Bentz et al., 1998})$$

ε_{LIN} = Linear elastic strain (m/m) or microstrain ($\mu\text{m}/\text{m}$)

S_w = Water saturation factor (-)

σ_{cap} = Pore fluid stress / capillary stress (MPa)

K_p = Bulk modulus of the whole porous system (MPa)

K_s = Bulk modulus of the material making up the solid frame (MPa)

The stress in the pore is acting in three dimensions. From this stress, a dimensional change of length can be calculated. This is based on the theory of Mackenzie who developed a general mathematical model for a porous medium. It is modelled as an solid elastic material containing spherical holes (Mackenzie, 1950).

In 1998, the original theory has been rewritten to be better understood and linked to the theory of finite element modelling (Dale P. Bentz et al., 1998).

Since then, this theory is used on cement paste and concrete modelling by multiple researchers (Chen et al., 2019)(Zhang, Hou, & Han, 2012)(Lura, Jensen, & Weiss, 2009)(L. Liu et al., 2016)(Lu, 2019).

In the Bentz formula, the tensile pore stress (σ_{cap}) is the key input parameter. According to the Kelvin-Laplace law, stress increases as the pore RH decreases.

The drying part of concrete is cement paste. The here used formulas are based on poromechanical models validated on the material properties of cement paste (L. Liu et al., 2016).

Shrinkage strain of concrete is lower than that of cement paste. As the volumetric part of the material shrinking is lower and the aggregates form an internal restraint of free elastic deformation. The shrinkage strain of cement paste is corrected for the effect of aggregates by the Neville and Brooks formula, this is covered in part [1.6.4.1.3 Influence of aggregates](#).

Concrete mixtures with low w/c-ratios have a cement paste that shows relatively more shrinkage.

The initial conditions are determined for a concrete mixture with a composition as seen in Table 9. The measured free shrinkage deformation of the prisms is in the same range. Cement used for the prisms are blends of CEM III and CEM I. All mixtures have a w/c-ratio of 0,5.

The cement type used for theoretical modelling is Portland cement, CEM I. Because the used models for simulating the microstructure formation during hardening are based on CEM I. The models affected by the cement type are: Powers' model and Bentz law. 'Hymostruc Lite' is the software tool used to simulate the hydration. This tool is not capable of simulating other cement types. A strong recommendation in the aim for a parametric FEM model including accurate drying shrinkage, is to use models which distinguish the cement types.

This results in initial material properties based on the cement specific conditions. The concrete prisms simulated in this thesis are of moderate strength and not of low w/c-ratio. Differences in hydration and the development of (drying) shrinkage strain become significant for high strength low w/c-ratio cement paste.

2.4.1 Powers' volumetric model

The (liquid) water saturation factor (S_w) is multiplied by the active capillary pressure (σ_{cap}) in the formula by Bentz. For a fully saturated paste, the factor is 1. For a completely dried out paste, it is 0. This factor is responsible for reducing the presence of capillary pressure during drying, as lesser water is present.

The factor of saturation is calculated as the ratio of evaporable water content ($V_{ew}(\alpha)$) over the total pore volume ($V_p(\alpha)$). Both these values are depending on the degree of hydration (α) where the degree of hydration on itself depends on the w/c-ratio (See [2.4.2 Degree of hydration](#)).

Powers' model is used to calculate the saturation factor (T. C. Powers & Brownyard, 1947). The result of this calculation is used as initial value of saturation. This level of saturation is reached after a period of sealed hydration.

Saturation fraction:
$$S_w = \frac{V_{ew}(\alpha)}{V_p(\alpha)}$$

S_w = Water saturation factor (-)
 $V_{ew}(\alpha)$ = Evaporable water content (m^3/m^3)
 $V_p(\alpha)$ = Total pore volume of the paste (m^3/m^3)

Powers' model calculates the volumes of the elements present in the hydrating paste. The sum of volumes make a total of 1, as the volumes are per unit of cubic volume.

$$S_w = \frac{V_{ew}(\alpha)}{V_p(\alpha)} = \frac{V_{cw}(\alpha) + V_{gw}(\alpha)}{V_{cw}(\alpha) + V_{gw}(\alpha) + V_{cs}(\alpha)}$$

Chemical shrinkage	(m^3/m^3)	$V_{cs}(\alpha) = 0.2(1 - p)\alpha$	} $\Sigma_i V_i = 1$
Capillary water	(m^3/m^3)	$V_{cw}(\alpha) = p - 1.3(1 - p)\alpha$	
Gel water	(m^3/m^3)	$V_{gw}(\alpha) = 0.6(1 - p)\alpha$	
Gel solid	(m^3/m^3)	$V_{gs}(\alpha) = 1.5(1 - p)\alpha$	
Cement	(m^3/m^3)	$V_c(\alpha) = (1 - p)(1 - \alpha)$	
Degree of hydration	(-)	$\alpha = \text{based on HYMOSTRUC simulation}$	

The volumes of hydration products in cement paste are largely depending on the volumetric ratio of water and cement. As the proportion of these two products denotes the initial porosity of the paste, denoted by (p).

Initial porosity
$$p = \frac{V_w}{V_c + V_w}$$

p = Initial porosity cement paste (-)
 V_w = Water volume (m^3/m^3)
 V_c = Cement volume (m^3/m^3)

$$p = \frac{w/c}{(w/c) + (\rho_w/\rho_c)}$$

ρ_w = Density of water $\rho_w \cong 1000 (kg/m^3)$
 ρ_c = Density of cement $\rho_c \cong 3150 (kg/m^3)$

From these calculation it is deduced that the porosity of young concrete increases as the w/c increases (Xi et al., 1994). This results in relative more macroscopic pores which increases the diffusivity. The initial porosity for the cement paste used in the concrete of the test beams is $p = 0.61$. A simulation of hydration is made in HYMOSTRUC Lite, this gave an similar level of initial porosity.

In Figure 10, a graphical representation of Powers' Model is given. The degree of hydration (α) never reaches 100% in practise. For lower w/c mixtures, the degree of hydration evolves slower. It is assumed that 80% of hydration is reached for a mixture with $w/c=0,5$. See [2.4.2 Degree of hydration](#).

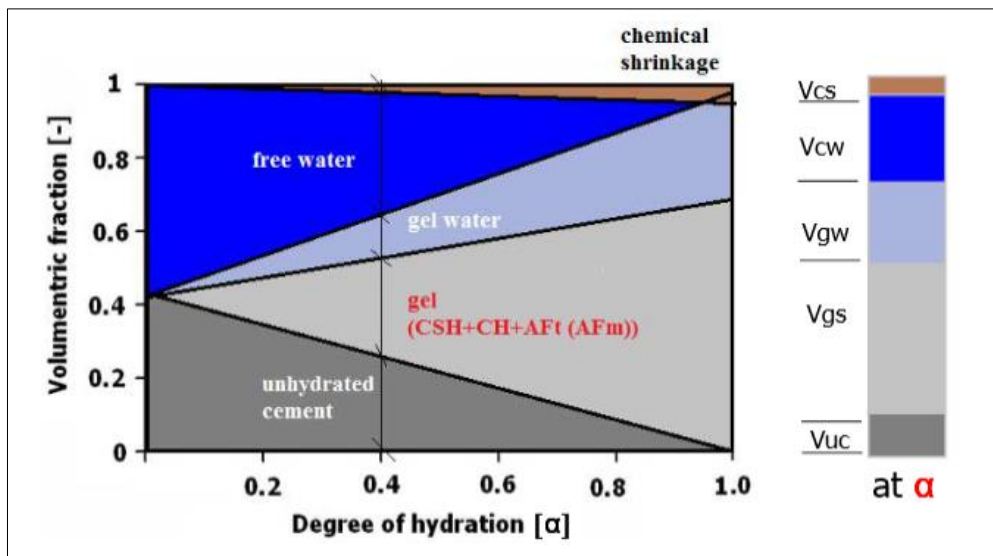


Figure 10. Powers' Model.

The initial saturation fraction (S_w) for the mixture used in this thesis can now be calculated using Powers' model, initial $S_w = 0.87$. Complex models for the saturation fraction exists, linking to the internal relative humidity or to the capillary pore pressure. Examples of these are given by Lebental et al. and Baroghel-Bouny et al. (Lebental, Moujahid, Lee, Maurice, & Cojocaru, 2012)(Baroghel-Bouny, Mainguy, Lassabatere, & Coussy, 1999). A more simplistic approach is to take the level of saturation equal to the pore relative humidity, as proven by Chen et al. Their study is comparable due to the use of the Kelvin-Laplace equation and Bentz law based on Mackenzie theory (Chen et al., 2019). The differences in the outcome of these methods is only a few percentage. Therefore the strategy by Chen et al. is chosen. Initially the saturation fraction is equal to $S_w = 0.87$ when $RH < 0.87$ the RH level is used, $S_w = RH$.

2.4.2 Degree of hydration

The degree of hydration is an important parameter for the microstructure formation.

A degree of hydration equal to 1 means a fully hydrated paste.

The development of the degree of hydration is measured by isothermal calorimetry (Gamnitzer et al., 2019)(Bílek et al., 2016)(Lura et al., 2003). The measured heat of hydration (Q) over the potential heat of hydration (Q_{pot}), results in the degree of hydration (α).

$$\text{Degree of hydration} \quad \alpha = \frac{Q}{Q_{pot}}$$

This is an experimental method to determine the maturity of the material. Theoretical models to determine the maturity also exist, as the Arrhenius equation or Nurse and Saul (Jensen & Hansen, 1999). These are based on isothermal and adiabatic development of cement during hydration. Maturity models differ per cement type, as the activation energy is not equal (Z P Bažant & Wittmann, 1982). The models used for the maturity and activation energy are of special interest when the focus is on the influence of temperature in combination with relative humidity. However, their influence is mainly on the hardening process of cement paste which is interesting for (autogenous) deformation but limited for drying shrinkage.

In this research, the degree of hydration of Portland cement is simulated in Hymostruc (HYdration MOrphology and STRUcture). This software is based on the multi-phase hydration theory of 'hygro-thermal-mechanical model'(Gawin et al., 2006). Simulating the hydration of each individual cement particle. The software tool, HYMOSTRUC Limited edition 1.7, is developed by Microlab at the TU Delft. Hymostruc makes 3D numerical simulations of cement hydration and microstructure development (Dr. ir. E.A.B. Koenders, 2013)(Ye, 2003)(K. van Breugel, 1991). The degree of hydration (α) is a function of the particle size distribution of the microstructure which is formed during the hardening of cement.

A performed simulation resulted in a degree of hydration of $\alpha = 0.74$, after 28 days of sealed hydration. This is a bit less than the expected $\alpha = 0.80$ on the long term which is achieved in the time after sealed hydration. In this thesis, the degree of hydration is kept constant at $\alpha = 0.74$. Furthermore, the ambient temperature is kept constant at 20°C.

As input, the default composition for a CEM I binder was used having a standard Bogue mass fraction for the 4 main cement compounds. The Blaine value, donating the specific surface area of cement, was kept at 400 m²/kg.

The microstructure created by the numerical simulation can be visualized in ParaView 5.7.

In Figure 11, the particle distribution in a 100 * 100 μm cube of fresh cement is seen at the left. The ride-side of the picture shows an isolation of the capillary water in the pore system.

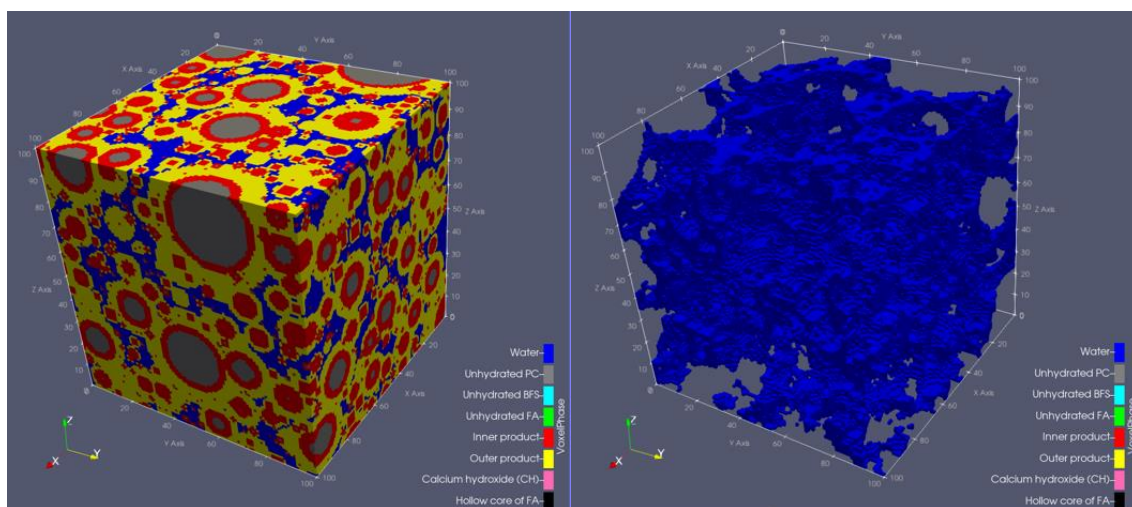


Figure 11. Visualisation of particles in young cement paste. Imaging performed in Paraview, based on Hymostruc data.

left) Particle distribution. right) Capillary water.

For the calculations the HYMOSTRUC software is used to obtain the degree of hydration, Elastic modulus of the paste and the internal relative humidity. All values are taken after 28-days of sealed hydration.

- The degree of hydration (α) is needed in Powers' volumetric model. $\alpha = 0.74$ (–)
- The elastic modulus of the paste. $E_p = 14000$ MPa
- The internal relative humidity (RH) is used as initial value in the finite element simulation of moisture diffusion through concrete. By the consumption of water in the cement reaction, the internal moisture level is decreasing even when the specimen is sealed. $RH_0 = 95\%$

In line with the research question, HYMOSTRUC was the preferred option for this thesis above the other previous mentioned theoretical maturity models.

HYMOSTRUC has the potential to be coupled with a structural model used for finite element calculations. This is done by using the data-export functions of HYMOSTRUC, as was used by K. Nijs for his master thesis. The research focussed on FEM implementation of a specific model for drying shrinkage. A material subroutine was used to control DIANA FEA which is regarded inscrutable. However, the usage of HYMOSTRUC was sound.

In this version, the cement particles under hydration and their products are presented as spherical or as cubicle particle. Spherical is used, as this is corresponding to the Kelvin-Laplace theory. Academics of the faculty Civil Engineering and Geosciences at Delft University of Technology are currently exploring improvements of existing methods. One of these improvements focus on morphology by using irregular and randomly shaped particles (Materials and Environment section at the department of Materials, Mechanics, Management & Design (3Md) at Civil Engineering and Geosciences, TU Delft).

2.4.3 Bulk modulus of the system

In Bentz deformation law, bulk modulus of the solid skeleton (K_s) and bulk modulus of the porous body (K_p) are used.

$$\varepsilon_{LIN} = \frac{S_w \sigma_{cap}}{3} \left(\frac{1}{K_p} - \frac{1}{K_s} \right)$$

The bulk modulus is the ratio of volumetric stress to volumetric strain. This is different than the Young's modulus, being the ratio of directional tensile stress to tensile strain.

By the elastic modulus of the paste (E_p) and Poisson's ratio (ν), the bulk modulus of the porous body is calculated by (Lura et al., 2003)(Zhang et al., 2012):

$$K_p = \frac{E_p}{3(1 - 2\nu)}$$

Values used:

$E_p =$	Elastic modulus of the paste	14000 MPa	From HYMOSTRUC
$\nu =$	Poisson's ratio	0.2 (–)	From (Nielsen, 1991) as used by: (Lura, 2003)(Lu, 2019)
$K_p =$	Bulk modulus of the porous body	7800 MPa	
$K_s =$	Bulk modulus of the solid skeleton	45000 MPa	For cement paste with 0.5 w/c From (L. Liu et al., 2016)

2.5 Drying shrinkage at equilibrium

With the presented formulas, the drying shrinkage strain at equilibrium can be calculated. This does not include moisture transmission over time at a certain diffusivity. It takes 5~10 years to reach full equilibrium.

The initial internal pore RH is 95%, at dried equilibrium the internal RH is 65%

This results in empty pores of 2.5 nm in radius (r) and larger. With a capillary pressure (σ_{cap}) of 58 MPa in the smallest pores. The saturation fraction (S_w) has decreased from an initial 0.88 (-) to a value equal to the present RH, making $S_w = 0.65$.

Resulting in a cement paste shrinkage at equilibrium of $\varepsilon_{HCP} = 1127 \mu m/m$. This value is the strain due to drying at the final equilibrium level of RH = 65%. The value is deducted by 216 $\mu m/m$ of the theoretically calculated value. A deduction is needed due to the rise in capillary pressure between relative pore humidity of 100% to 95% due to cement hydration. Without this deduction, the resulting strain includes drying and autogenous shrinkage.

When the internal restraining effects of sand and aggregates are included, the shrinkage of concrete can be calculated. As stated in appendix [I.6.4.1.3 Influence of aggregates](#).

$$\varepsilon_c = (1 - a)^{n_p} \cdot \varepsilon_{HCP}$$

ε_c	=shrinkage of concrete	$\mu m/m$	
ε_{HCP}	=shrinkage of hardened cement paste	1127 $\mu m/m$	
a	=aggregate volume fraction	0.704 (-)	(Table 9)
n_p	=correction factor	$n_p = 1.2 \sim 1.7$ by Neville and Brooks	(Neville & Brooks, 1991)

Another, more accurate, model exists to calculate the restraining effects of aggregates. This is Pickett's model.

$$\varepsilon_c = (1 - a)^\beta \cdot \varepsilon_{HCP}$$

β	=correction factor	1.508
---------	--------------------	-------

$$\beta = \frac{3(1 - \nu_p)}{1 + \nu_p + 2(1 - \nu_s) \left(\frac{E_p}{E_s} \right)}$$

ν_p	=Poisson's ratio of cement paste	0.2	
ν_s	=Poisson's ratio of aggregate particle	0.3	(Pichler et al., 2007)
E_p	=Elastic modulus of cement paste	14000 MPa	From HYMOSTRUC
E_s	=Elastic modulus of aggregate particle	50000 MPa	(Pichler et al., 2007)

The aggregate volume fraction of the concrete used for the ABT test beams is $a = 0.70$. This value is accompanied by an correction factor of $\beta = 1.48$, thus in the range of $n_p = 1.2 \sim 1.7$ as suggested by Neville and Brooks (Neville & Brooks, 1991).

$$\varepsilon_c = (1 - a)^\beta \cdot \varepsilon_{HCP} = (1 - 0.704)^{1.508} * 1127 = 180 \mu m/m$$

In the test performed by ABT, the concrete prisms were subjected to drying for 84 days. This will result in a lower shrinkage value than found at the equilibrium condition, which takes years to develop.

A second calculation is made, assuming a relative air humidity of 50%. In this drier conditions the cement paste shrinkage at equilibrium is $\varepsilon_{HCP} = 1446 \mu m/m$ and concrete shrinkage is estimated to be $\varepsilon_c = 231 \mu m/m$. Being 28% higher compared to the more humid drying condition.

The calculated values are compared to the measured values in chapter [4 Discussion of results](#). In chapter 3, diffusion and therefore time-dependency will be included in the calculation.

2.6 Diffusion

Concrete contains water for cement hydration and workability. The part of water not consumed by hydration will be subjected to drying. Transmission of water through the material is taking place by diffusion.

The *test beam* specimens that are analysed were cured before being subjected to drying. Material parameters, as the degree of hydration and the stiffness of the element, are assumed to be constant during drying. The reason for taking these maturing parameters constant is because the degree of hydration has mostly matured during the curing phase. Furthermore, by eliminating changes in material characteristic, full focus is on diffusion of moisture. The study of Liu et al. focused on the curing phase and presented that the change in diffusivity has a clear relation with the change in degree of hydration. As the cement paste in concrete is hardening, the (micro-)pore structure is changing and densification is taking place. Consequently, it reduces connectivity of the capillary pores. Therefore, the diffusivity is decreasing when the degree of hydration is evolving (C. Liu et al., 2019).

The level of relative humidity (RH) is clearly changing during drying. The speed of drying, expressed as diffusivity, is based on the level of RH. A highly non-linear relation exists between the diffusion coefficient and relative humidity. As can be seen in the graph of Figure 12, published by G. Ye and Holmes & West (Holmes & West, 2003)(Ye, 2003). This graph is based on the premier publications in the field of moisture diffusion through concrete by Bažant and others (Z.P. Bažant & Najjar, 1971) (Z P Bažant & Wittmann, 1982).

In the graph of Figure 12, distinction is seen for the diffusion coefficients between the w/c ratios. When the w/c ratio is higher, the microstructure formed is less dense and the amount of capillary pores is higher.

During drying, the fully saturated conditions change to non-saturated. This causes a decrease in moisture diffusion.

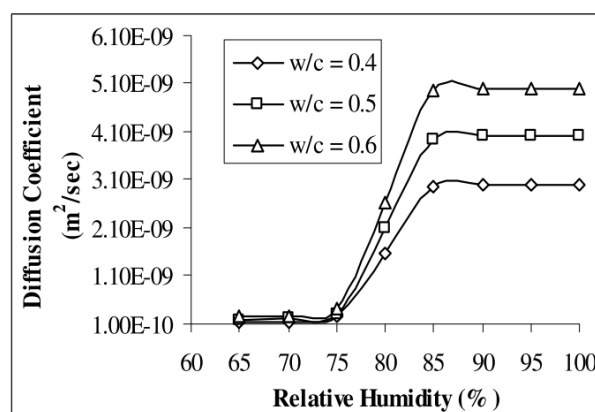


Figure 12. Diffusion coefficient for concrete of different w/c-ratio's (Holmes & West, 2003).

Within concrete mechanics, there are three known mechanisms resulting in shrinkage due to moisture diffusion (Xi et al., 1994). Being: ordinary diffusion (molecular diffusion), Knudsen diffusion and surface diffusion. This distinction of diffusion mechanisms in cementitious materials was first published in 1994 by the renowned researchers Xi, Bažant, Molina and Jennings.

It is out of the scope of this research to cover them in dept. Though, it can be said that surface diffusion is the driving force behind the mechanism of 'surface tension', as covered in part [2.2 Physics of drying](#). This type of diffusion is only prone at very low humidity's. Knudsen diffusion describes dynamic viscosity and the mobility of individual molecules.

Based on the publication by Chen et al., ordinary diffusion is described by the to be introduced Fick's law of diffusion. In this thesis report, diffusion is used without further specifying the underlying type.

Diffusion is modelled without the presence of sources and sinks which affect the concentration balance of the system. Moisture is not added to the system or extracted in another way than by

evaporation at the system boundaries, being the surface of the concrete element. In the chapter about Benz deformation law and the usage of HYMOSTRUC, an assumption on morphology was made. All particles and pores are assumed to be spherical in the cementitious material. This is in agreement with the modelling method used in HYMOSTRUC. For this reason the assumption on morphology is acceptable in this research.

The ordinary diffusion of water moisture through the porous medium is described by Fick's first law of diffusion. Time dependency is included in the second order non-linear differential equation of Fick's second law. This second order equation is used to calculate the relative pore humidity throughout the drying cross section. The first order equation is used to calculate the surface flux of moisture evaporation.

Another well-known law of permeation is the law of Darcy. Darcy's law describes a flow of fluid through a porous (permeable) solid. This law is based on the flow of water in a liquid form due to a difference in hydraulic head. In this study the focus is on water in gaseous phase where transmission of moisture is a result of differences in concentration levels. This is described by Fick's laws of diffusion.

2.6.1 Fick's 2nd law – diffusion

Fick's law of diffusion is used to obtain the RH-distribution needed to calculate shrinkage strain by the capillary tension approach.

Diffusion through the porous medium is done by a nonlinear transient equation. Being transient means that the main coefficient, the diffusion coefficient, is affected by the current condition. Over time, the element is drying and diffusivity is decreasing. Fick's second law can be used to describe a flow of concentration or mass through a medium (Van den Akker & Mudde, 2014). The relative pore humidity is in the range between completely dry and fully saturated, $0 < H < 1$ (Fib bulletin 65, 2012).

Fick's 2nd law of diffusion
$$\frac{\partial RH}{\partial t} = \frac{\partial}{\partial x} \left(D(RH) \frac{\partial RH}{\partial x} \right)$$

$RH =$	Relative humidity	(-)
$t =$	Time	(s)
$x =$	Position	(m)
$D(RH) =$	Diffusion coefficient depending on RH	(m ² /s)
$\frac{\partial RH}{\partial x} =$	Relative humidity gradient	

Diffusion occurs when concentration levels of a matter are not uniformly distributed. This is valid for heat, dissolved particles in a liquid and for moisture in a porous medium.

The equations used for moisture transmission are equivalent to the equations used in thermodynamics. In other words, the laws for diffusion of mass are completely analogue with Fourier's law of heat conduction. Both are fluxes directly proportional to their concentration gradient. The use of the heat analysis as humidity analysis for concrete is proved to be successful by Holmes and West (Holmes & West, 2003). The full derivation of the flux theory and diffusion can be found in [Appendix C](#). In short, the used Fick's equations are based on the Gauss's difference Theorem.

Fick's 2nd law of diffusion for calculating RH values of pores in concrete has been used in numerous studies (Holmes & West, 2003) (Hajibabae, Grasley, & Ley, 2016) (Kang, Kim, Lee, Park, & Kim, 2012). An interesting publication is of Park, Kwon and Song as their publication includes both the theory of Kelvin-Laplace and of Fick's diffusion law. They have used Fick's non-linear diffusion equation as governing equation in their Finite Element model (Park et al., 2011). This is similar to the approach in this thesis.

Furthermore, Fick's law is prescribed by the Model code 2010 as method to address a transient diffusion phenomena. See section 5.1.12.2, formula (5.1-130) in volume 1 of the Model code 2010 (Fib bulletin 65, 2012).

2.6.1.1 Diffusion coefficient

The diffusion coefficient used in Fick's second law is depending on relative pore humidity and material parameters. Calculating the drying of concrete by diffusion, using the diffusion coefficient, was first published by Bažant and Najjar in 1971. They based their suggested formula on data fitting of experimental results. The experiments evaluated cylindrical and spherical specimens but also concrete slabs (Z.P. Bažant & Najjar, 1971).

The diffusion coefficient as presented than, is still used in the Model code 2010. Valid only for normal strength concrete and under isothermal conditions. These requirements are met in this thesis.

$$\text{Diffusion coefficient } D(RH) = D_1 \left[\alpha + \frac{1-\alpha}{1 + \left[\frac{(1-RH)}{(1-RH_c)} \right]^n} \right]$$

- $D_1 =$ is the maximum of $D(RH)$ for $RH = 1$ in m^2/s
 $D_0 =$ is the minimum of $D(RH)$ for $RH = 0$ in m^2/s
 $\alpha =$ $= D_0/D_1$
 $RH =$ is the relative pore humidity
 $RH_c =$ is the relative pore humidity at $D(RH) = 0.5D_1$
 $n =$ exponent characterizing the drop in diffusivity

The exponent n is a characterisation of the steep decreasing part in the non-linear $D(RH)$. According to Bažant and Najjar, the value is between $n = 6$ and $n = 16$.

Suggested values for the diffusion coefficient according to the Model code 2010 are:

- $\alpha =$ 0.05
 $RH_c =$ 0.80
 $n =$ 15

D_1 can be estimated by:

$$D_1 = \frac{D_{1,0}}{f_{cm} - 8} \quad \text{with } D_{1,0} = 1E - 08 \text{ (m}^2/\text{s) and } f_{cm} \text{ as mean compressive strength.}$$

These recommended values are used to determine the diffusion coefficient. The parameter α indicates that the diffusivity of wet concrete is 20 times higher than for dry concrete. Initial diffusivity is based on the characteristic compressive strength, $f_{ck} = f_{cm} - 8 \text{ MPa}$. Stronger concrete has a lower initial diffusivity. Material parameters from Table 8 are used.

The initial diffusion coefficient at an RH level of 95% is $D(0.95) = 3,33E - 10 \text{ (m}^2/\text{s)}$. At 65% RH the coefficient is $D(0.65) = 1,67E - 11 \text{ (m}^2/\text{s)}$.

This value is relatively close to the value for D_1 as determined by S. Kang et al. in 2012. For concrete with $w/c = 0.50$ they suggested a value of $D_1 = 6.28E - 10 \text{ (m}^2/\text{s)}$. Their study measured internal pore humidity levels with RH probes castes into the concrete (Kang et al., 2012).

In Figure 13, the course of the diffusion coefficients is seen. The brown line of the Model code is used in the FEM model.

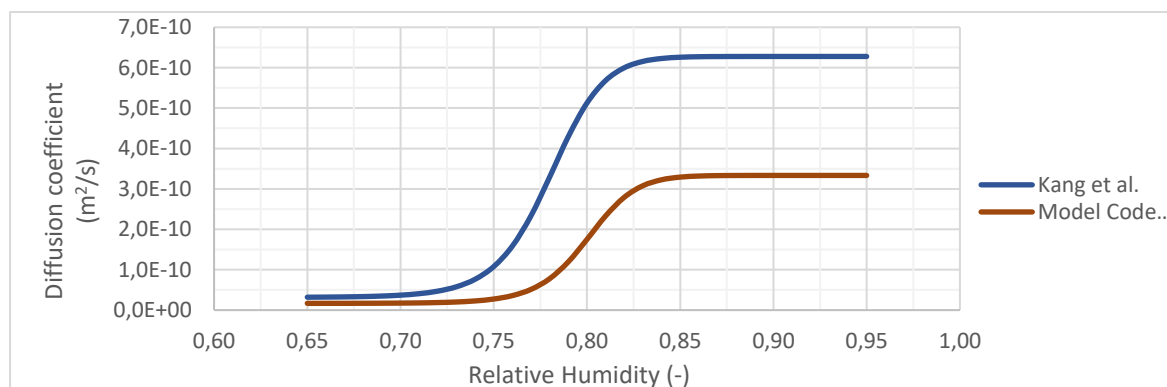


Figure 13. Diffusion coefficient used in Fick's 2nd law. Based on the Model code 2010 and from studies of Kang et al. For $w/c=0.50$ and drying at 20°C .

2.6.2 Fick's 1st law - flux

The outcome of Fick's 2nd law is a concentration at an specific point and moment in time. Fick's first law is used to calculate a mass flux through a material or at the surface of a material. The theory of Fick's first law is used by multiple researchers in their study to calculate drying shrinkage (Holmes & West, 2003)(Chen et al., 2019)(Abyaneh, Wong, & Buenfeld, 2016)(Kamali-Bernard, Bernard, & Prince, 2009) (Gamnitzer et al., 2019). In [Appendix C](#) the full theoretical and analytical derivation of Fick's first law is given.

At the surfaces, exposed to the ambient environment, transmission of moisture takes place through convection. This process of evaporation through the boundary surface is expressed by the convection coefficient (f). The driving mechanism is the difference in RH level at the surface of the element (φ_s) and the environment (φ_{en}). The moisture flux through the surface is:

$$J_s = f * (\varphi_s - \varphi_{en})$$

$J_s =$	Surface moisture flux	$(kg/m^2 \cdot s)$
$f =$	Surface evaporation rate	$(kg/m^2 \cdot s)$
$\varphi_s =$	Surface relative humidity	(-)
$\varphi_{en} =$	Environment relative humidity	(-)

Different approaches are used for the surface moisture flux in literature. D. Chen is using a 'surface moisture transfer coefficient' in m/s , multiplied with absolute concentration levels in kg/m^3 . In this thesis, the FEM calculation is based on RH-levels. Therefore, the surface evaporation rate is used (Chen et al., 2019).

The change in weight of the *test beam* during drying was measured. These results will be compared with the outcome of the FEM calculation using Fick's first law. When the FEM results for the boundary flux show good resemblance with the measured weight changes, this can act as a verification of the model. As the change of internal relative pore humidity was not measured and the model cannot be verified based on those results.

Change in total weight of the *test beam* due to surface evaporation through convection is:

$$\Delta kg = \sum (J_{s_i,t_j} \cdot \Delta t_j) \cdot S_{\text{testbeam}}$$

$J_{s_i,t_j} =$	Surface moisture flux of representative element i at time-step t_j
$\Delta t_j =$	Duration of time-step t_j

The flux at the surface of the concrete is determined using the evaporation nomograph of the American Concrete Institute. In this graph, the rate of evaporation of water from the concrete surface is related to ambient air temperature ($T_{air} = 293.15K$), ambient air relative humidity ($\varphi_{en} = 65\%$), concrete temperature ($T_{concrete} = 293.15K$) and the wind velocity ($V_{wind} = 0 \text{ km/h}$). For these values the surface evaporation rate is $f = 2.8E - 05 \text{ kg/m}^2/s$.

3 Finite element modelling

A finite element model is used to simulate moisture transport through concrete. The model is focussed on transport phenomena and not on material characteristics. A phenomenon as diffusion takes place at micro-scale level, whereas mechanical responses of the material are defined at a meso-scale. Design parameters used for the material are theoretically substantiated in the previous chapters.

An overview of the steps taken is presented in the flowchart diagram in Figure 3.

The concrete *test beam* is modelled in the finite element package of DIANA FEA. This specific package has been chosen based on the numerical possibilities and data exchange options. Furthermore, it is used in related studies and it is a well-known program at ABT. Aim of this thesis is to find a parametric and efficient FEM model to answer the research question.

Concrete structures have been modelled using FE approaches for decades (Rots, 1988). The publication of West and Holmes describes the first DIANA orientated study regarding concrete drying based on non-linear partial differential equations (Holmes & West, 2003).

Numerous researches have been done on drying of cementitious microstructures based on lattice modelling or lattice discrete particle modelling (Reybrouck, Wendner, Caspeepe, & Taerwe, 2009)(L. Liu et al., 2016). These approaches are competent for material research, but do not offer applicability in existing FEM packages and therefore lack direct structural implementation (Grassl, Wong, & Buenfeld, 2008).

In 2017, a user subroutine was created in DIANA by graduate student K. Nijs (Nijs, 2017). This subroutine added detailed shrinkage behaviour to the material model. However, it could only be used through cumbersome scripting. The finite element model in this thesis is also based on material parameters derived by HYMOSTRUC but integrated through user-interface modules.

The commands for the geometric model, material parameters, boundary conditions, used analysis and required outcome are all written in Python and were loaded into DIANA. Material parameters in this script were exported from tabular Microsoft Excel data. The Excel files contain the material calculation as described in the previous chapter.

Results of the finite element calculation are exported to a tabular file-type, which makes it suitable for post-processing in Notepad ++ and Excel. The graphs visualising the results are made in Excel.

In this chapter the set-up of the DIANA model is elaborated followed by the used calculation methods and at last the obtained results. Focus is solely on moisture diffusion, resulting in a strain valid for unrestrained concrete. Restrained concrete could crack under forced deformation. Integration of crack formation in a FEM model is theoretically substantiated in [Appendix D](#).

3.1 Model setup

The model is subjected to (initial) boundary conditions. These conditions are linked to the condition of drying. The *test beam* is air dried under indoor office conditions. Air humidity during drying is assumed to be 65% RH (Arboportaal, n.d.). The second finite element simulation is made at an relative low ambient RH of 50% (Pleysier, n.d.).

Internal initial relative humidity is $RH_{i,0} = 95\%$, which is before drying is initiated. The environmental RH is kept constant during the simulation $RH_{en} = 65\%$ and a second simulation with $RH_{en} = 50\%$.

This way the influence of the ambient relative humidity on drying can be evaluated.

The long term equilibrium condition is fairly straight forward to be calculated, as done in [2.5 Drying shrinkage at equilibrium](#). However, the development of relative pore humidity over time is more complicated as the difference between RH-levels is the driving force in the diffusion equation. Thus, the ambient RH is affecting the development of the internal RH distribution over time. For the lower ambient RH of 50%, a faster decrease of relative pore humidity is expected and therefore a faster drying shrinkage strain development.

3.1.1 Finite elements

The model is composed of a single solid material, concrete, with the diffusive parameters as determined in this thesis. To analyse the moisture transport through the material, based on the heat equation, specific finite elements are needed.

The object is modelled using two types of finite elements. Internal transport takes place in solid brick elements and the moisture exchange with the surrounding is taking place through boundary elements.

For the body of the *test beam* twenty-node quadratic solid brick elements are used. The twenty nodes are positioned on the eight corners of each brick type element and at the mid-length of the twelve ribs. These elements are capable on non-linear analysis.

The moisture exchange with the environment is modelled by a general potential flow element. This four-node element is capable of describing three-dimensional flows.

In Figure 14, the used elements are illustrated (DIANA - Finite Element Analysis, 2017).

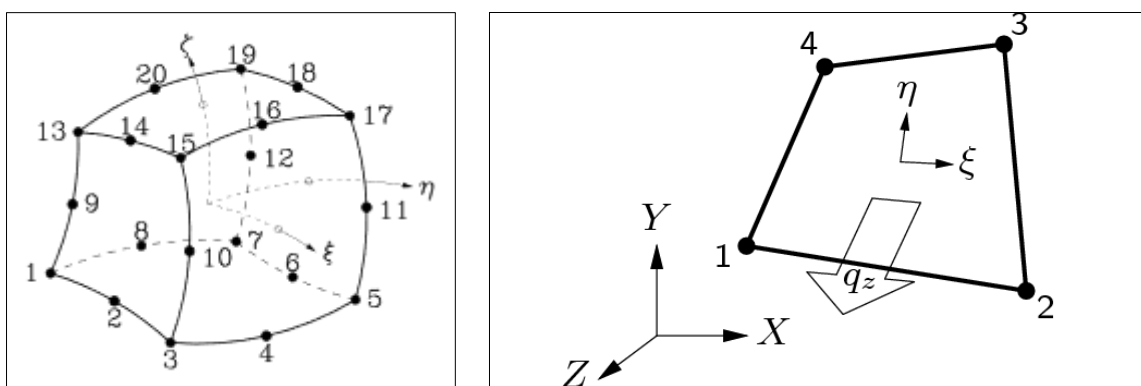


Figure 14. left) Twenty-node solid brick element. right) Four-node potential flow boundary element

3.1.2 Mesh size

For numerical analysis of the material, the model is discretized into a finite amount of elements. As explained, these elements are of the solid and boundary types. The size of the discretized elements is determined based on the ability to accurately describe shrinkage.

Based on the low diffusivity of the material, it is expected that a relatively small mesh size is needed for a reliable outcome. The outcome should be a result of the structural response and not a result depending on the chosen mesh size. In other words, a mesh-independent model is required. An optimum mesh size is a trade-off between calculation accuracy and computational power. When further densification of the mesh does not significantly change the outcome of the calculation, the correct mesh size is found.

During the development phase of the model, trial simulations were ran to select the right mesh size. Starting at a relative course distribution, proceeding to a more refined distribution. During refining of the mesh, a shift of the diffusion front was occurring. The part with the strongest change of relative pore humidity shifted towards the surface of the model. Furthermore, it was noticed that with a coarser mesh-distribution, the moisture diffusion through the specimen seems to evolve at a higher speed than with a dense distribution. This is a misleading outcome based on the coarser meshed being used. In a coarse mesh, a linear distribution seems present but in fact a linearization between integration points is seen. Hence, the amount of integration points is not sufficient.

The trial simulations can be found in [Appendix G](#).

Stable and reliable results were found by taking a representative part of the *test beam* and by modelling this in greater detail. The full model is divided into 80 slices. One of them is analysed, called the *slice* model. On this model, the same boundary conditions are applied at the perimeter. Hence, the general boundary flow elements are not present at the sliced surface of the *slice* model. The mesh distribution is shown in Figure 15. For the results of the full model, moisture flux through the exposed 'head' of the *test beam* is included.

The effect of mesh refinement is shown in [Appendix G](#). For the *slice* model, the mesh size is set to 0.0015 m.

The amount of elements used in the analysed *slice* model, is presented in Table 4. Without dividing the model into slices, the total amount of elements needed would be 4.170.000. This strategy reduces the total elements needed for the same result to 52.000, a reduction of 98.75 %. The *slice* model has a computational time of 10 minutes. Simulating the whole model at once, would take 13.5 hours.

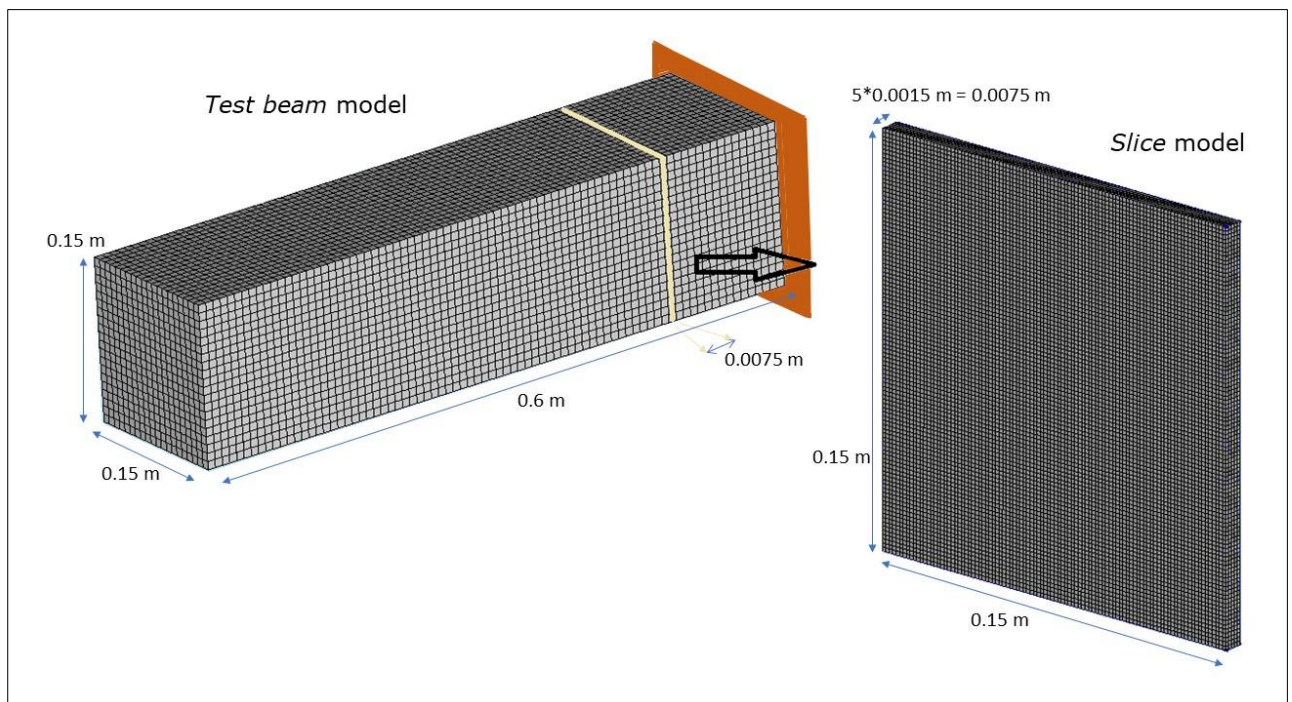


Figure 15. Mesh distribution of test beam model and associated slice model.

			<i>Slice model</i>	<i>Full test beam model</i>
	Type	Mesh size	Amount	Amount
Solid element	CHX60	0.0015 m	50.000	$50.000 * 80 = 4.000.000$
Boundary element	BQ4HT	0.0015 m	2.000	$2.000 * 80 = 160.000$ $+ 10.000$ 'head' elements = 170.000
			<i>total</i> = 52.000 elements	<i>total</i> = 4.170.000 elements

Table 4. Mesh size of FEM model.

3.2 Equations used

The diffusion of moisture is modelled with the heat equation as governing equation. Diffusion of moisture through a drying specimen cannot be modelled directly in DIANA FEA. Therefore, the 'Energy balance equation' of DIANA FEA is used. This equation can be used through the user interface of the program. As explained earlier, Fick's law of diffusion is analogue to the heat equation. See [Appendix C](#) for the full derivation of Fick's second law and the substantiation of the analogy with the heat equation. Instead of temperature (T), relative humidity (RH) is used.

Energy balance equation:
$$c \frac{\partial T}{\partial t} = \text{div}(k \vec{grad} T + \vec{v}T) + q_v$$

c = thermal capacity
 T = temperature
 t = time
 k = thermal conductivity
 $\vec{v}T$ = convective flux
 q_v = source or sink

For internal diffusion, convective fluxes and sources or sinks are disregarded. The reason is given in chapter [2.6.1 Fick's 2nd law – diffusion](#). Resulting in an equation used in the DIANA FEA model:

Energy balance equation:
$$c \frac{\partial T}{\partial t} = \text{div}(k \vec{grad} T)$$

(no convection, no source or sink)

c = thermal capacity (J/m³K)
 T = temperature (K)
 t = time (s)
 k = thermal conductivity (W/m K)

In this study, temperature is replaced by relative humidity. Furthermore, thermal capacity(J/m³K) and thermal conductivity(W/mK) are not used in Fick's 2nd law of diffusion, but instead diffusivity(m²/s) is used. The relation between the parameters used in the energy balance equation and Fick's diffusion law is described by K. van Breugel.

K. van Breugel uses the thermal differential of Fourier. Here this notation is taken over without thermal source. Full analogy with Fick's second law of diffusion is present.

K. van Breugel diffusion equation:
$$\frac{\partial T}{\partial t} = \alpha_c \cdot \left[\frac{\partial^2 T}{\partial x^2} + \frac{\partial^2 T}{\partial y^2} + \frac{\partial^2 T}{\partial z^2} \right]$$

With α_c (m²/s) being the 'temperature levelling coefficient.

$$\alpha_c = \frac{\lambda_c}{\rho_c \cdot c_c}$$

λ_c = heat conduction coefficient (W/m K)
 c_c = specific heat of concrete (J/kg K)
 ρ_c = specific mass of concrete (kg/m³)

The only difference between DIANA and K. van Breugel is the usage of thermal capacity, being the specific heat of concrete multiplied with the specific mass of concrete. However, this results in the same energy balance equation used for modelling. Dividing k over c makes the diffusion coefficient.

$$\frac{k}{c} = D(RH) \quad \rightarrow \quad \frac{W/m K}{J/m^3 K} = \frac{(J/s)/m K}{J/m^3 K} = m^2/s$$

Based on reasoning explained here, the heat equation in DIANA FEA can be used for moisture diffusion based on Fick's second law.

$$\frac{\partial T}{\partial t} = \text{div} \left(\frac{k}{c} \vec{grad} T \right) \quad \rightarrow \quad \frac{\partial RH}{\partial t} = \frac{\partial}{\partial x} \left(D(RH) \frac{\partial RH}{\partial x} \right)$$

The relation of the changing diffusion coefficient to the RH is captured in a dependency relation of the thermal conductivity. The change of diffusivity, as is used in the DIANA simulation, is covered in part [2.6.1.1 Diffusion coefficient](#). As input in DIANA the values of the diffusion coefficient are given to k , the value is multiplied with $c = 75$. In the latter formula it can be seen why this multiplication is done. DIANA input commands can be found in [Appendix I](#).

Flux through the boundary-flow elements is given by the moisture formula as presented in chapter [2.6.2 Fick's 1st law - flux](#):

$$J_s = f * (\varphi_s - \varphi_{en})$$

The surface flux, J_s ($kg/m^2 \cdot s$) is depending on the surface evaporation rate f ($kg/m^2 \cdot s$) and the differences in relative humidity between the concrete surface and ambient air.

Discharge of moisture from the modelled system is governed by convection. According to the analogue heat flow theory, the parameter used is the (surface) heat transfer coefficient.

The value set for the heat transfer coefficient is the surface evaporation rate for moisture.

Detailed justification of this action is given in [Appendix E](#).

The heat transfer coefficient (rate of evaporation) is not affected by the surface potential in the simulations. The transient change in the parameter for surface evaporation is not significant compared to the potential dependency of the moisture diffusion through the material. Therefore, a potential dependency is included in the diffusion coefficient, but not for the surface evaporation. In this way, the effect of the key parameter is seen clear in the outcome and is not polluted with noise of other changing parameters.

3.2.1 Method of solving: Transient Heat Analysis

The formulas in the previous chapter are ran in DIANA using the suited numerical method, the transient heat analysis. In this analysis, the initial temperature of the material and the environmental temperature are used as starting point. The conditions at the boundary of the domain and classified as a Dirichlet boundary condition.

Step sizes of the calculation are chosen based on expected change in the system. At the beginning, the diffusion will be at a higher phase than in the later stage. Therefore, the time-steps are shorter in the beginning. A total of 35 time-steps are used. The first 28 steps account for the 84-days of drying of the *test beam*. These values are needed to compare the simulation with the experimentally obtained data. Seven more steps prolong the simulated drying time till 10 years.

For the nonlinear analysis, the incremental iterative method of Newton-Regular is used for solving the equation. The amount of iterations per time step is set to a maximum of 5, with a convergence tolerance of 1E-6.

Method of solving is Parallel Direct Sparse with a tolerance of 1E-8. The method of Euler backward is used for the integration over time. This method has a time integration parameter $\alpha = 1$. Both setting are set by default for nonlinear analysis (DIANA - Finite Element Analysis, 2017).

An analytical approach for solving this finite element problem is substantiated in [Appendix F](#).

The required output from the chosen analysis is the heat flux. This flux is analogue to the moisture flux by diffusion. Furthermore, the temperature is analogue to the relative humidity.

Fluxes are results given per element while temperature is a nodal results. Specific boundary heat flux is only a solution for the associated boundary elements.

3.3 Finite element results

The goal is to model the development of drying shrinkage over time depending on the concrete type and environmental conditions. For this, a section of the *test beam* has been modelled in detail. This model contains 52.000 elements and 230.000 nodes. A selection of nodes and elements is made, which are used for post-processing. These chosen nodes are representative for the internal changes during drying. Therefore, the deformation, based on the values of these nodes, is accurate. The nodes are selected on a cross sectional cut, based on their average result over time. In [Appendix H](#), the selection of the mean nodes is substantiated. The produced data in the FEM simulation is exported from the DIANA environment in tabular files by using the procedure and commands found in [Appendix J](#).

3.3.1 Drying in FE simulation

The *test beam* is subjected to drying during the time period, starting at 28-days till 112 days. In DIANA, the 84 days of drying are simulated. Over time, the internal relative humidity will make equilibrium with the external relative humidity. The change of internal RH during the 84 days of drying will be used to calculate the related drying shrinkage strain.

The four mean nodes visualise the change of RH at the surface, centre and of two nodes representing the average of a straight- and a diagonal cross-sectional cut. A graphical result of the RH-levels is shown in Figure 16. The concrete has an initial internal relative pore humidity of 65% and an external relative humidity of 95%.

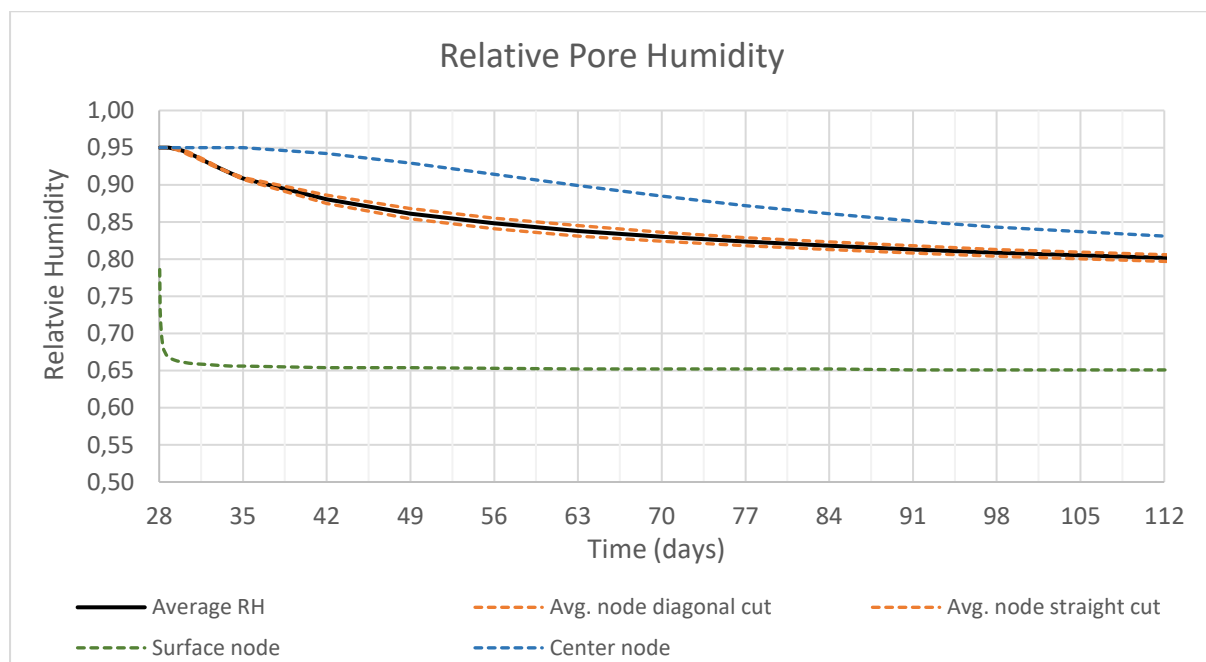


Figure 16. Internal relative humidity of concrete pore during drying based on the FEM model. Time period 28 days – 112 days and $RH_{external}=65\%$.

It is observable that the decrease of relative pore humidity is progressing most rapid as the concrete is exposed to drying. This is related to the decrease in potential, as the internal and external RH-levels are equalising. Based on the nonlinear diffusion coefficient used in Fick's 2nd law, a strong decrease in speed of drying was expected from a RH-level of about 0.82.

This effect is not visible on the time scale used in this observation.

Nodes located at the surface quickly reach equilibrium with the external 65% RH. The core of the object has the slowest decrease of relative humidity, as the distance to the surface is the longest. The two averages taken from a straight- and diagonal section cut do not show much difference. From the graph, it is deduced that no equilibrium is reached during the 84 days of drying. After this time, the relative pore humidity of the concrete is still decreasing.

When the full 10-years of simulated drying time is displayed, long-term drying can be analysed. (Figure 17)

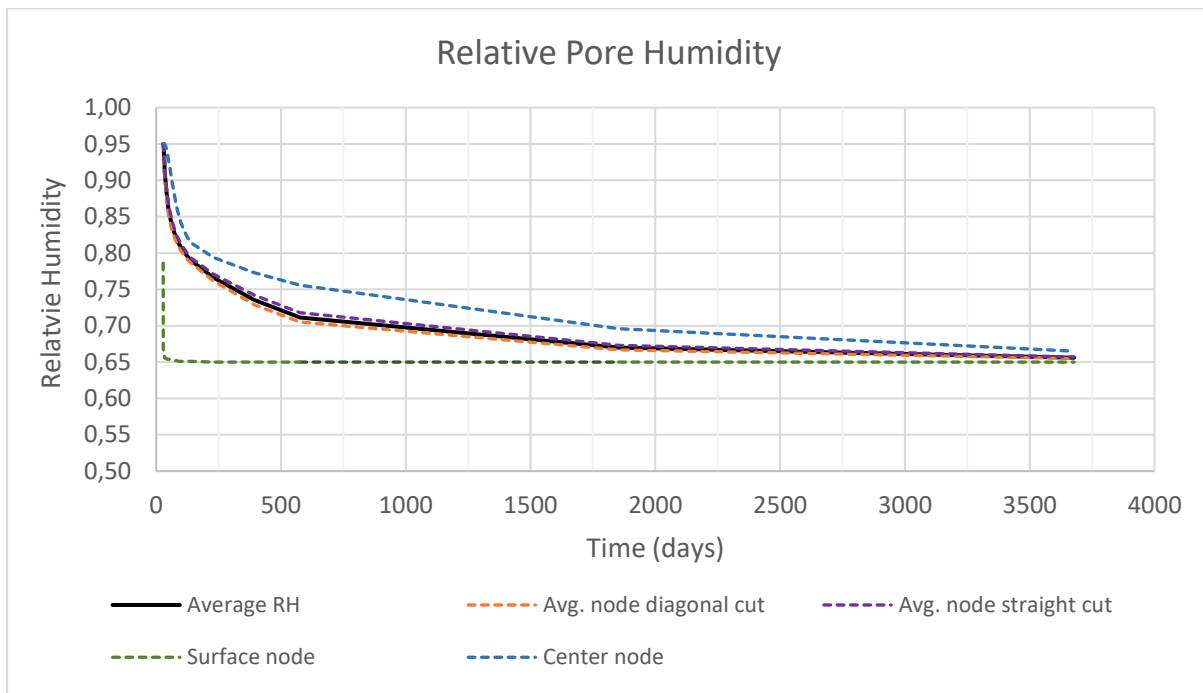


Figure 17. Internal relative humidity of concrete pores during drying, based on FEM model. Time period 28 days - 10 years and $RH_{external}=65\%$.

An stable equilibrium through the cross-section of the concrete beam is still not reached after 10 years. However, after 2000 days (5.5 years), an acceptable convergence is reached. At that moment, 93% of drying has occurred in the simulation. After 10 years, 99.1 % of the full equilibrium is met.

In the graph, some slight angular transitions are visible. These transitions are due to time-step accuracy in the simulation.

The same simulation is ran for an external relative humidity of 50%. Which is equivalent to a relative dry indoor office climate, as stipulated in [3.1 Model setup](#).

The results of this simulation are shown in Figure 18, for the time period of 28 days to 112 days. In Figure 19, the drying period of 28 days to 10 years is presented.

The evolution of the drying curve in the situation with a lower external relative humidity is comparable. Except that the equilibrium condition, which is met at 50% RH instead of 65% RH. When comparing both conditions, a difference in RH-levels is only significant on the long term. The first 84 days of drying are of interest in this study. During this time, the difference in RH-levels at the 112th day is only 4.1%. The reason that these outcomes are close to the equivalent might be the influence of the diffusion coefficient. As the potential in RH-levels has clearly a limited influence on drying during this time period.

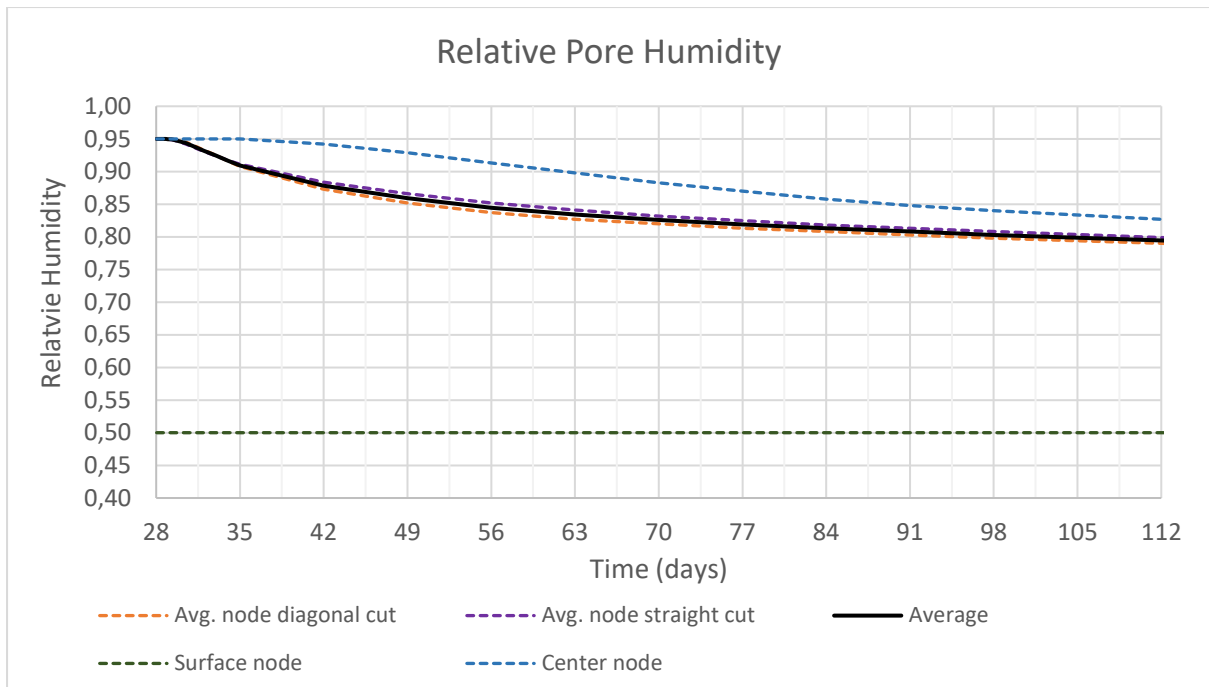


Figure 18. Internal relative humidity of concrete pores during drying, based on FEM model. Time period 28 days - 112 days and $RH_{external} = 50\%$.

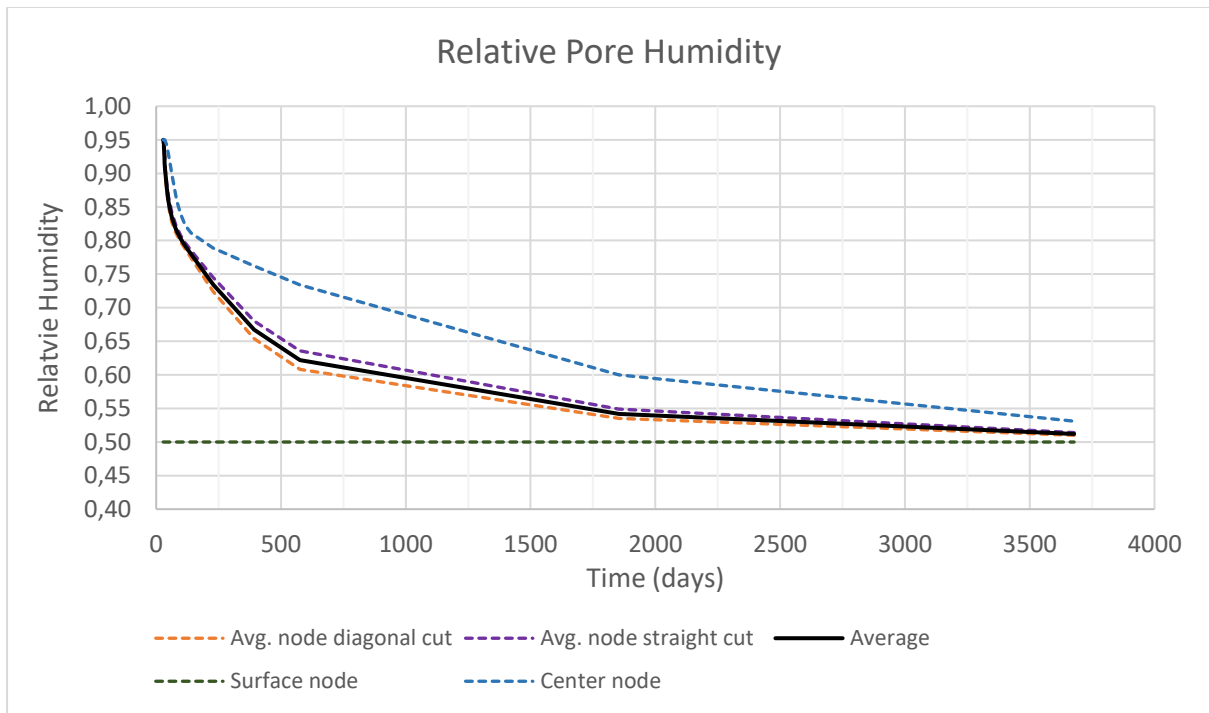


Figure 19. Internal relative humidity of concrete pores during drying, based on FEM model. Time period 28 days - 10 years and $RH_{external} = 50\%$.

3.3.2 Drying shrinkage strain

The change of relative pore humidity is now coupled to the theory of drying and shrinkage. As prescribed by the steps in the flowchart of Figure 3.

In Figure 20, the drying shrinkage of cement paste and concrete is presented. The graph contains the course of drying shrinkage for concrete exposed to 65% and 50% of external relative humidity.

These results are the product of combining the FEM results of diffusion with the theoretical laws of Kelvin, Laplace, Bentz and Powers’.

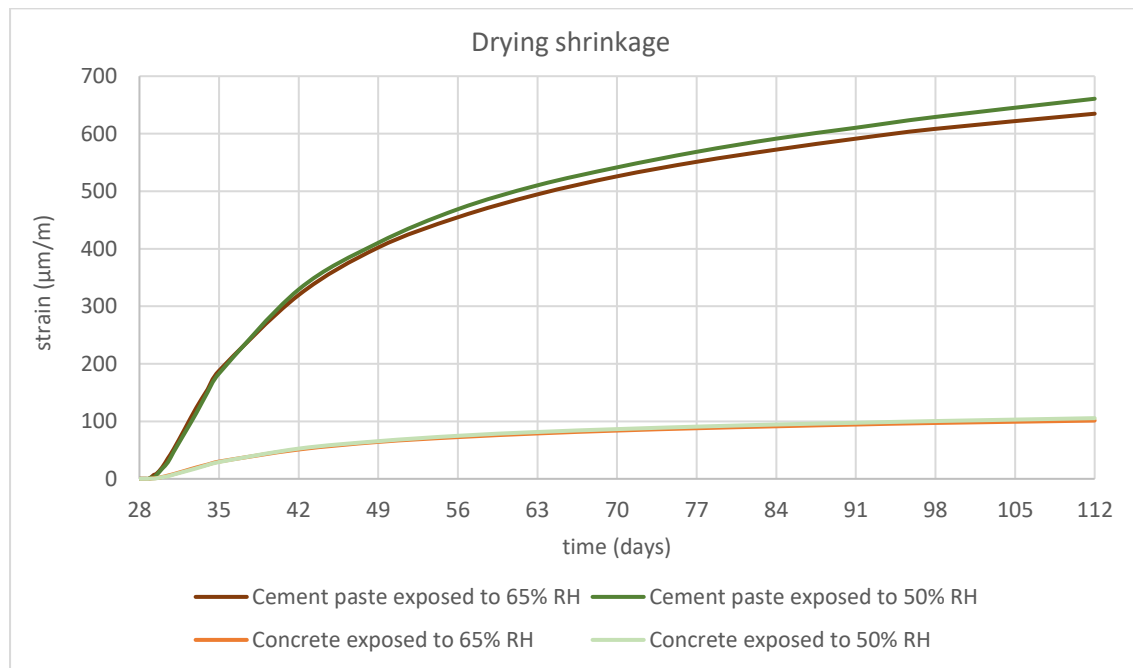


Figure 20. Drying shrinkage strain of cement paste and concrete. 112-days for $RH_{\text{external}}=65\%$ and $RH_{\text{external}}=50\%$.

The course of the graph is as expected. Drying proceeds faster at the beginning and proceeds at a slower phase afterwards. For the situation with an external RH of 65%, the cement paste shrinkage due to drying is 635 $\mu\text{m}/\text{m}$ at the 112th day and of concrete it is 101 $\mu\text{m}/\text{m}$. The situation with an external RH of 50% results in paste shrinkage of 660 $\mu\text{m}/\text{m}$ and 105 $\mu\text{m}/\text{m}$ for concrete. This 4% of difference in strain due to the change in external relative humidity is not significant. A difference in this small order was expected based on the comparable RH-profiles presented in [3.3.1 Drying in FE simulation](#).

Shrinkage of the concrete is only 16% of the cement paste deformation, based on the restraining effect of aggregates according to Pickett’s model. The internal restraint formed by the aggregates is of major influence.

The results of the simulation with an external RH of 65% will be used as main result. This is chosen based on the small difference in outcome and a RH of 65% is a normal indoor climate.

The strain results in Figure 20 are normalised. Drying of the pores starts at a RH-level of 95% at t_0 (= 28 days). In the theoretical used model, a strain is already present at RH=95%. These models calculate a rise in capillary pressure starting from RH 100%. Therefore, the theoretically calculated values are deducted with the strain present at RH=95%. If this action would not be performed, the results would include both drying and autogenous shrinkage. The difference in results is seen in the graph of Figure 21. According to these findings the autogenous shrinkage part is accountable for 25% of the total after 112 days.

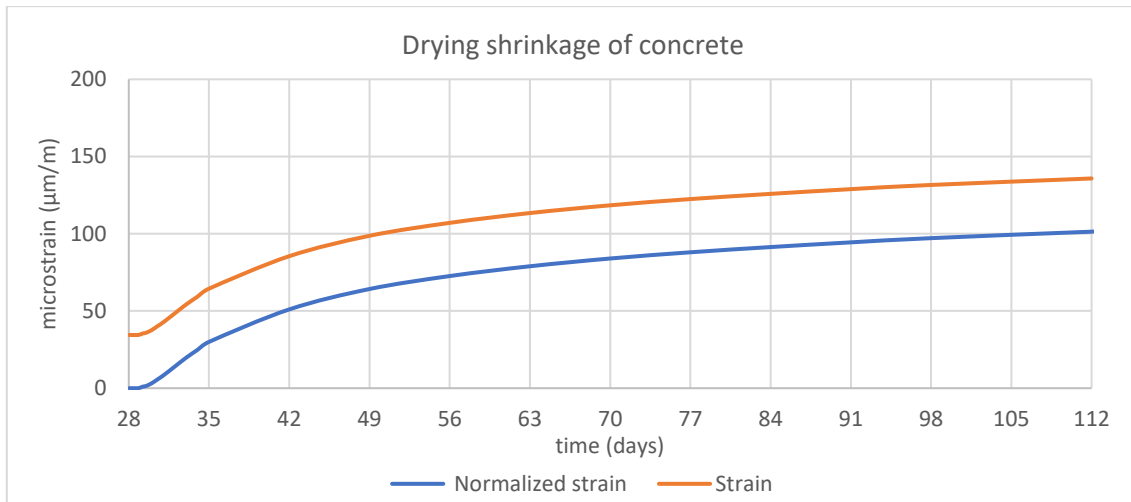


Figure 21. Normalised drying shrinkage of concrete. $RH_{external} = 65\%$.

For the FEM simulation of the RH-profile, convergence is met after 2000 days. The shrinkage development at this moment in time is $1075 \mu m/m$ for cement paste and $173 \mu m/m$ for concrete at exposure to $RH_{external} = 65\%$. For $RH_{external} = 50\%$ the strain in cement paste is $1380 \mu m/m$ and in concrete $220 \mu m/m$. The drying shrinkage development over a time period of 10 years is given in Figure 22.

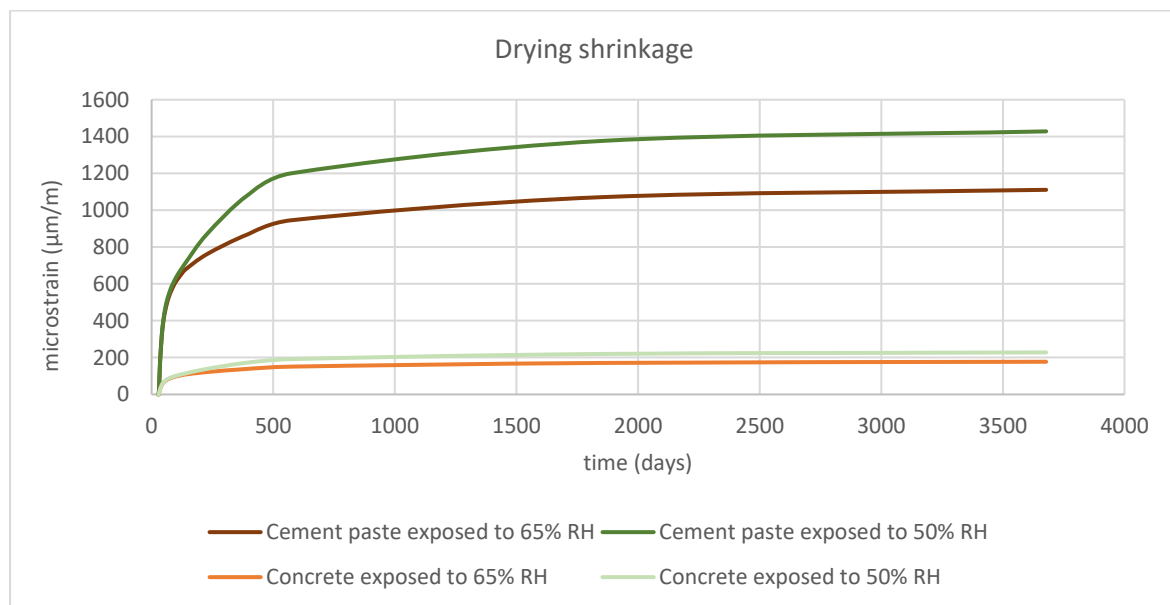


Figure 22. Drying shrinkage strain of cement paste and concrete. 10-years for $RH_{external} = 65\%$ and $RH_{external} = 50\%$.

As seen in Figure 20, paste shrinkage reaches about $650 \mu m/m$ after 84 days of drying. In Figure 22, it is clearly seen that the environmental RH-level has an effect on the long term shrinkage. Over a longer period of time the difference in strain due to drying shrinkage becomes relevant.

3.3.2 Boundary flux

At the boundary of the object, moisture is evaporating from the surface. This flux is modelled in DIANA. For a concrete beam exposed to $RH_{\text{external}}=65\%$, the average flux through the surface is as presented in Figure 23. The average is based on the elemental result of one of the *test beam* sides.

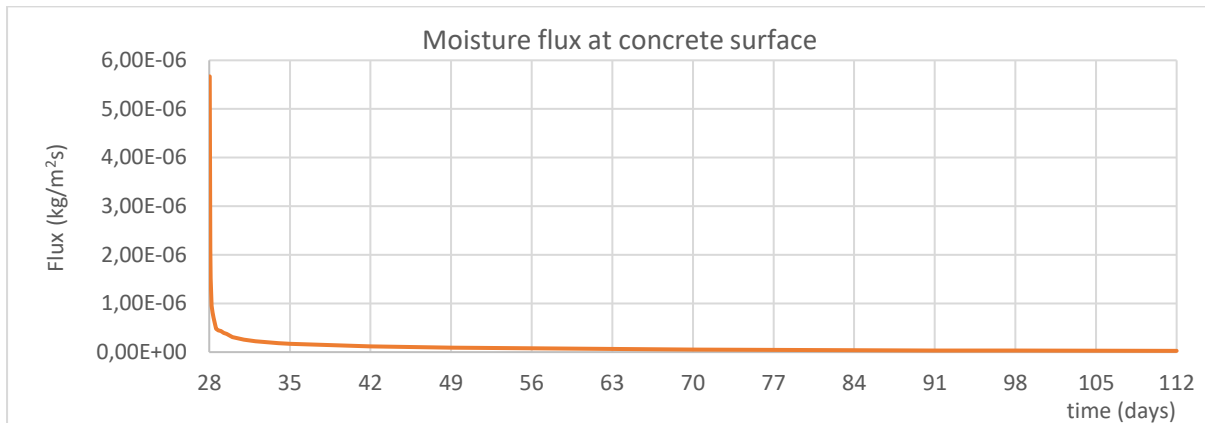


Figure 23. Average moisture flux at the concrete surface during drying. $RH_{\text{external}} = 65\%$.

The RH-levels at the surface of the concrete levels quickly with the surrounding air. After this event, the 'drying-front' penetrates inwards to the centre of the concrete beam. Within the first days, the relative pore humidity of the material close to the surface is in equilibrium with RH_{external} . These events change the surface flux drastically. Within half of the first day, the flux decreases by fivefold. The change of boundary flux is better understood on a shorter time scale. In Figure 24, the flux is shown for the first two days.

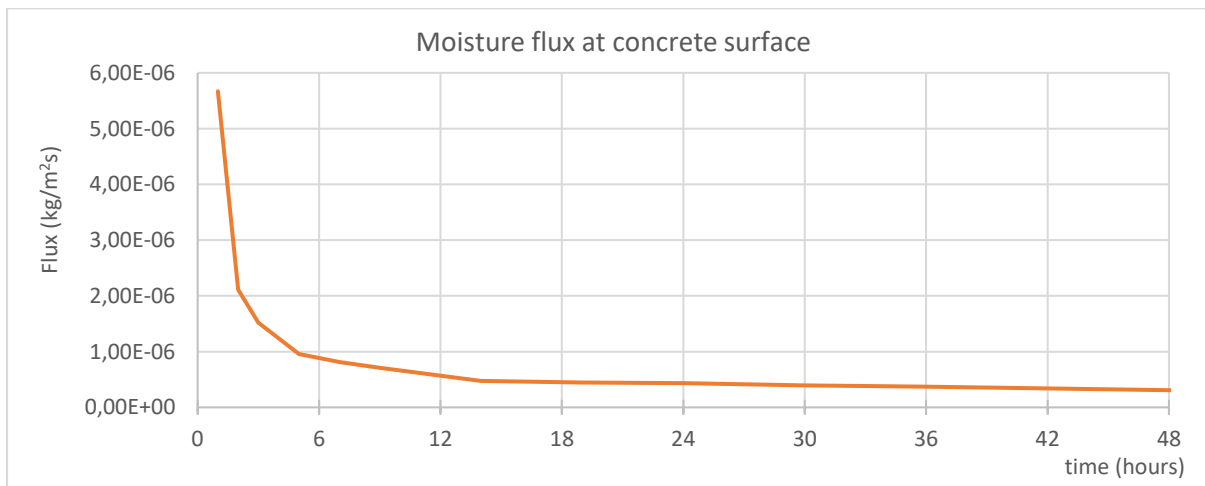


Figure 24. Average moisture flux at the concrete surface during the first 48 hours of drying. $RH_{\text{external}} = 65\%$.

From these graphs it can be concluded that the rate of evaporation (f) is not normative for the drying of the concrete. The rate of evaporation is used in Fick's first law to calculate the surface flux. The supply of water from the inner concrete to the surface is normative. Diffusion of moisture through the material is relatively slow compared to the surface evaporation. Hence, the surface evaporation rate does not influence the diffusion of elements attached to the surface boundary elements.

By calculating the surface area of the flux-graph in Figure 23, the total loss of moisture during drying is determined. This is done by multiplying the flux at a given time-step with the duration of the time-step. Flux through the exposed 'head surface' of the *test beam* is slightly higher during the first days of drying compared to the sides. After a few days, the head flux becomes smaller compared to the sides. This can be explained by the fact that the elements located close to the head surface have a short distance to the surface of the object than elements located in the centre. 90% Of the moisture flux went through the exposed sides during drying and 10% through the head.

Initial water content of the pore structure is modelled as thermal capacity in DIANA. The value of water content is assigned to thermal capacity as the transient heat analysis is used in the FEM model. The analogy is explained in chapter 3.2 'Equations used'. This initial water content is determined by diminishing the amount of water in the concrete mixture by the theoretically consumed water by hydration. It is assumed that a water/cement-ratio of 0.38 is needed for full hydration (Holt, 2001). From Table 9 it is known that the used w/c-ratio of the *test beams* is 0.5. The cement content is 350 kg/m^3 and the water content in the mixture is 175 kg/m^3 .

According to this theory, 133 kg of water is needed for full hydration. HYMOSTRUC calculated an degree of hydration of $\alpha = 0.74$. This makes 98.5 kg of consumed water during the first 28-days of hydration. Therefore, the initial water content in the pore structure is estimated to be $175 \text{ kg} - 98.5 \text{ kg} = 76.5 \text{ kg}$. The capacity of the material in DIANA is given 75 kg/m^3 . Based on the dimensions of the *test beam*, the beam has 1 kg of free water at the start of the drying simulations.

During 84 days of drying with normal exposure to $RH_{external} = 65\%$, the concrete has lost 0.174 kg in the simulation. This is 17% of the initial free water content. The measured change in weight during drying was 0.190 kg . This is 8% more than the simulated drying.

When the drying time in simulation is prolonged to 10 years under normal drying conditions, the change in weight due to drying is 0.312 kg , being 31% of the initial free water content. The result is displayed in Figure 25. For the development of shrinkage, it was concluded that after 2000 days acceptable convergence is reached. Over this period of time, the *test beam* has lost 0.298 kg . Which is equal to the loss of 30% of the initial water content.

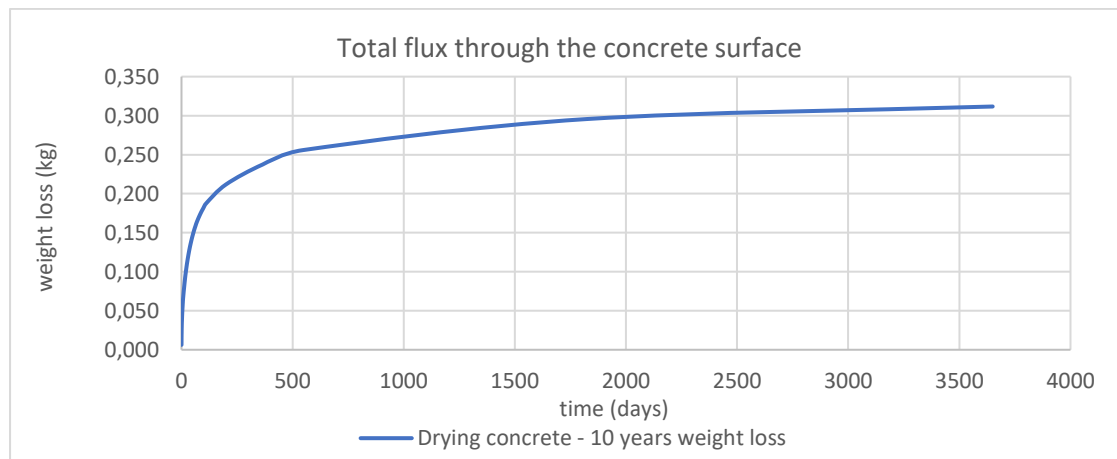


Figure 25. Change of weight over a time period of 10 years. Concrete exposed to $RH_{external}=65\%$

The *test beams* of ABT were oven dried after the 112th day. In the oven, excess water left in the pore structure of the concrete will evaporate. After oven-drying the total change of weight is 0.726 kg for the *test beams*. Hence, 73% of the initial free water has evaporated.

The oven-drying step is simulated in DIANA by exposing the material to a theoretical $RH_{external} = 0\%$. During a 10 year simulation, 0.940 kg of water has evaporated.

This is 92% of the water present in the pore structure at the start of the simulation.

4 Discussion of results

In this chapter, the results of the finite element analysis are compared to the measurements of the *test beam* and discussed. The outcome is also related to the Eurocode and Model code calculation.

At first, the FEM results of concrete shrinkage strain is plotted against the change in weight, see Figure 26. A linear relation is observed. This finding is in line with published results in literature (R.M. Mors, 2011). This graph presents the result for concrete, as this is the material of the *test beam*. When cement paste would be observed, the linear curve would have had a higher inclination.

The relation between strain and loss in weight due to drying is linear. However, the change over time is nonlinear.

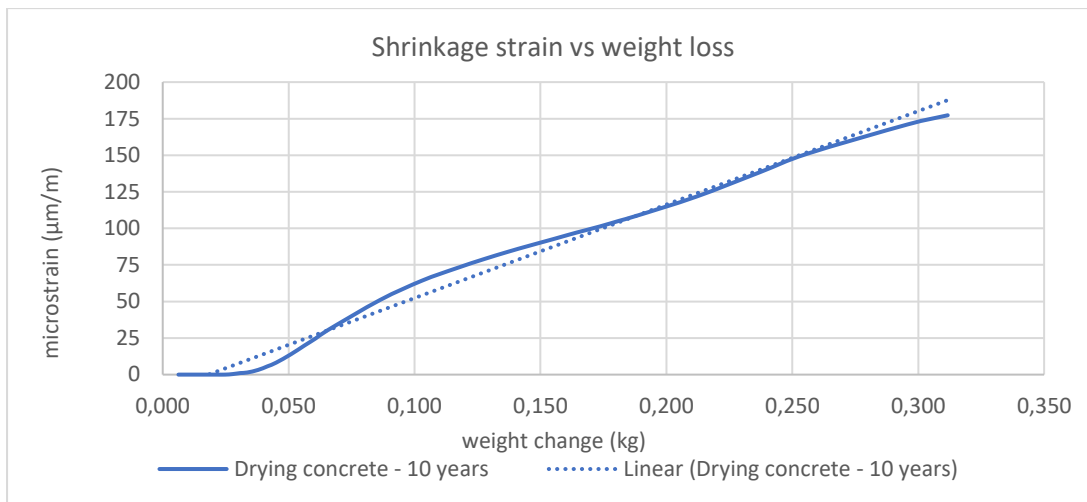


Figure 26. Shrinkage strain plotted against change in weight based on FEM results.

The results presented in Figure 26 are valid for concrete exposed to $RH_{external} = 65\%$. During the first 84 days of drying the simulated drying can be related to the measured data, as done in [3.3.2 Boundary flux](#). The difference between the simulation and measured data was 8% after 84-days.

When oven-drying conditions were simulated for the *test beam*, the differences were larger. The difference between measurements and the simulation is 23%. A higher loss of mass is found in the FEM simulation. A possible explanation for this difference is based on the theory of hydration. In the FEM model, all water present at the start of the simulation is modelled as 'free-water'. This is the amount of water in the raw-mixture minus the amount of water needed for hydration till the 28th day. However, in real concrete the process of hydration still continues after the 28th day and water is consumed in this process. Thus at the moment of oven-drying less free water is present in the concrete than in the material simulated in FEM.

The simulated drying shrinkage in FEM is compared to the measurements in Figure 27. At the 112th day of drying, the concrete shrinkage of the FEM simulation is $110 \mu\text{m}/\text{m}$ and the average shrinkage of the concrete *test beams* is $226 \mu\text{m}/\text{m}$. The dashed lines represents measured microstrain of the prisms. The FEM model for concrete shrinkage is based on Pickett's model for the restraining effect of aggregates.

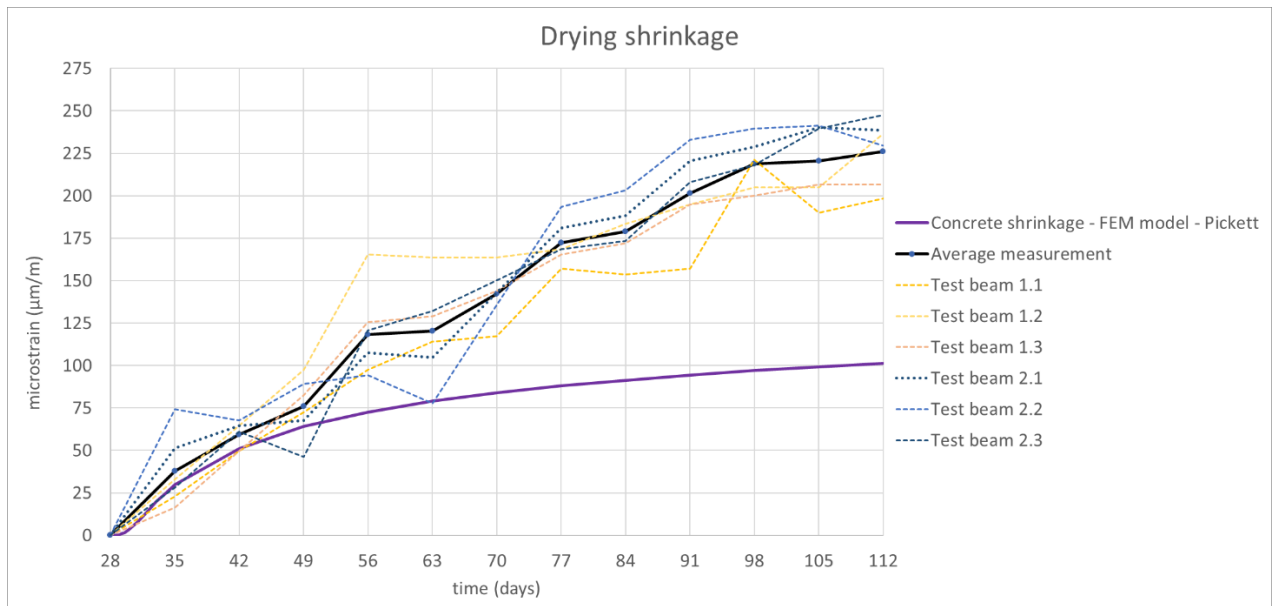


Figure 27. FEM result and shrinkage measurement of the test beams.

The difference between the FEM outcome and the measured shrinkage is significant. Multiple explanations for this difference are possible. The most likely reasons are given in three statements.

Firstly, in the calculation Pickett's model is used to includes the restraining effect of aggregates on the deformation of cement paste.

A similar model exists by Neville and Brooks, suggesting a correction factor of $n = 1.2 \sim 1.7$ in their calculation. This is covered in chapter [I.6.4.1.3 Influence of aggregates](#).

The key equation for concrete shrinkage is: $\epsilon_c = (1 - a)^n \cdot \epsilon_{HCP}$. However, the presented results are based on a calculation using Pickett's model, which produced a $\beta = 1.51$. This factor is used in the same calculation ($n = \beta$).

Using the lower-bound correction factor ($n = 1.2$) of Neville and Brooks reduces the restraining effect of aggregates.

Secondly, the results are based on drying shrinkage. These are calculated using the relative pore humidity, starting at RH=95%. The first 5% are used for cement hydration. However, according to the theoretical models used, shrinkage strain develops as soon as the relative pore humidity drops below 100%. To exclude the shrinkage during hydration, the calculated values are normalised at RH=95%. During hydration, autogenous and chemical shrinkage develops. The measurement of the beams of ABT starts after a curing period of 28 days. It is possible that autogenous shrinkage still develops after this time, as hydration is ongoing after the 28th day.

Furthermore, the 5% drop of RH is based on a numerical simulation of cement hydration. The normalisation based on this simulation does decrease the concrete shrinkage with 25% at the 112th day of drying. Without this normalisation, shrinkage values will be higher.

A third explanations could be found in the presence of microcracks in real concrete. Improving the level of diffusivity through the cement matrix and locally at aggregates through the ITZ (see [I.6.4.1.3 Influence of aggregates](#)).

In the graph of Figure 28, the effect of these two statements is visualised. The new graphs are called 'Concrete shrinkage -FEM model - Neville' and 'Concrete shrinkage -FEM model - Neville + No normalisation'. Also the cement paste shrinkage is displayed. This visualises the effect of the calculation on aggregate restraint. Cement paste shrinkage is the actual result of the FEM calculation on moisture diffusion and used in the laws of Kelvin, Laplace and Bentz. The aggregate restraint is based on the theory of Pickett and Neville.

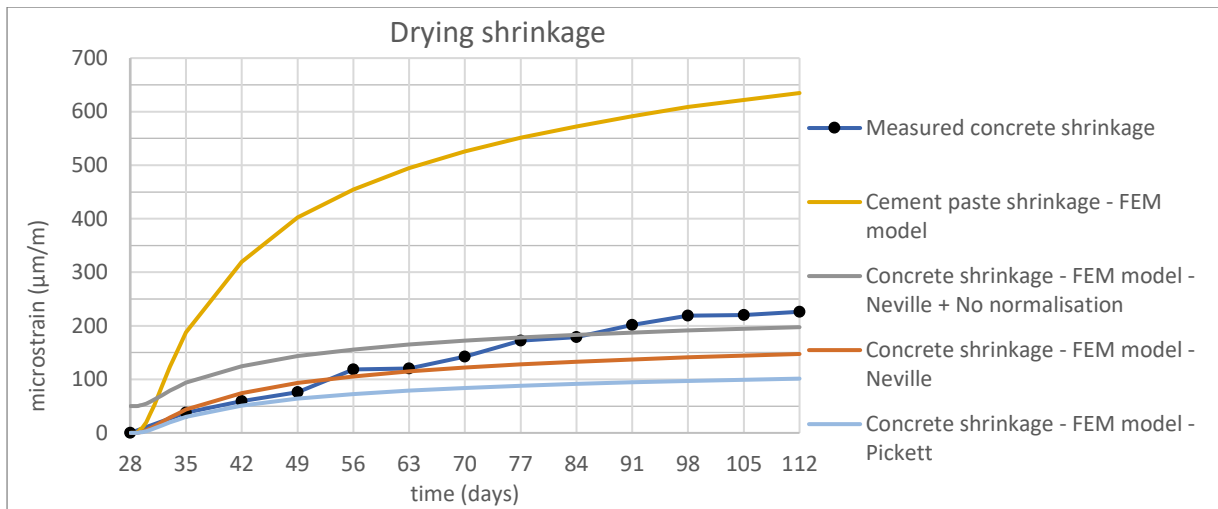


Figure 28. FEM results of cement paste and concrete with different levels of aggregate restraint.

Based on the graph, it can be concluded that the applied approach in this thesis of modelling cement paste based on FEM simulation and theoretical laws is feasible. The normalised concrete strain does follow the measured increment during the first weeks.

However, the influence of aggregates is large and can cause significant spread in the outcome. Including the initial strain is not a solution, as the focus is solely on drying shrinkage. The 'Concrete shrinkage – FEM model - Neville' is chosen as recommended model. In Neville's model, 23% of paste shrinkage is translated to concrete shrinkage.

Figure 29 presents the results of the developed drying shrinkage model in this thesis together with the actual measured deformation, the Eurocode and Model code. As presented in [Appendix II: Codes & Structural conditions](#).

A reason for the codes overestimating the shrinkage of the *test beam* could be due to the 28-day hydration of the concrete in a climate chamber. Resulting in a higher stiffness of the cement skeleton compared to ordinary concrete poured at a construction site. Based on Hooke's law, less strain will develop in a stiffer material.

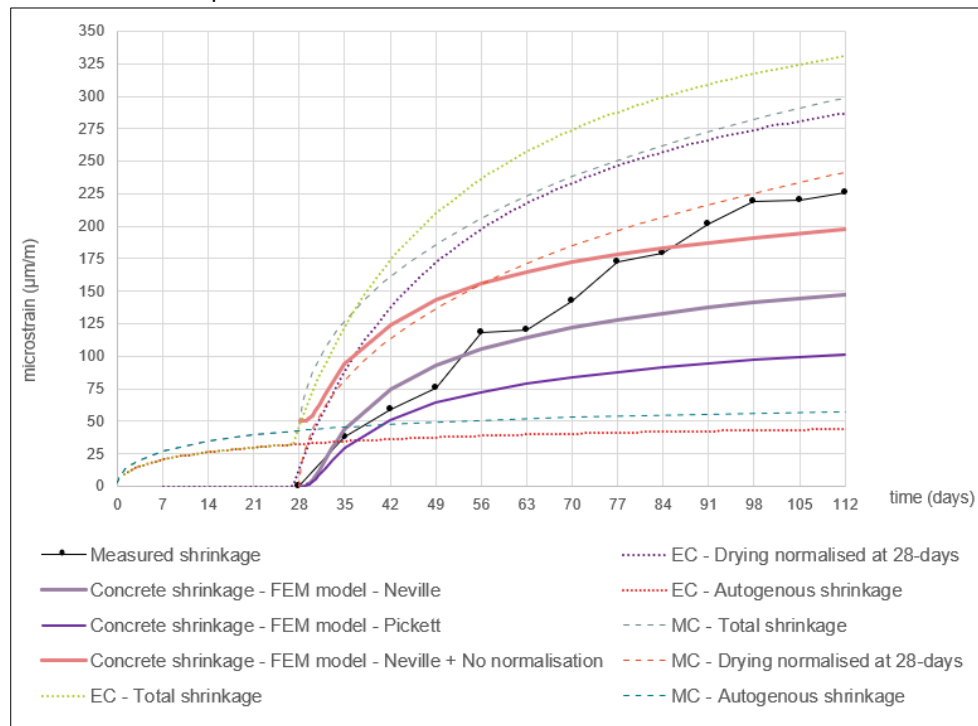


Figure 29. Concrete drying shrinkage of the developed models, the measured strain and the design codes.

The same results are also presented in Table 5.

After 84 days of drying		
	$\mu\text{m/m}$	%
Measured strain	226	100
Eurocode 2	286	127
Model Code 2010	241	107
FEM - Neville	147	65
FEM - Pickett	101	45

Table 5. Drying shrinkage at the 112th day. After 28-days of sealed hydration and 84-days of drying.

From the graph in Figure 29 and the numbers in Table 5 it can be concluded that the Model code calculation estimates drying shrinkage of the *test beam* with the best accuracy.

The models based on finite element simulation are less accurate in their outcome. This is possibly due to the estimation of restraining effects of aggregates. The simulation in FEM is focussed on cement paste behaviour.

Using the aggregate effect of Neville the simulation approximates 65% of the measured deformation. However, as explained in [3.3.2 Drying shrinkage strain](#), concrete shrinkage is only 16% of the cement paste deformation due to aggregate restraint. This step is of great significance. Improving the model used for the effects of aggregates will therefore significantly change the outcome.

At the beginning of chapter 5, the expectation was expressed that the decrease in relative pore humidity is faster when the ambient RH is lower, 50% RH instead of 65% RH. This expectation is proven to be incorrect. The effect of a change in ambient RH only affects the concrete close to the exposed surface. This is due to limited penetration depth of external RH-level, as is clearly visible in Figure 69 in [Appendix H](#), showing the RH of 100 nodes on a section-cut.

Reason that the level of ambient RH-level does not affect drying significantly in the first year, lies within the theory of Fick's second law. Diffusivity of concrete is very low and the effect of the diffusion coefficient on the change of local pore RH is higher than the present potential difference of RH-levels. Hence, the potential in RH is affecting the speed of drying. This effect is small compared to the influence of the diffusion coefficient.

To increase the speed of drying, an increase in temperature will prove to be more effective than increasing the ambient RH. As the diffusion of moisture is depending on temperature. Research should be done on the influence of temperature on the diffusion coefficient. Formula's used in this thesis are only valid by an constant temperature of 20 degrees and isothermal conditions.

The FEM results are similar to the measurements made by S. Kang et al., who used RH-probes cast into concrete. The used concrete in their research had a $w/c = 0.50$ and was dried at 20°C. One of their probes was situated at an depth of 50mm, after 80 days of drying the local RH-level reached 0.83. This is the same as what was found in the FEM-result of the RH-profile (Kang et al., 2012). This matching result is not surprising as S. Kang et al. have applied the same theory of Fick's laws of diffusion with comparable parameter values. Their suggested initial value of diffusivity is comparable to the one used in the FEM simulation of this thesis, see [2.6.1.1 Diffusion coefficient](#).

Furthermore, they used a similar finite element approach to find a numerical solution. Therefore, the comparable outcomes prove that the applied theory and the finite element model are reliable.

5 Conclusions and recommendations

5.1 Conclusions

In summary, the theoretical steps taken in this research were as follows: The changing relative pore humidity is calculated using an optimised finite element model. These values are used to determine the hydrostatic capillary pressure based on the Kelvin and Laplace equation. The material response of cement paste subjected to the capillary pressure is calculated using Bentz law. At last, the models of Pickett and Neville are used to include the restraining effect of aggregates and determine the absolute deformation of concrete subjected to drying.

The main research question is formulated as:

[How can a parametric FEM model efficiently simulate drying shrinkage in industrial concrete floors?](#)

In this study, a fundamental material model including the source mechanisms leading to macroscopic shrinkage is made. This material model is based on finite element modelling to analyse the transport of water through the porous material and based on laws of material mechanics. The result is a FEM model which simulates shrinkage. The outcome of the model is reasonable as it approaches the measured strain of the *test beam*, but not accurate. Efficiency of the model cannot be determined with the current method of verification. As the measurements used for verification were not taken with the goal of verifying the here presented model. When the development of the internal RH-levels in the cement paste are measured, together with the deformation and change in weight, than the model could be verified. With the verified model, a structural design can be made based on the calculated shrinkage which will lead to smarter designs and potential material savings. The level of efficiency should be based on material savings in the structural design, compared to a design according to the construction standards.

The theoretical calculation steps are reasoned in great detail and proven to be trustworthy. Moreover, the result are quantitatively reasonable. For the cement paste and concrete strain, the results are in the expected order of magnitude. However, only 16%~23% of paste shrinkage is present in concrete. From this, it can be deduced that the calculation of the restraining effect of the aggregates is of major importance. In this thesis, Pickett's and Neville's model are used to calculate the effect of the aggregates. Neville showed most promising results, with 23% of paste shrinkage, the concrete shrinkage is approached the best.

The change of weight during ordinary drying is simulated with an error of 8%. This means that the flux out of the system is modelled with reasonable accuracy.

Based on the presented findings, the influence of aggregates on the reduction of shrinkage should be further investigated. A slight difference in this calculation results in a significant change in the outcome. The presented model is focussed on cement paste deformations and less on the influence of aggregates. Aggregates greatly influence drying shrinkage due to their restraining effect and microcrack formation at the interfacial transition zone. In this zone at the surface of the aggregate, surface- and radial-cracks affect the local diffusivity.

The Eurocode calculations are 27% off from the measured deformations of the *test beams*. For the Model code, this is just 7%. Therefore, a better resemblance with the measurements is achieved using the Model code. Based on this finding, calculations by structural engineers on drying shrinkage of industrial concrete floors are preferably done according to the Model code.

Once the proposed method in this thesis is verified, it can be easily included in structural 3D calculations. The used 'transient heat equation', to describe diffusion of moisture through the porous concrete, has proven to be successful. However, for structural calculations, additional finites elements are required for modelling potential flow of moisture.

Shrinkage is a delicate process which is affected by tens of parameters. Several of the parameters are of a transient type. Moreover, the dependencies due to temperature and the exact chemical composition of cement cannot be neglected. In order to have the model as efficient as possible, most of the parameters used in this theses are assumed static. This proved to be successful for the study performed in this thesis. As part of the parameters are unchangeable, the outcome cannot be referred to as a fully parametric model. Therefore, parametric integration of drying shrinkage in a structural concrete floor model is yet to be achieved.

5.2 Recommendations

Based on the assumptions and outcomes of this study, multiple recommendations are given. These are meant as improvement on the current study and as recommended next step in research to improve the understanding of drying shrinkage. Before advancing to a complete parametric structural model, full understanding of the material mechanics is needed. For this, further theoretical research is needed as well as experimental studies providing reliable data.

- When the focus is solely on shrinkage, cement paste is more suitable to analyse compared to mortar or concrete. As aggregate greatly influence the strain development of the system.
Advised is to measure shrinkage of cement paste and concrete shrinkage of the same cementitious material. In this way the effect of aggregates is isolated.
- The available data used in this research was limited and should be increased. This will give more reliable data to simulate in a FE-model. Furthermore, it is advised to measure longer than 84 days, as drying shrinkage continues for years. The used strategy in this thesis can be verified in detail when internal relative humidity levels and temperature are measured during drying. During drying, the diffusivity values should also be measured.
- Additional shrinkage data from public databases could be used for verification. For example from the RILEM and JSCE (K Sakata, Tsubaki, Inoue, & Ayano, 2001) ("Zdenek P. Bazant," n.d.).
- No visual information of the concrete prisms used in this research were available. Detailed documentation of measurements and observations is advised. Cracks in the drying specimen can change the drying through diffusion significantly.
- The combination of both restrained and unrestrained shrinkage strain should be studied. By studying the differences in outcomes due to support conditions, the development of stress-dependent strains will be better understood. The difference in shrinkage of the free deformable and restrained specimen reveal information about the stress development internally. The resulting stresses should be measured during (sealed)hydration and (unsealed)drying. Furthermore, the developed stiffness of the material should be determined with a Vicat apparatus. Knowing these two physical units, results in a strain value by linear elastic law. This strain value is likely lower than the amount of strain in the specimen which is able to deform freely. This difference is due to creep and relaxation of concrete under loading.
The performed measurements and calculation should be done for a variety of cement types. For future perspective, alkali-activated cements are of interest. These materials are making headway in the quest for more sustainable concrete.
- Perform a practical study on concrete containing shrinkage reducing additives (SRA). Compare the outcome with the Kelvin-Laplace calculation strategy. The surface tension of pore water should be reduced based on the SRA concentration. In theory, the used strategy in this thesis for modelling shrinkage strain should be applicable to SRA containing concrete. As the Kelvin equations has the (reduced)surface tension as one of the input-parameters needed to link the local relative humidity to pore pressure.
- The internal restraining effect of aggregates proved to be of major importance. Effect of the interfacial transitional zone (ITZ), between aggregate and deforming paste, should be modelled in detail. Same accounts for local restraining effect of fibres in SFRC.
- The used theoretical framework is based on water transport by diffusion, as the phase of water is vapour. The actual flow of water through the porous structure can be included by Darcy's law. This does complicate the system tremendously (Gamnitzer et al., 2019).
- Once the theoretical framework is validated, it can be integrated in a structural model. In a structural model, the crack development due to drying shrinkage can be modelled. Furthermore, reinforcement stresses can be calculated and reinforcement mesh configurations can be optimized.
- The number of maximum iterations per calculate time-step in FEM can be increased to minimize the calculation error. However, for the simulation in this thesis, a higher number of iterations did not change the outcome.

6 References

- Abrihami, H. H., & Mitchell, D. (1997). Influence of Steel Fibers on Tension Stiffening. *ACI Structural Journal*, 94(6), 769–776. <https://doi.org/10.14359/9736>
- Abyaneh, S. D., Wong, H. S., & Buenfeld, N. R. (2016). Simulating the effect of microcracks on the diffusivity and permeability of concrete using a three-dimensional model. *Computational Materials Science*, 119, 130–143. <https://doi.org/10.1016/j.commatsci.2016.03.047>
- American Concrete Institute. (1971). *Cement and concrete research*. Retrieved from <http://www.sciencedirect.com/science/journal/00088846>
- Arboportaal. (n.d.). Luchtvochtigheid op het werk | Arboportaal. Retrieved April 30, 2020, from Ministerie van Sociale Zaken en Werkgelegenheid website: <https://www.arboportaal.nl/onderwerpen/luchtvochtigheid>
- Bangham, D. H., & Fakhoury, N. (1931). The translation motion of molecules in the adsorbed phase on solids. *J. Chem. Soc., CLXXV*, 1324–1333. <https://doi.org/10.1039/JR9310001324>
- Baroghel-Bouny, V., Mainguy, M., Lassabatere, T., & Coussy, O. (1999). Characterization and identification of equilibrium and transfer moisture properties for ordinary and high-performance cementitious materials. *Cement and Concrete Research*, 29(8), 1225–1238. [https://doi.org/10.1016/S0008-8846\(99\)00102-7](https://doi.org/10.1016/S0008-8846(99)00102-7)
- Battaglia, I., Whited, G., & Swank, R. (2008). *ECLIPSE® SHRINKAGE REDUCING ADMIXTURE PRODUCT EVALUATION FINAL REPORT*. Retrieved from <https://wisconsin.gov/documents2/research/fep-01-08eclipse.pdf>
- Bažant, Z.P., & Najjar, L. J. (1971). Drying of concrete as a nonlinear diffusion problem. *Cement and Concrete Research*, 1(5), 461–473. [https://doi.org/10.1016/0008-8846\(71\)90054-8](https://doi.org/10.1016/0008-8846(71)90054-8)
- Bažant, Z P, & Wittmann, F. H. (1982). *Creep and Shrinkage in Concrete Structures*. Retrieved from <https://pdfs.semanticscholar.org/39c7/e0f9da20099f4acd3193887f61f152f8a5.pdf>
- Bažant, Zdeněk P., & Oh, B. H. (1983). Crack band theory for fracture of concrete. *Matériaux et Constructions*, 16(3), 155–177. <https://doi.org/10.1007/BF02486267>
- Bentz, D.P., & Jensen, O. M. (2004). Mitigation strategies for autogenous shrinkage cracking. *Cement & Concrete Composites*, 26, 677–685. [https://doi.org/10.1016/S0958-9465\(03\)00045-3](https://doi.org/10.1016/S0958-9465(03)00045-3)
- Bentz, Dale P., Garboczi, E. J., & Quenard, D. A. (1998). Modelling drying shrinkage in reconstructed porous materials: Application to porous Vycor glass. *Modelling and Simulation in Materials Science and Engineering*, Vol. 6, pp. 211–236. <https://doi.org/10.1088/0965-0393/6/3/002>
- Bílek, V., Kalina, L., Novotný, R., Tkacz, J., Pařízek, L., & Pařízek, L. (2016). Some Issues of Shrinkage-Reducing Admixtures Application in Alkali-Activated Slag Systems. *Materials (Basel, Switzerland)*, 9(6). <https://doi.org/10.3390/ma9060462>
- Bisschop, J., & Mier, J. G. M. van. (2002). Effect of aggregates on drying shrinkage microcracking in cement-based composites. *Materials and Structures/Matériaux et Constructions*, 35, 453–461. <https://doi.org/10.1007/BF02483132>
- Breugel, K. van. (1991). *Simulation of hydration and formation of structure in hardening cement-based materials*. (Technical University Delft). Retrieved from <https://repository.tudelft.nl/islandora/object/uuid%3A2f8a3f72-1a25-4aa6-bc25-872df6fa32d4>
- Breugel, K. van, Braam, C. R., Veen, C. van der, & Walraven, J. C. (1996). Betonconstructies onder temperatuur- en krimpvervormingen : theorie en praktijk. In *Betonpraktijkreeks ; 2 TA - TT - 's-Hertogenbosch SE - IX*, 225 p. : ill. ; 30 cm. : Stichting BetonPrisma.
- Breugel, K van. (1997). Simulation of hydration and formation of structure in hardening cement-based materials. In *TA - TT - (2nd ed.)*. Delft SE - XVI, 305 p. : ill. ; 25 cm. : Delft University Press.

- Budnikov, P. P., & Strelkov, M. I. (1966). *Some Recent Concepts on Portland Cement Hydration and Hardening*. Retrieved from https://pdfs.semanticscholar.org/be8f/5ca67ee20e46e0bc6e101c047bb566e0e60d.pdf?_ga=2.245187975.300835561.1568289853-1747597664.1567172421
- Chen, D., Zhu, Q., Zong, Z., & Xiang, T. (2019). The Linear Hygroscopic Expansion Coefficient of Cement-Based Materials and Its Determination. *Materials (Basel, Switzerland)*, 13(37). <https://doi.org/10.3390>
- Concrete Society. (2014). *Technical Report 34 - Concrete industrial floors.pdf*. Concrete society.
- Crank, J. (1979). The mathematics of diffusion. In *Oxford science publications TA - TT - (2d ed.)*. Oxford [Eng] SE - viii, 414 pages : illustrations ; 24 cm.: Clarendon Press.
- CUR - Commissie Staalvezelbeton. (2012). Staalvezelbeton. kennis en kennisleemten. *CUR Bouw En Infra*, 245.
- DIANA - Finite Element Analysis. (n.d.). *Staggered Heat flow - Structural Analysis*. (10.3).
- DIANA - Finite Element Analysis. (2017). *DIANA FEA. User's Manual* (10.2; J. Manie, Ed.). Delft.
- Domone, P. L. J., & Illston, J. M. (2010). Construction materials: their nature and behaviour. In *TA - TT - (4th ed.)*. Retrieved from <https://www.worldcat.org/title/construction-materials-their-nature-and-behaviour/oclc/989126507>
- Dr. ir. E.A.B. Koenders. (2013). Hymostruc. Effective Transport Properties of Cementitious Materials. Retrieved April 23, 2020, from <https://www.nwo.nl/onderzoek-en-resultaten/onderzoeksprojecten/i/47/11947.html>
- E.I. Tazawa, R. Sato, E. Sakai, & S. Miyazawa. (2000). Work of JCI Committee on autogenous shrinkage. In Baroghel-Bouny and P.-C. Aitcin (Ed.), *International RILEM workshop on shrinkage of concrete* (pp. 21–40). Retrieved from https://www.rilem.net/publication/publication/22?id_papier=1728
- Ferraris, C. F., & Wittmann, F. H. (1987). Shrinkage mechanisms of hardened cement paste. *Cement and Concrete Research*, 17(3), 453–464. [https://doi.org/10.1016/0008-8846\(87\)90009-3](https://doi.org/10.1016/0008-8846(87)90009-3)
- Fib bulletin 65. (2012). Model code 2010 : final draft Vol. 1. In *fib bulletin, 1562-3610 ; 65 TA - TT -*. Lausanne SE - 311 blz. ; .. cm.: International Federation for Structural Concrete (fib).
- Gamnitzer, P., Brugger, A., Drexel, M., & Hofstetter, G. (2019). Modelling of coupled shrinkage and creep in multiphase formulations for hardening concrete. *Materials*, 12(11), 1–23. <https://doi.org/10.3390/ma12111745>
- Gawin, D., Pesavento, F., & Schrefler, B. A. (2006). Hygro-thermo-chemo-mechanical modelling of concrete at early ages and beyond. Part I: hydration and hygro-thermal phenomena. *International Journal for Numerical Methods in Engineering*, 67(3), 299–331. <https://doi.org/10.1002/nme.1615>
- Ghasemzadeh, F., Shekarchi, M., Sajedi, S., Khanzadeh Moradllo, M., & Sadati, S. (2010). *Effect of Silica Fume and GGBS on Shrinkage in the High Performance Concrete*. <https://doi.org/10.1201/b10552-128>
- Grassl, P., Wong, H. S., & Buenfeld, N. R. (2008). *Influence of aggregate size and volume fraction on shrinkage induced micro-cracking of concrete and mortar*. Retrieved from <https://arxiv.org/pdf/0811.0019.pdf>
- Gribniak, V., Kaklauskas, G., & Bacinskas, D. (2008). Shrinkage in reinforced concrete structures: A computational aspect. *Journal of Civil Engineering and Management*, 14(1), 49–60. <https://doi.org/10.3846/1392-3730.2008.14.49-60>
- Hajibabaei, A., Grasley, Z., & Ley, M. T. (2016). Mechanisms of dimensional instability caused by differential drying in wet cured cement paste. *Cement and Concrete Research*, 79, 151–158. <https://doi.org/10.1016/J.CEMCONRES.2015.09.007>
- Harutyunyan, V., Kirchheim, A., Monteiro, P., P. Aivazyanyan, A., & Fischer, P. (2009). Investigation of early growth of calcium hydroxide crystals in cement solution by soft X-ray transmission

- microscopy. *Journal of Materials Science*, 44, 962–969. <https://doi.org/10.1007/s10853-008-3198-5>
- Heath, A. C., & Roesler, J. R. (1999). *Shrinkage and Thermal Cracking of Fast Setting Hydraulic Cement Concrete Pavements in Palmdale, California*. Retrieved from [http://www.ucprc.ucdavis.edu/PDF/Shrinkage and Therm Crack.pdf](http://www.ucprc.ucdavis.edu/PDF/Shrinkage%20and%20Therm%20Crack.pdf)
- Holmes, N., & West, R. (2003). *Finite Element Modelling of Moisture Movement in Concrete Floors*. Retrieved from <https://arrow.dit.ie/engschcivcon>
- Holt, E. E. (2001). Early age autogenous shrinkage of concrete. *VTT Publications*, (446), 2–184.
- Idiart, A. E. (2006). Coupled analysis of degradation processes in concrete specimens at the meso-level. *Journal of Vestibular Research Equilibrium Orientation*, 20(5), 43–84. Retrieved from <http://www.ncbi.nlm.nih.gov/pubmed/20826935>
- Jennings, H. M. (2004). Colloid model of C–S–H and implications to the problem of creep and shrinkage. *Materials and Structures*, 37(1), 59–70. <https://doi.org/10.1007/BF02481627>
- Jensen, O. M. (1993). *Autogenous deformation and RH-change – self-desiccation and self-desiccation shrinkage (in Danish)*. Technical University of Denmark, Lyngby.
- Jensen, O. M., & Hansen, P. F. (1999). Influence of temperature on autogenous deformation and relative humidity change in hardening cement paste. *Cement and Concrete Research*, 29(4), 567–575. [https://doi.org/10.1016/S0008-8846\(99\)00021-6](https://doi.org/10.1016/S0008-8846(99)00021-6)
- Kamali-Bernard, S., Bernard, F., & Prince, W. (2009). Computer modelling of tritiated water diffusion test for cement based materials. *Computational Materials Science*, 45(2), 528–535. <https://doi.org/10.1016/J.COMMATSCI.2008.11.018>
- Kang, S. T., Kim, J. S., Lee, Y., Park, Y. D., & Kim, J. K. (2012). Moisture diffusivity of early age concrete considering temperature and porosity. *KSCE Journal of Civil Engineering*, 16(1), 179–188. <https://doi.org/10.1007/s12205-012-1445-4>
- KIVI. (2019). Historie KIVI | KIVI. Retrieved August 27, 2019, from <https://www.kivi.nl/meer/over-kivi/historie-kivi>
- Klee, H., Hunziker, R., van der Meer, R., & Westaway, R. (2011). Getting the numbers right: a database of energy performance and carbon dioxide emissions for the cement industry. *Greenhouse Gas Measurement and Management*, 1(2), 109–118. <https://doi.org/10.1080/20430779.2011.579357>
- Koenders, E. (2015). *The Multi-scale Model of Things* (p. 11). p. 11. Retrieved from <http://www.jci-net.or.jp/~multi-scale/Koenders.pdf>
- Koenders, E. A. B. (1997). *Simulation of Volume Changes in Hardening Cement-Based Materials*. Retrieved from <https://repository.tudelft.nl/islandora/object/uuid%3A1dbcb7fb-3f8f-466b-8517-b2235ad4912f>
- Le Chatelier, H. (1900). "Sur les changements de volume qui accompagnent le durcissement des ciments",. *Bullet. de La Société d'encouragement Pour l'industrie Nationale*, 5, 54–57.
- Lebental, B., Moujahid, W., Lee, C., Maurice, J., & Cojocar, C. S. (2012). Graphene-based resistive humidity sensor for in-situ monitoring of drying shrinkage and intrinsic permeability in concrete. *NICOM 4: 4th International Symposium on Nanotechnology in Construction*, (May).
- Liu, C., Qian, C., Qian, R., Liu, Z., Qiao, H., & Zhang, Y. (2019). Numerical prediction of effective diffusivity in hardened cement paste between aggregates using different shapes of cement powder. *Construction and Building Materials*, 223, 806–816. <https://doi.org/10.1016/J.CONBUILDMAT.2019.06.125>
- Liu, L., Wang, X., Chen, H., & Wan, C. (2016). *Microstructure-based modelling of drying shrinkage and microcracking of cement paste at high relative humidity*. <https://doi.org/10.1016/j.conbuildmat.2016.09.066>
- Liu, R., Xiao, H., Liu, J., Guo, S., & Pei, Y. (2019). Improving the microstructure of ITZ and reducing the permeability of concrete with various water/cement ratios using nano-silica.

- Journal of Materials Science*, 54(1), 444–456. <https://doi.org/10.1007/s10853-018-2872-5>
- Lu, T. (2019). *Autogenous shrinkage of early age cement paste and mortar*. <https://doi.org/10.4233/uuid>
- Lura, P. (2003). *Autogenous Deformation and Internal Curing of Concrete*.
- Lura, P., Jensen, O. M., & Breugel, K. Van. (2003). Autogenous shrinkage in high-performance cement paste : An evaluation of basic mechanisms. *Cement and Concrete Research* 2, 33, 223–232. Retrieved from https://ac.els-cdn.com/S0008884602008906/1-s2.0-S0008884602008906-main.pdf?_tid=9c61cc0a-d05d-11e7-87d7-00000aacb35d&acdnat=1511448793_2774e5b1adbc8f1a919776d1ca54c419
- Lura, P., Jensen, O. M., & Weiss, J. (2009). Cracking in cement paste induced by autogenous shrinkage. *Materials and Structures*, 42(8), 1089–1099. <https://doi.org/10.1617/s11527-008-9445-z>
- Mackenzie, J. K. (1950). The Elastic Constants of a Solid containing Spherical Holes. *Proceedings of the Physical Society. Section B*, 63(1), 2–11. <https://doi.org/10.1088/0370-1301/63/1/302>
- Mier, J. G. M. van. (2013). *Concrete fracture : a multiscale approach*. CRC Press.
- Müller, H. S., & Acosta, F. (2015). *Eurocode 2, revision 2015+ "Status of Work on TG7 on the modelling of shrinkage."* Report.
- Narin, F., & Wiklund, O. (2012). Design of slabs-on-ground regarding shrinkage cracking. *Thesis - Chalmers University of Technology*.
- NEN. (2011). *NEN-EN 1992-1-1 + C2*. (november 2011).
- Neville, A. M., & Brooks, J. J. (1991). Concrete technology. In *Building Research & Information* (2nd ed., Vol. 19). <https://doi.org/10.1080/09613219108727128>
- Nielsen, L. F. (1991). *A research note on sorption, pore size distribution, and shrinkage of porous materials*. Lyngby, Denmark.
- Nijs, K. (2017). Finite element implementation of the Ishikawa concrete drying shrinkage model Author. *Thesis - Delft University of Technology*, 41.
- Park, S. S., Kwon, S. J., & Song, H. W. (2011). Analysis technique for restrained shrinkage of concrete containing chlorides. *Materials and Structures/Materiaux et Constructions*, 44(2), 475–486. <https://doi.org/10.1617/s11527-010-9642-4>
- Persson, B. (1997). Self-desiccation and its importance in concrete technology. *Materials and Structures*, 30(5), 293–305. <https://doi.org/10.1007/bf02486354>
- Pichler, C., Lackner, R., & Mang, H. A. (2007). A multiscale micromechanics model for the autogenous-shrinkage deformation of early-age cement-based materials. *Engineering Fracture Mechanics*, 74(1–2), 34–58. <https://doi.org/10.1016/j.engfracmech.2006.01.034>
- Pickett, G. (1956). Effect of Aggregate on Shrinkage of Concrete and a Hypothesis Concerning Shrinkage. *ACI Journal Proceedings*, 52(1), 581–590. <https://doi.org/10.14359/11617>
- Pleysier, I. J. A. (n.d.). Vocht, Luchtstroming door constructies en infiltratie. In *Post-HBO Bouwfysica* (pp. 1–16). Bouwfysica en Energie, Deerns.
- Powers, T. C., & Brownyard, T. L. (1947). Studies of the Physical Properties of Hardened Portland Cement Paste. *ACI Journal Proceedings*, 43(9), 933–992. <https://doi.org/10.14359/15306>
- Powers, Treval Clifford. (1948). *A discussion of cement hydration in relation to the curing of concrete*. Chicago: [Portland Cement Association].
- R.M. Mors. (2011). Autogenous Shrinkage Cementitious materials containing BFS. *Master Thesis ,Delft University of Technology*, (August).
- RCR Industrial Flooring. (2019). Bekaert - Dramix. Retrieved from Bekaert - Dramix website: <https://www.rcrindustrialflooring.com/strategic-partnerships>

- Reybrouck, N., Wendner, R., Caspeepele, R., & Taerwe, L. (2009). *Shape Correction Factors for Drying Shrinkage of Several Typical Concrete Cross-Sections*. (February 2018).
- RILEM TC 162-TDF. (2003). Final recommendation of RILEM TC 162-TDF: Test and design methods for steel fibre reinforced concrete sigma-epsilon-design method. *Materials and Structures*, 36(262), 560–567.
- Rots, J. G. (1988). *Computational modeling of concrete fracture* (TU Delft). Retrieved from <https://repository.tudelft.nl/islandora/object/uuid%3A06985d0d-1230-4a08-924a-2553a171f08f>
- Sakata, K, Tsubaki, T., Inoue, S., & Ayano, T. (2001). *PREDICTION EQUATIONS FOR CREEP AND DRYING SHRINKAGE IN CONCRETE OF WIDE-RANGING STRENGTH*. Retrieved from <http://library.jsce.or.jp/jsce/open/00670/No40/CLI-40-0145.pdf>
- Sakata, Kenji, & Shimomura, T. (2004). Recent progress in research on and code evaluation of concrete creep and shrinkage in Japan. *Journal of Advanced Concrete Technology*, 2(2), 133–140. <https://doi.org/10.3151/jact.2.133>
- Setzer, M. J. (2006). The solid-liquid gel-system of hardened cement paste. *2nd International RILEM Symposium on Advances in Concrete through Science and Engineering*. <https://doi.org/10.1617/2351580028.044>
- Soroka, I. (1979). Portland cement paste and concrete. In *TA - TT -*. London: Macmillan.
- Strang, G., & Herman, E. (2018). *Calculus. Volume 3*. Retrieved from <https://www.bartleby.com/textbooks/calculus-volume-3-16th-edition/9781938168079/solutions>
- Tazawa, E., Miyazawa, S., & Kasai, T. (1995). Chemical shrinkage and autogenous shrinkage of hydrating cement paste. *Cement and Concrete Research*, 25(2), 288–292. [https://doi.org/10.1016/0008-8846\(95\)00011-9](https://doi.org/10.1016/0008-8846(95)00011-9)
- The Concrete Centre. (2016). Eurocodes revision – an update. *MPA - The Concrete Centre - UK*, (April), 53–54. Retrieved from [https://www.thisisconcrete.co.uk/TCC/media/TCCMediaLibrary/PDF attachments/CONCRETE-Jan-2016.pdf](https://www.thisisconcrete.co.uk/TCC/media/TCCMediaLibrary/PDF%20attachments/CONCRETE-Jan-2016.pdf)
- Thelandersson, S., Martensson, A., & Dahlblom, O. (1988). Tension softening and cracking in drying concrete. *Materials and Structures/Materiaux et Constructions*, 21, 416/424. Retrieved from <https://link.springer.com/content/pdf/10.1007%2FBF02472321.pdf>
- Tiberti, G., Minelli, F., & Plizzari, G. (2015). Cracking behavior in reinforced concrete members with steel fibers: A comprehensive experimental study. *Cement and Concrete Research*, 68, 24–34. <https://doi.org/10.1016/j.cemconres.2014.10.011>
- Tiberti, G., Mudadu, A., Barragan, B., & Plizzari, G. (2018). Shrinkage cracking of concrete slabs-on-grade: A numerical parametric study. *Fibers*, 6(3), 1–18. <https://doi.org/10.3390/fib6030064>
- Traetteberg, A., Ramachandran, V. S., & Grattan-Bellew, P. E. (1974). A study of the microstructure and hydration characteristics of tricalcium silicate in the presence of calcium chloride. *Cement and Concrete Research*, 4(2), 203–221. [https://doi.org/10.1016/0008-8846\(74\)90133-1](https://doi.org/10.1016/0008-8846(74)90133-1)
- UNEP; WMO. (2014). IPCC AR5 Climate Change 2014. *IPCC*, 1535. <https://doi.org/10.1017/CBO9781107415324>
- Van Breugel, Klaas, & Van Tuan, N. (2015). Autogenous shrinkage of HPC and ways to mitigate it. *Key Engineering Materials*, 629–630(December 2015), 3–20. <https://doi.org/10.4028/www.scientific.net/KEM.629-630.3>
- Van den Akker, H., & Mudde, R. F. (2014). *Transport Phenomena - The Art of Balancing*.
- Vass, T., Fernandez-Pales, A., & Levi, P. (2019). Cement Tracking Clean Energy Progress. Retrieved August 26, 2019, from International Energy Agency website: <https://www.iea.org/tcep/industry/cement/>

- Vazquez, A., & Pique, T. M. (2016). Biotech admixtures for enhancing portland cement hydration. *Biopolymers and Biotech Admixtures for Eco-Efficient Construction Materials*, 81–98. <https://doi.org/10.1016/B978-0-08-100214-8.00005-1>
- Vecchio, F. J., & Collins, M. P. (1986). Modified Compression-Field Theory for Reinforced Concrete Elements Subjected To Shear. *Journal of the American Concrete Institute*, 83(2), 219–231. <https://doi.org/10.14359/10416>
- Vervoort, N. H. A. (2015). Verhinderde krimp in op staal gefundeerde, betonnen bedrijfsvloeren. *Master Thesis, Eindhoven University of Technology*.
- Weiss, W. J. (1999). *Prediction of early-age shrinkage cracking in concrete elements*. Retrieved from <https://ui.adsabs.harvard.edu/abs/1999PhDT.....219W/abstract>
- Wimsatt, A. J., McCullough, B. F., & Burns, N. H. (1987). *Methods of Analyzing and Factors Influencing Frictional Effects of Subbases*. Retrieved from <https://library.ctr.utexas.edu/digitized/texasarchive/phase2/459-2f.pdf>
- Wittmann, F. (1968). Surface Tension. Shrinkage. and Strength of Hardened Cement Paste. *Matériaux et Constructions*, 1, 547–552.
- Wu, L., Farzadnia, N., Shi, C., Zhang, Z., & Wang, H. (2017). Autogenous shrinkage of high performance concrete: A review. *Construction and Building Materials*, 149(September), 62–75. <https://doi.org/10.1016/j.conbuildmat.2017.05.064>
- Wu, Z., Mac, M. J., Wong, H. S., & Buenfeld, N. R. (2013). *CHARACTERISATION OF MICROCRACKS AND THEIR INFLUENCE ON TRANSPORT PROPERTIES OF CEMENTITIOUS MATERIALS*. Retrieved from https://www.nanocem.org/uploads/documents/Project_11.pdf
- Xi, Y., Bažant, Z. P., Molina, L., & Jennings, H. M. (1994). Moisture diffusion in cementitious materials Moisture capacity and diffusivity. *Advanced Cement Based Materials*, 1(6), 258–266. [https://doi.org/10.1016/1065-7355\(94\)90034-5](https://doi.org/10.1016/1065-7355(94)90034-5)
- Ye, G. (2003). *Experimental Study and Numerical Simulation of the Development of the Microstructure and Permeability of Cementitious Materials* (Vol. 50). <https://doi.org/10.1617/s11527-017-1082-y>
- Yoo, D. Y., Kim, S., & Kim, M. J. (2018). Comparative shrinkage behavior of ultra-high-performance fiber-reinforced concrete under ambient and heat curing conditions. *Construction and Building Materials*. <https://doi.org/10.1016/j.conbuildmat.2017.12.029>
- Yu, J., & Zhao, Q. (2013). Effect of steel fiber on creep behavior of concrete. *Kuei Suan Jen Hsueh Pao/Journal of the Chinese Ceramic Society*, 41(8), 1087–1093.
- Zdenek P. Bazant. (n.d.). Retrieved May 16, 2020, from <http://www.civil.northwestern.edu/people/bazant/>
- Zhang, J., Hou, D., & Han, Y. (2012). Micromechanical modeling on autogenous and drying shrinkages of concrete. *Construction and Building Materials*, 29, 230–240. <https://doi.org/10.1016/J.CONBUILDMAT.2011.09.022>
- Zhou, J., Ye, G., & Breugel, K. van. (2006). Hydration of Portland cement blended with blast furnace slag at early stage. *2nd International RILEM Symposium on Advances in Concrete through Science and Engineering*, (January 2006). <https://doi.org/10.1617/2351580028.085>

7 Appendix

Appendix I: Response of materials

This chapter explains the hardening process of cement. Shrinkage deformation is caused by the hydration of cement and drying of the material. The amount of shrinkage is affected by several parameters as the cement type and the water content in the mixture. In this chapter, the material properties of concrete and its influence on shrinkage is explained.

I.1 Cement

Cement is the binder in concrete which hardens in reaction with water. The product of cement and water is called: cement paste. Mixing cement paste with sand and aggregates results in concrete. Sand contains particles smaller than 2 mm in size. Aggregates are a mixture of different sized grind. Natural stone or crushed natural stone is used as Grind. The aggregates used are characterised by their size distribution. This can be 2 to 20 mm or 2 to 40 mm. The composition of concrete is schematized in Figure 30.

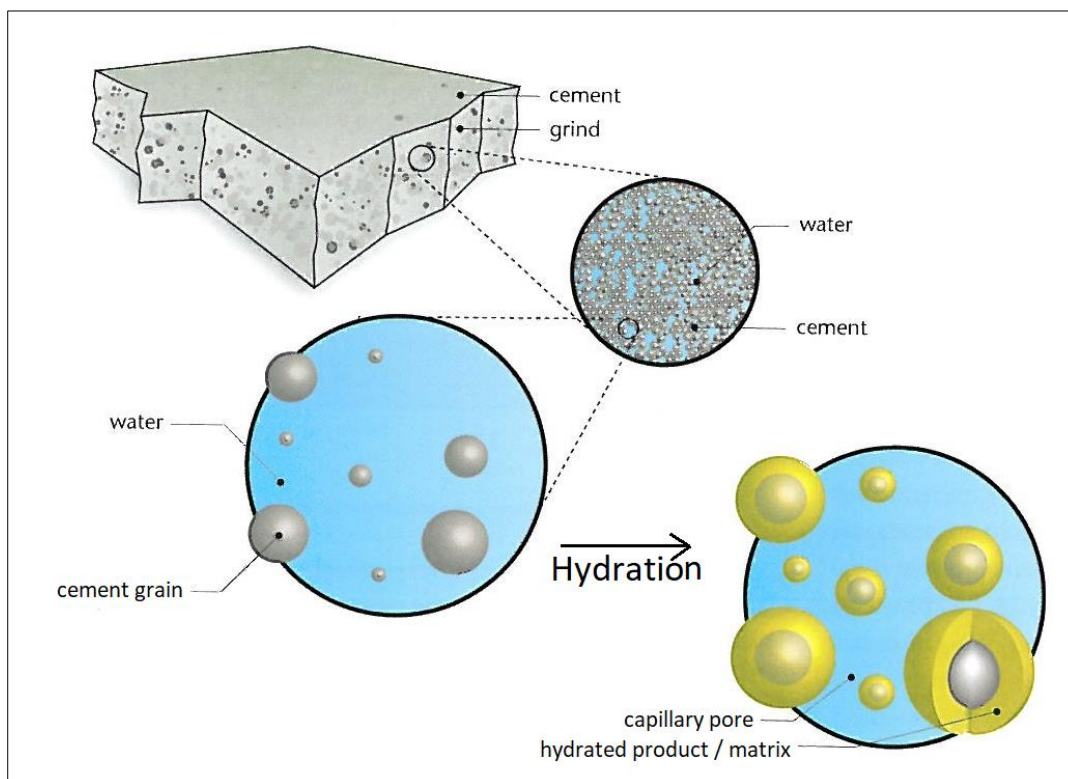


Figure 30. Hydrated cement particles in concrete. (source: betonlexicon.nl)

Most of the cement used throughout the world is Portland Cement, patented in 1824 by Joseph Aspdin (Domone & Illston, 2010). Focus in this research is on Portland cement (CEM I). Second most used cement is a blend of Portland cement clinker and blast furnace slag (CEM III). It differs per application which type of cement is preferred and per location, slab availability differs per country. The stiffness and even more the strength of hardened concrete highly depends of the cement type and amount of cement used.

This chapter is a literature review on concrete and shrinkage behaviour. The hardening of cement by hydration is explained and how this results in shrinkage.

1.1.1 Cement composition and reaction

Cement is the component in concrete which binds the aggregates to form a monolithic stiff solid. The binding reaction starts when water is added to the cement powder. Portland cement has hydraulic properties, it reacts with water. This is different for blast furnace slag cement which is a latent hydraulic material and needs an activator to react and start the hardening process (Domone & Illston, 2010).

This hydraulic reaction is responsible for a change of the chemical structure. Volume changes that are related to the hydration reaction can for a part be designated as autogenous shrinkage. This will be elaborated in chapter [1.2.2 Autogenous shrinkage](#).

Portland cement is manufactured by heating a mixture of ingredients up to 1500°C in a rotating kiln. The material mixture entering the kiln is called the raw meal. Essential components in cement are calcium silicates, needed for the accretion of a strong and stiff material. These components are found in the raw meal entering the kiln. Existing of calcium oxide (CaO) and silicon dioxide, also known as silica (SiO₂). Both of these needed elements are found in natural occurring resources. The former, CaO, is sourced in the form of calcium carbonate (CaCO₃). Found in limestone or chalk. The other essential component, SiO₂, is sourced in the form of (quartz)sand, clay or shale.

To ensure a continuous uniform product, the stages in the kiln need to be well monitored. Cement manufacturing is highly energy consuming (IEA)(Vass, Fernandez-Pales, & Levi, 2019). A statement about the environmental impact of cement production is given in [Appendix B](#).

Portland cement consist of a mixture of compounds formed in the kiln at different temperatures, so called *burning zones*. The rotating kiln process is called clinkering, producing clinker. This clinker is cooled and grinded to form usable cement grains.

In the theory of cementitious materials, certain abbreviations for oxides are used:

CaO	(lime)	= C
SiO ₂	(silica)	= S
Al ₂ O ₃	(alumina)	= A
Fe ₂ O ₃	(iron oxide)	= F
H ₂ O	(water)	= H

The four main compounds, often referred to as phases in cement are:

Chemical name	consistence	In short	
Tricalcium silicate	3CaO.SiO ₂	C3S	Alite
Dicalcium silicate	2Cao.SiO ₂	C2S	Belite
Tricalcium aluminate	3Cao.Al ₂ O ₃	C3A	
Tetracalcium aluminoferrite	4Cao.Al ₂ O ₃ .Fe ₂ O ₃	C4AF	

Table 6. Cement nomenclature (Domone & Illston, 2010)(L. Wu et al., 2017).

Principal oxides in the raw meal are calcium oxide and silica dioxide. These are present in a 3:1 weight ratio and are needed to form the two calcium silicates, being C3S and C2S. These two compounds make up 75% of the cement mass. Small quantities of additional materials are added to achieve the right properties for Portland cement. Being gypsum (calcium sulphate dihydrate, CaSO₄.2H₂O), calcium sulphate (anhydrite) and limestone powder (free lime, CaO). These additives are needed to acquire the right speed of hydration to regulate the setting time. The gypsum and dehydrated gypsum, anhydrite, decrease the speed of hardening. Without these elements there is the risk of a *flash set*. An unwanted event of rapid hardening, decreasing the ability to fully hydrate.

In the cement type CEM III, part of the Portland cement clinker is replaced with blast furnace slag or ground granulated blast furnace slag (GGBFS). This is a pozzolanic material type. A small concentration of Portland is needed for initial hardening. The hydration model for this type of cement is more complex as a result of the hydration reactions happening simultaneously. In this report the theory of Portland cement hydration is used to clarify shrinkage development.

Hydration reactions of compounds in cement is explained in the next part [I.1.2 Hydration](#).

Followed by an explanation of the relation between this chemical reaction and shrinkage.

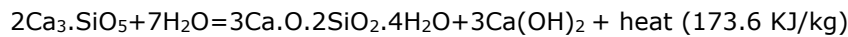
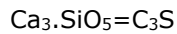
I.1.2 Hydration

Hardened cement is scientifically seen as solid gel. This product is a result of the reaction between cement and water, called a solid-liquid gel system (Setzer, 2006).

From the unhydrated cement, the two calcium silicates compounds give most of the stiffness and strength to the hydrated and hardened product (Domone & Illston, 2010).

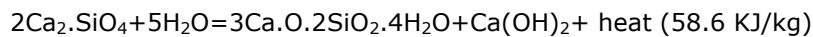
The alite, C3S, is the most reactive hydrant forming Calcium-Silicate-Hydrate (CSH).

This exothermic reaction is:



The main product is Calcium-Silicate-Hydrate (CSH). However, the alite also produces Calcium Hydroxide (CH). This hydroxide is deposited as a crystal and has the chemical formula $\text{Ca}(\text{OH})_2$, known as CH-crystals or portlandite (Harutyunyan, Kirchheim, Monteiro, P. Aivazyanyan, & Fischer, 2009)(L. Wu et al., 2017).

Hydration of belite, C2S, produces similar products as alite but in slower manner:



Typically for the hardening of Portland cement is a dominance of CSH hydrant product from day 1 and onwards. The formed CSH is categorised as an amorphous solid.

In brief, the hydration process of cement can be divided into five consecutive stages. These stages are recognizable by the amount of heat output, or rate of heat evolution, of the mixture. This heat is produced by the exothermic reaction of cement. The duration and amount of heat that is produced during a stage, depends on the type of cement in combination with certain additives (K van Breugel, 1997). Rate of heat evolution is divided into stages as illustrated in Figure 31.

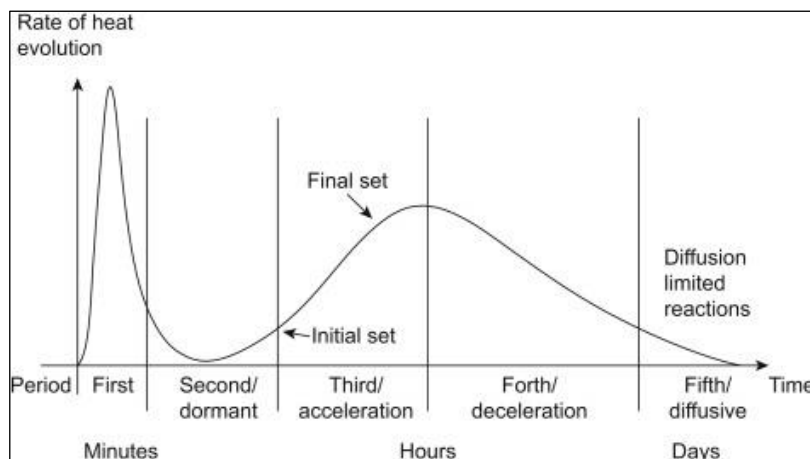


Figure 31. Heat evolution of hydrating cement paste (Vazquez & Pique, 2016)

The first stage starts when water is added to the cement mixture. This stage will last for about 15 minutes and shows a distinctive first initial peak of heat output. This can be clearly seen in Figure 31. In this phase no hardening takes place yet but two chemical reactions occur. At first gypsum is reformed. This happens by the rehydration of the dehydrated gypsum, calcium sulphate hemihydrate, when contact is made with water. Secondly, ettringite is formed by a reaction between gypsum, C3A and water. Without the presence of gypsum, C3A, the main aluminate phase, would react violently with water. Ettringite forms a protective layer on the tricalcium aluminate (C3A). By doing so it prevents further *fast/flash* reaction which would lead into an unwanted event of a *flash set*, turning the mixture quickly into a stiff paste.

The ettringite is not of value to the final developed strength in concrete, but has the highest relative contribution to chemical shrinkage (Holt, 2001). This will be elaborated in [1.2.2 Autogenous shrinkage](#).

The second stage has a duration of about 2 hours, known as the dormant period. Together with the first stage they form the liquid phase. The aluminates C3A and C4AF continue to react. However, the ferrite including aluminate reacts slightly slower than C3A (Domone & Illston, 2010). During this stage the deposition of portlandite, CH, in crystalline form takes place. Together with the very first hydrated products, they form a barrier layer on hydrated cement elements. The stages of a cement-grain during hydration are illustrated in Figure 32.

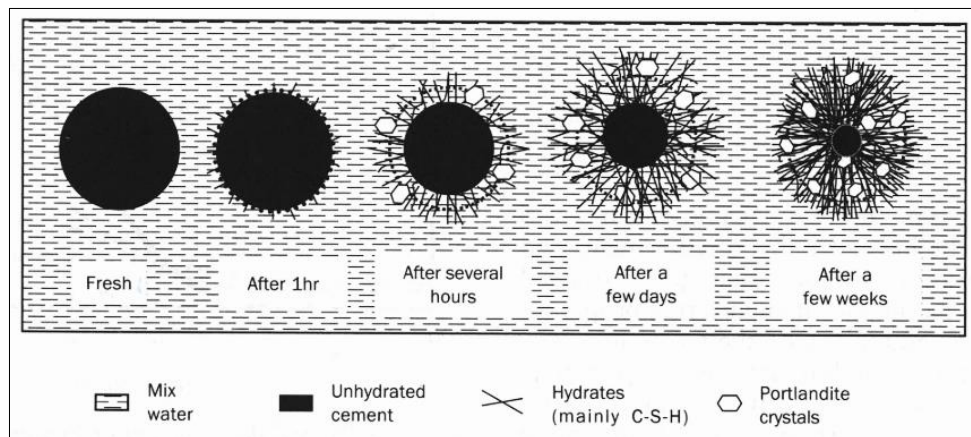


Figure 32. Stages of hydration of a single cement grain (Domone & Illston, 2010)

The barrier layer is formed at the surface of the cement grains, the interface layer. During the slow dissolution of C3S in the initial hydration phase, Ca^{2+} and OH^- ions are released. Ca^{2+} ions are bound to the C3S surface and make it positively charged while the OH^- ions stay in the gel. This clarifies the formation of Portlandite crystals, $\text{Ca}(\text{OH})_2$, in the scheme of Figure 32. In Figure 31 a growing heat output towards the end of the dormant period is seen caused by the formation of Portlandite (CH).

The third stage is characterised by the accelerated chemical reaction by hydration of C3S and C2S. These principal compounds react to form calcium silicate hydrates (CSH). Furthermore, an increase of calcium hydroxide is apparent, making the hardening cement highly alkaline. pH Values are between 12.5 and 13. The formed CSH are deposited as irregular fibrous particles which are shaped flat, hollow or solid. They are typically 0.5-2 μm long and less than 0.2 μm in diameter. The formation of these fibrous element increase the surface area by a thousand time (Domone & Illston, 2010).

This increases the exposure of the unhydrated parts of the cement grain and explains the fast acceleration in hydration as seen in the heat output.

The products of hydration form the gel. This gel contains pores. Further on in hydration these pores get filled by new deposited CSH and portlandite crystals. The porosity decreases as hydration continues. The amount and size of pores in low water/cement ratio concrete is lower compared to that of higher water/cement ratio.

The density of the original water filled area is slightly lower than close to the unhydrated cement. Here there is a denser matrix of deposited hydrated products, called the inner product. The so called outer product contains more CH-crystals and aluminoferrite and has a lower presence of CSH fibrous material. Interlocking CSH particles in the outer product form connections between cement elements. Resulting in a solid skeleton structure.

The third stage is followed by a stage of 'deceleration'. The rate of hydration reduces due to decrease of pores and ease of water to flow through the gel of hydrated products.

Followed the fifth diffusive stage of slow continuation of hydration. The on-going hydration is a process continuing for years. Concrete strength is still increasing during this period.

1.2 Shrinkage

Shrinkage is a change in volume caused by the chemical and physical properties of concrete. Volume changes of concrete are also induced by creep, relaxation and thermal expansion. When referred to free shrinkage, a structural member can deform without any physical restrictions or limitations. Stresses inside the concrete member arise when free shrinkage is restrained. The external interaction with the soil and internal interaction with reinforcement form restraints. In the case, reduction in volume of the concrete member is restrained and tensile stresses will develop, these may result in cracking when the tensile strength of the concrete member is exceeded.

The total shrinkage of a structural concrete element is determined by multiple design- and material-parameter. There are based on the material properties, dimension of the element, external influences and heavily time dependent.

Different types of concrete shrinkage are distinguished from each other. The total shrinkage is the sum of drying-, autogenous-, chemical-, plastic-, and carbonation-shrinkage (K. van Breugel, Braam, Veen, & Walraven, 1996). Shrinkage types are shown in Figure 33.

In [Appendix A](#), an explanatory diagram is given. In that diagram internal stresses, caused by restrained (drying) shrinkage, are linked to the formation of cracks.

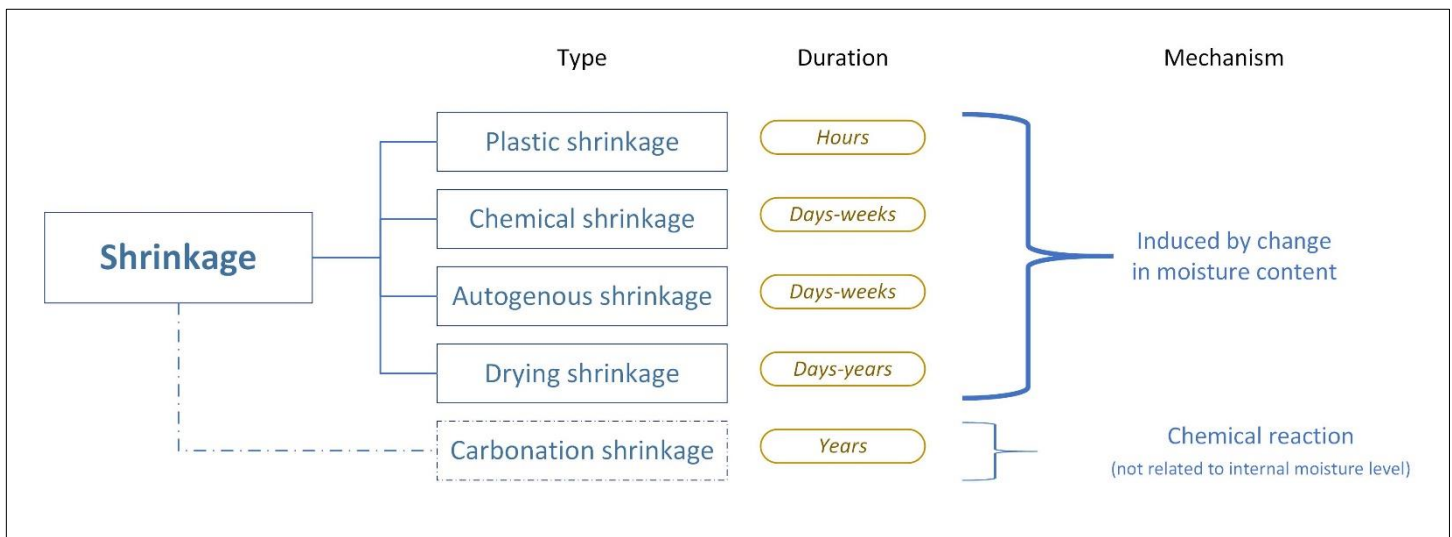


Figure 33. Types of shrinkage.

Plastic, chemical and autogenous shrinkage are related to processes in the hydration stage. During this process water is consumed and the moisture content changes. Drying shrinkage is a long-term process not related to hydration but to an exchange of moisture with the environment. Chemical and autogenous shrinkage are related to each other and hard to distinguish. The types of shrinkage will be explained in the next chapters.

Carbonation shrinkage is caused by a reaction of atmospheric carbon dioxide (CO_2) with hydrated cement. The relatively large calcium hydroxide crystals (CH, portlandite) dissolve, producing a volumetric change (D.P. Bentz & Jensen, 2004). The resulting strain over time is not significant compared to drying shrinkage. The principal effect of carbonation is a decrease in pH, leading to an increasing of corrosion of the reinforcement (Holt, 2001). This form of shrinkage is not in the scope of this thesis.

For low- and normal-strength concrete, drying shrinkage is the main contributor to the total shrinkage. As the strength of concrete increases, the water-to-cement ratio (w/c-ratio) decreases. Autogenous and chemical shrinkage become more relevant for high strength concrete. Difference in shrinkage caused by the concrete strength is illustrated in Figure 34. High strength concrete has a lower w/c-ratio than normal strength concrete, meaning less water content. Therefore, less water is subjected to drying. In addition, low water presence in the hydrating paste evokes self-desiccation which is the main mechanism behind autogenous shrinkage.

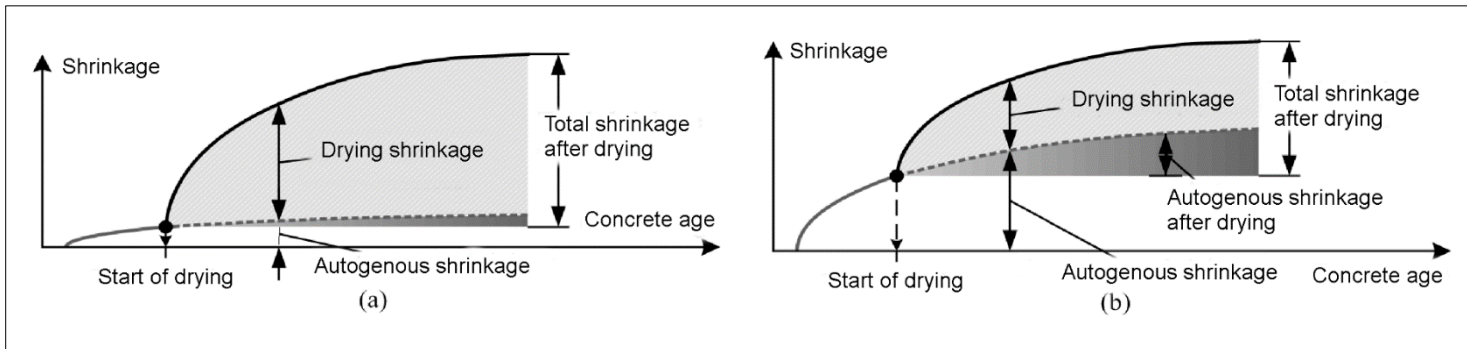


Figure 34. Shrinkage types developing over time. Low-medium strength concrete (a) and high strength concrete (b) (Kenji Sakata & Shimomura, 2004).

1.2.1 Plastic shrinkage

Plastic shrinkage occurs in the early stage of hardening, just after pouring. At this moment, water evaporates from the surface. Due to capillary forces, water is being forced from deeper in the slab towards the surface. In case of excessive water quantities in the mixture, this effect might result in bleeding. When bleeding occurs, more water is at the surface than can evaporate. On the other hand, when more water evaporates from the outer surface than is provided from the inner layers, a net water loss is present resulting in a volumetric reduction. Young concrete has low tensile strength capacity. The resulting tensile forces in the outer layer of the concrete slab might result in a dense mesh of fine and shallow cracks, called crazing. An illustration of this phenomena is shown in Figure 35. Based on the physical effects, a clear distinction from drying shrinkage can be made. Firstly, crazing is occurring in the first hours after pouring until the end of the first day. This is different compared to drying shrinkage which is a long-term effect and continues for years. Secondly, plastic shrinkage is only present close to the surface and has limited cracks widths. Therefore, the resulting the damage caused is only esthetically. A difference is seen in drying shrinkage which can cause structural damage. Drying shrinkage results in cracks piercing through the whole cross-section

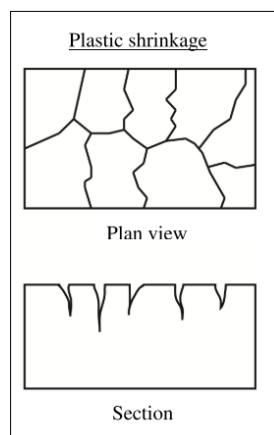


Figure 35. Illustration of plastic shrinkage (Domone & Illston, 2010).

1.2.2 Autogenous shrinkage

The chemical shrinkage as result of the hydration process in the cement paste, as described in part [1.1.2 Hydration](#), is a part of autogenous shrinkage. The total amount of chemical shrinkage can theoretically be determined by stoichiometric calculations on the cement hydration equations, published by Tazawa et al. (Tazawa, Miyazawa, & Kasai, 1995). The volume of the final hydrated product is less than of the initial cement products. There does not exist an easy one-to-one relation between chemical shrinkage and macroscopic autogenous shrinkage of concrete or cement paste. The reason for this is that most of the chemical shrinkage on microscopic level results in small internal air voids. These voids do not affect external deformation to the specimen. This is illustrated in Figure 36.

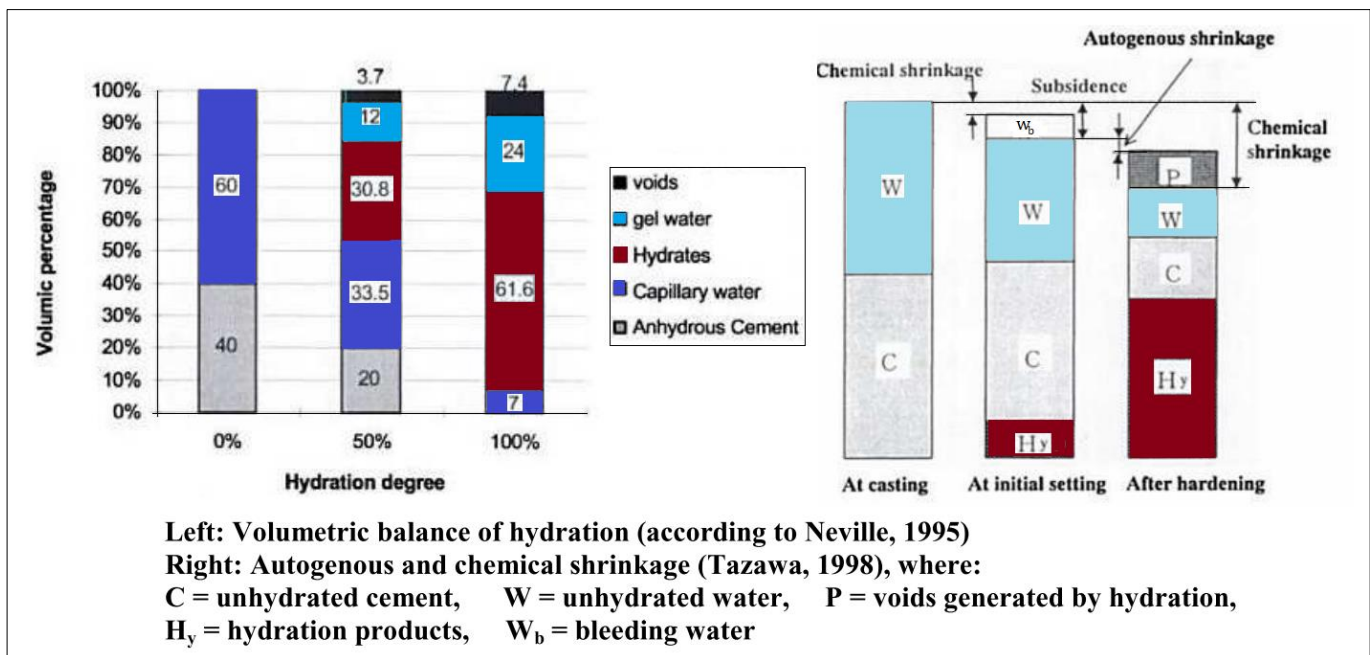


Figure 36. Autogenous shrinkage caused by hydration of cement.

The relation between chemical shrinkage and macroscopic autogenous shrinkage is further reduced by other phenomena, for example, the formation of ettringite in the cement paste (Jensen & Hansen, 1999)(Holt, 2001). Swelling of hardening concrete is explained later in this thesis.

Autogenous deformation is a viscoelastic response to the concrete self-desiccation (Persson, 1997). Self-desiccation is a result of internal drying, it occurs when complete saturation of particles is no longer sustained, resulting in a reduction of the internal relative humidity (RH) and a decrease in the meniscus radius. In chapter [2 Theory of drying](#) is explained how pore RH is related to internal strain and shrinkage.

It is needed to position the effect of autogenous shrinkage in perspective regarding to the scope of this research on concrete industrial floor slabs. These type of floors are in general constructed using low-, to medium-strength concrete as C30/37 (Adviesgroep Civiele Techniek, ABT, 2015)

The self-created bulk strain by autogenous type of shrinkage is several times less than for drying shrinkage. This is valid for low-, to medium-strength concrete. However, in high-strength concrete autogenous shrinkage becomes the prominent source of strain. High strength concrete has low porosity and low water to cement ratio (Persson, 1997) (Lura et al., 2009)(Jensen & Hansen, 1999). The reason that these cement pastes show more self-desiccation is because of an insufficient amount of water for full hydration. Secondly, the relative high cement content will cause a high amount of chemical shrinkage.

Studies showed a relation between autogenous deformation and a change in relative humidity (RH) (Jensen & Hansen, 1999). The rate of deformation as well as the final autogenous deformation, after setting, depend on the temperature. At higher temperatures the decrease of internal RH is progressing at a higher rate.

Shrinkage is temperature dependent, as explained in part [2.3 Method of Kelvin – Laplace](#). Temperature is an important parameter in calculating the pore pressure related to the relative humidity in the pore. In this research thesis temperature is kept constant at 20 °C (Celsius) or 293.15 K (Kelvin).

1.2.3 Drying shrinkage

Drying shrinkage is a strain deformation caused by moisture transport. An excessive amount of water is present in concrete to ensure workability. This water will evaporate from the poured concrete. Due to continues hardening, the porosity of concrete decreases over time as well as the speed of drying. This process can continue for years and so does drying of the concrete. As is stated in the 'Technical Report 34' by the Concrete Society, drying shrinkage is the most relevant type of shrinkage for industrial floors (Concrete Society, 2014).

In the type of concrete used for industrial floors, drying shrinkage is more prominent over autogenous shrinkage. This is opposite for high-strength concrete as explained earlier. In Figure 37 the free shrinkage deformation for C35/45 is shown. In this graph, it can be clearly seen that most of the deformation is a result of drying according to this graph (Tiberti, Mudadu, Barragan, & Plizzari, 2018).

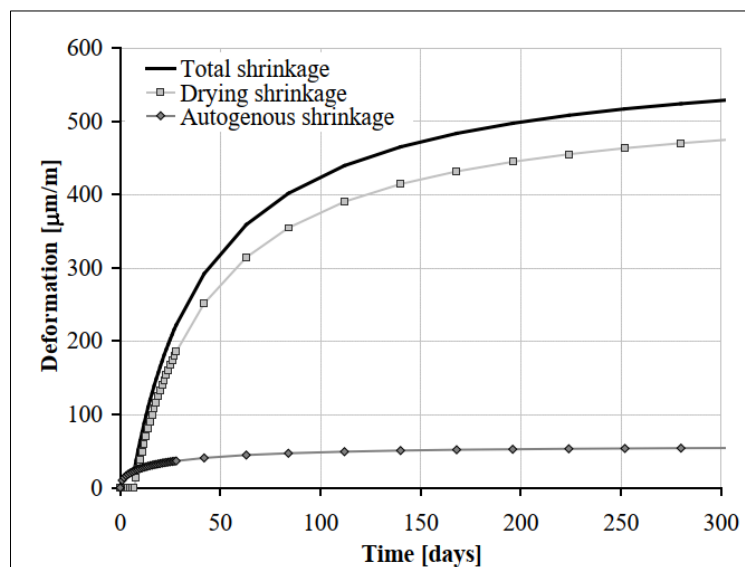


Figure 37. Shrinkage according the Eurocode for C35/45. (Tiberti, Minelli, & Plizzari, 2015)

Shrinkage deformation is subdivided in an axial uniform deformation and a shrinkage gradient. Autogenous deformation takes place uniformly throughout the cross section. Drying shrinkage is predominantly taking place at the exposed surface and to a lesser extent at the bottom side. For industrial slab floors this depends on the relative humidity of the base ground compared to the relative humidity of the surface exposed to the air. The scientists Heath & Roesler have shown that the difference between exposed and not exposed surface of final drying shrinkage is 60% on average, see Figure 38 (Heath & Roesler, 1999). The gradient part of drying shrinkage is reducing over time as the speed of drying slows down.

Other models also exist. In 1998 Rasmussen & McCullough assumed no shrinkage from the bottom till mid-depth of the slab and a linear development from mid-depth till full shrinkage development at the exposed top surface.

The overall speed of drying shrinkage reduces as the concrete member dries out. When the difference of relative humidity (or any other type of concentration) between point A and B becomes smaller, the speed of diffusion becomes smaller as well. This relation is of importance when modelling drying later in this thesis. It is covered in part [2.6 Diffusion](#).

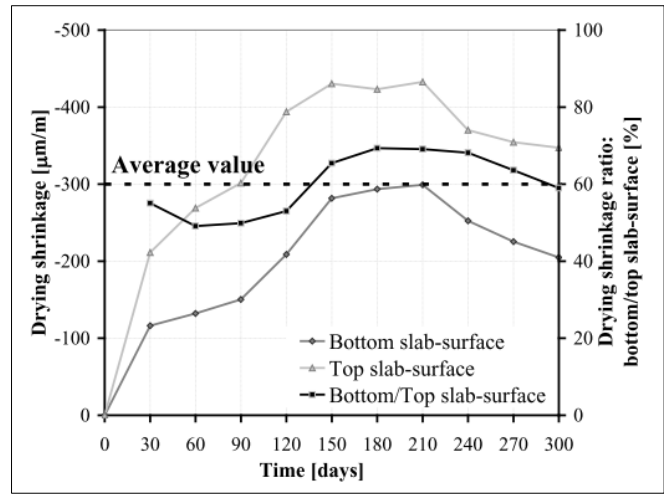


Figure 38. distribution of drying shrinkage over the cross section of a 200mm thick concrete slab. (Heath & Roesler, 1999)

The humidity of the environment acts as drying force in moisture transport. For this reason at the top side of the slab is more drying shrinkage. The cracks will appear at the place where they are least wished for serviceability of the structure. Secondly, due to the reduction in length of the top side a curling effect will take place at the corners (see Figure 39). The corners and sides have the tendency to move upwards and reduce the flatness of the floor. It happens that a crack appears diagonal to the corner after it is loaded again (Figure 40). Curling can be prevented by reducing the difference in top-, and bottom-shrinkage or by applying specific reinforcement.

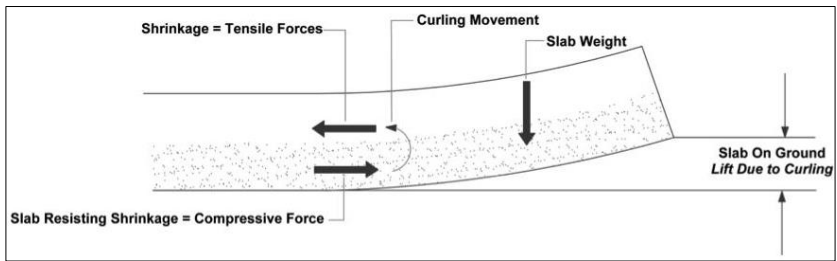


Figure 39. Curling effect



Figure 40. Crack due to curling

In part [2 Theory of drying](#) the physics of drying and how this leads to macroscopic shrinkage is covered in greater detail.

1.3 Swelling of young hardening concrete

This type of deformation takes place in the initial hardening phase of concrete. An expansion deformation of cement paste was already documented by Le Chatelier in 1900. This study observed a positive change in volume for a hydrating cement paste in fully saturated conditions (Le Chatelier, 1900).

Swelling is related to the formation of ettringite. Swelling is caused by two mechanisms:

- 1) Blast furnace slag is present in the cement. Swelling and formation of ettringite is higher in GGBFS concrete.
- 2) Lower levels of CH crystals (portlandite) and high amounts of ettringite. The morphology differ for portlandite, ettringite and CSH. Ettringite has longer and thicker-needle like crystals compared to the shorter and finer needle-like crystals of CSH (Ghasemzadeh, Shekarchi, Sajedi, Khanzadeh Moradillo, & Sadati, 2010).

Relaxation in an early phase can also be seen as *autogenous swelling* as it takes place during the phase of hardening by hydration, this is the same moment when autogenous shrinkage takes place (Klaas Van Breugel & Van Tuan, 2015). Autogenous swelling is predominantly present in mixtures with medium or high w/c. On the other hand, in high w/c pastes less autogenous shrinkage develops. This shrinkage strain might not be larger than the autogenous swelling, causing an expansion.

Besides the earlier described swelling mechanisms related to the formation of ettringite and large crystals of Portlandite (Calcium Hydroxide), there are two other mechanisms causing expansion. Firstly the formation of microcracks in the hardening system and secondly the space needed to accommodate dissolving particles (Klaas Van Breugel & Van Tuan, 2015).

Microcracks, as a result of internal tensile forces caused autogenous shrinkage. Is a statement based on older research and former assumptions in 1974 (Traetteberg, Ramachandran, & Grattan-Bellew, 1974). This is linked to the dissolving particles theory, as the cracks accommodate dissolved particles.

Expansion as a result of dissolving particles was presented for the first by T. Powers in 1948 and further explained by P. Budnikov in 1966 (Trevall Clifford Powers, 1948)(Budnikov & Strelkov, 1966).

The dissolved and hydrated elements decrease in volume, however the product forms a spacious network of fibrous-like connections. This might make the absolute volume of this system larger than the initial unhydrated mixture. The theory of expansion could be valid based on the principle of expanding low w/c cement as Breugel described or based on the moment of measurement. Concrete does shrink, but volume measurement at the moment of mixing and dissolving could show expansions. Regarding normal strength concrete, strain due to drying shrinkage is not changed in magnitude of affected by swelling.

1.4 Creep

Deformation due to creep is a result of sustained loading on concrete. The amount of creep deformation depends on the magnitude, duration and the time of loading.

Creep $\varphi(t, t_0)$ is measured as the additional deformation $\varepsilon_c(t, t_0)$ of a certain load over time compared to the initial deformation $\varepsilon_c(t_0)$ of the certain load at the moment of loading. (K. van Breugel et al., 1996)

$$\varphi(t, t_0) = \frac{\varepsilon_c(t, t_0)}{\varepsilon_c(t_0)}$$

Distinction is made between basic creep and effective creep. In basic creep, or true creep, moisture transport between the concrete element and ambient environment is assumed to be zero.

In theory, also another definition is used: creep as the sum of basic creep and drying creep. The Model code 2010 is using this approach for the creep coefficient.

$$\varphi(t, t_0) = \varphi_{bc}(t, t_0) + \varphi_{dc}(t, t_0)$$

The Pickett effect describes the effect of the non-negligible difference between the separate observations and the super position of drying shrinkage and creep.

The resulting deformation cannot simply be found by superposition of the effects. This effect was the first documented by Pickett in 1942, who observed the non-linear relation between stress and creep strains.

The 1982 report of Bažant and Wittmann, on creep and shrinkage of concrete structures, has a clear graph presenting measured deformations. The difference, when measured simultaneously, is the Pickett effect (Z P Bažant & Wittmann, 1982). See Figure 41.

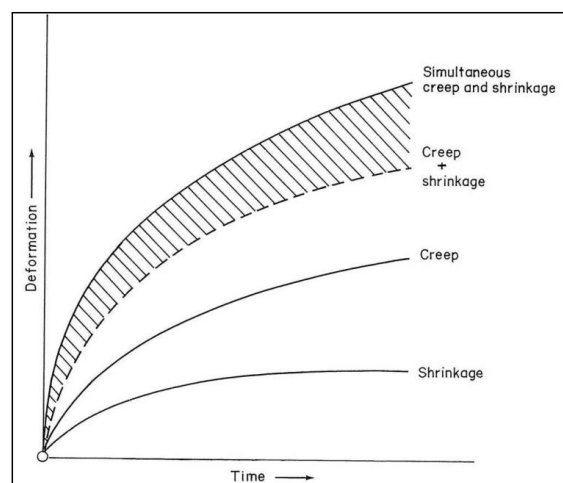


Figure 41. Representation of measured strains (Wittmann, 1982) compared to drying shrinkage strain and basic creep.

This drying-induced form of creep can also be referred to as *stress-induced shrinkage* (Idiart, 2006). This nomenclature is somewhat contradictory to what is claimed in the Model code 2010. Which states that shrinkage is a *stress-independent strain* and creep is *stress-dependent strain*. The naming used by Idiart makes a good example of the inextricable connection between shrinkage and creep. For the comprehensibility of this report, drying shrinkage strain is regarded a stress-independent strain, in line with the naming given in chapter [1.1 Shrinkage of industrial floors](#).

1.5 Relaxation

Creep is a time-, and stress-dependent deformation caused by sustained loading. Another mechanical mechanism taking place in a viscoelastic material is relaxation. Concrete can be modelled as a viscoelastic material as the response to loading is defined by an elastic stress-strain deformation and a viscous flow under sustained load over a time period.

In relaxation, internal stresses are reduced under an equal deformation. The difference between creep and relaxation is visualized in the stress-strain diagram in Figure 42.

Deformation strain as a result of shrinkage are related to internal stresses by Hooke's law.

This is valid for a simple uniaxial loaded member. When the developed strain and young's modulus are known, the unrelaxed stresses can analytically be determined. A modification of this law is needed to include the effects of creep and relaxation.

Multiple methods exist to calculate the true stresses compared to the theoretical stress. In the Eurocode, the modulus of elasticity is being reduced to get the 'effective modulus of elasticity' for concrete. Using the formula:

$$E_{c,eff} = \frac{E_{cm}}{1 + \varphi(\infty, t_0)}$$

The reduced (initial)tangent modulus of concrete gives a more realistic stress outcome. This includes the relaxation of tensile stress increments as a result of restraint shrinkage. Therefore the calculated tensile stress, including the effective modulus of elasticity, is lower than the theoretical engineering stress. In this calculation method, the occurrence of cracks is delayed compared to the calculation without creep and relaxation. In other words the material strain capacity is increased, as higher (shrinkage induced) strains are allowed with using $E_{c,eff}$ to reach fracture stress.

K. van Breugel describes in his book 'Betonconstructies onder temperatuur en krimpverkorting' in part 7.8.2 Relaxation, a relaxation formula suitable to determine the stress development for an aging structure modelled with time increments. This is based on the superposition principle for stresses acting per time increment. His equation is based on the degree of hydration and w/c ratio of the mixture.

The acting stress is calculated according an incremental time- and load-step function. This function is based on the formula used by K. van Breugel to find the tensile stresses as a result of thermal loading including relaxation.

The stress increment function as used by Breugel, gives a stress increment:

$$\Delta\sigma(\tau_j, t_i) = r \cdot \psi(\tau_j, t_i) \cdot \alpha_c(\alpha_h) \cdot \Delta T(\tau_j) \cdot E_c(\tau_j)$$

Modified to give the tension at every incremental step:

$$\sigma_c(t, t_{i-(1/2)}) = \sum_{i=1}^n [R_f(t_{i-(1/2)}) \cdot \Psi(t, t_{i-(1/2)}) \cdot \{\Delta\varepsilon_{cs}(t_i) + \alpha_c \cdot \Delta T(t_j)\} \cdot E_c(t_{i-(1/2)})]$$

K. Breugel concluded that initial stresses, as a result of the hydration process in the third period or 'acceleration' phase, are almost completely superseded by relaxation (K. van Breugel et al., 1996).

This assumption on relaxation by Breugel is also supported by other researches. In 1999, Weiss estimated a relaxation of early age developed stresses of 30% to 70% (Weiss, 1999).

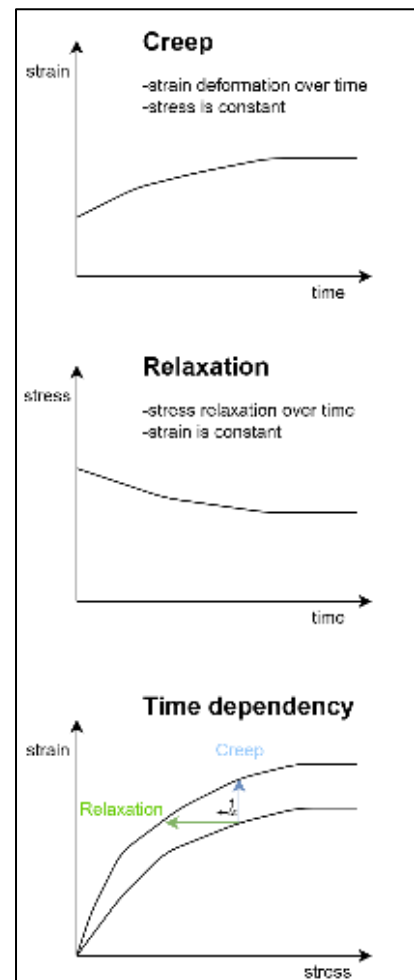


Figure 42. Creep and relaxation.

Similar results were found by Vervoort in his 2015 thesis research were creep and relaxation phenomena showed an early stress reduction of 40% to 60% (Vervoort, 2015).

In Figure 43 the stress development of an aging restrained member is illustrated. Part (a) in the figure visualizes the difference between the theoretical unrelaxed stress and stress in specimen after relaxation. Compared to the ordinary linear Hooke's law, the stress as a result of creep and relaxation is lower. Furthermore, the age of the specimen at time of cracking is delayed by a time period equal to Δt in

Figure 43 (a). Part (b) of the figure is a conceptual description of the stresses acting on an restrained specimen. Which includes internally developed stresses but exclude external loadings. A good simulation of restrained shrinkage, subjected to both creep and relaxation.

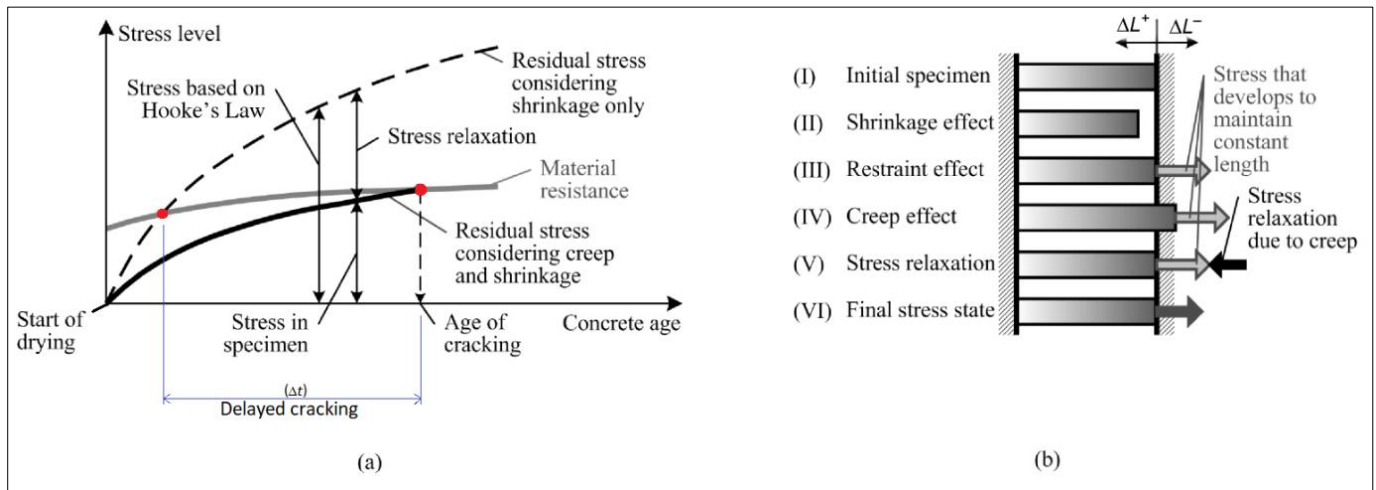


Figure 43. Stresses in a restrained concrete member. a) Stress development and b) Conceptual description of relaxation. (Gribniak, Kaklauskas, & Bacinskas, 2008)(Weiss, 1999)

N. Vervoort shows in his research that Portland cement and blast furnace cement are different in the evolution of shrinkage and relaxation. Differences are seen in the early age autogenous shrinkage and the phase after hardening, drying shrinkage.

Portland cement has more autogenous shrinkage compared to blast furnace cement due to the fact that the speed of hydration is higher. In CEM III cement, a mix of Portland and blast furnace cement, hydration is expected to be slower and autogenous shrinkage to be less. However, this is not seen in Figure 44 which shows the restraint stresses of Portland cement and blast furnace cement. It can be caused by the 'dilution effect'. In blended cement this can occur and increase hydration. Dilution is caused by the consumption of calcium hydroxide by blast furnace slag in the hydration reaction. Second to that, the slag particles are a nucleation site for formation of calcium hydroxide (Zhou, Ye, & Breugel, 2006).

In this early phase of hardening, Portland cement has a higher relaxation coefficient.

The lower relaxation measured in the mortar of blast furnace slag cement is caused by the development of a stiffer solid skeleton. More CH crystals are present in slag cement compared to Portland cement.

At $t = 600$ hours the amount of relaxation is still increasing for the Portland based mortar were it is not for blast furnace slag based mortar.

The shrinkage and relaxation of the restraint prisms by Vervoort result in an almost equal stress level at $t = 600$ hours. As seen in his results, shown in Figure 44, for the two cement types. Based on his simple uniaxial restrained shrinkage test, it could be concluded that crack formation is overestimated when relaxation is left out of the calculation. When excluding relaxation, an excess of reinforcement is used in the design. This cannot directly be concluded for concrete slab design. That would be an oversimplification because slabs differ from restraint prisms. In slabs large cross sectional differences in drying exist.

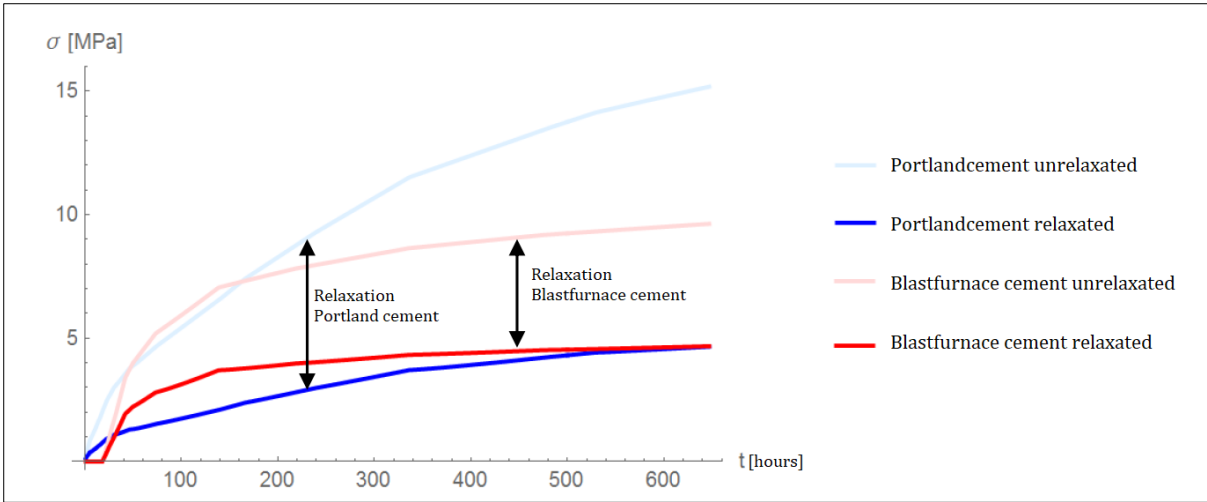


Figure 44. Relaxation of restrained tensile stresses in Portland cement and blast furnace cement (Vervoort, 2015).

In this thesis report focus in on unrestrained drying shrinkage. Specifically on the process of drying and how this can be modelled in a finite element model. This is a more fundamental approach to shrinkage from material perspective compared to measure restraint prisms. Due to the complexity of concrete behaviour, it is very difficult to distinct and quantify the responses of the material. To be able to answers the research question with adequate support, the topic of stress-dependent response cannot be left unthreaded.

1.6 Mitigation methods for shrinkage in reinforced concrete

There are methods to mitigate shrinkage and to reduce to amount of shrinkage. In this chapter a few methods are reviewed. These methods are focused on the concrete mix design (water content), cement composition including supplementary cementitious materials, chemical admixtures and internal- and external-restraints. In this research the focus is on the effects of reinforcements and aggregates on drying shrinkage in ordinary C30/37 concrete. These elements form internal restraints. Support conditions of the structure form external restraint.

1.6.1 Water content

The most coherent action is to reduce the amount of water present in the concrete mix design. In this way, less excess water will be present after hydration and subjected to drying. This is true to a certain extent.

Reducing the water content, and therefore the water-cement ratio, will decrease the consistency level of the fresh concrete. Consistency is the main indicator for workability of fresh concrete. Workability is prescribed per structure. When the water content is decreased, drying shrinkage will reduce and autogenous shrinkage will increase. Thus, lower w/c mixtures undergo relative more autogenous shrinkage. Low w/c-ratio's (<0,4) are typical for high-performance concrete (HPC). In this type of concrete, a dense microstructure is formed in the early hours and days of hardening. The dense structure prevents the flow of curing water to ensure complete hydration (D.P. Bentz & Jensen, 2004). Complete hydration should be read as potential hydration. In practice, the potential degree of hydration (DOH) is about 0,8. In low w/c-concrete, autogenous shrinkage is driven by self-desiccation which is explained in [1.2.2 Autogenous shrinkage](#).

All types of shrinkage are reduced by proper curing. In the early phase, less water will evaporate from the concrete surface. Leaving more water available throughout the cross section for hydration.

The stronger internal bonds created during decent curing, will reduce the strain caused by drying after curing.

1.6.2 Cement and supplementary cementitious materials

The most basic cement mix consists of 100% Portland cement. Often, part of the cement is replaced by another material with similar material characteristics. These are called supplementary cementitious materials (SCM). Portland cement is the most energy demanding type of cement. Ecological improvements can be achieved when part of this cement type is replaced by a less energy demanding type. Some of the SCM are industrial byproduct and therefore obtained with relative low additional energy consumption. The most well-known is Blast Furnace Slag (BFS), a rest product formed in the process of melting slag to steel.

CEM III is a cement type containing BFS. The products formed during hydration are equal, but the process and intermediate products differ. This results in a different microstructure in the hardened cement paste. The solid skeleton formed is of a denser structure compared to pure Portland cement. The speed of hydration is lower for BFS in the early phase, which is seen in the graph of Figure 45. The curves described the relative pore humidity of two measurements of CEM I and CEM III cement. RH levels are decreasing during hydration as water is consumed in the process.

In the graph, it is observed that BFS initially hydrates as a slower rate during the first two days. After these first days the level of RH starts to decrease in the BFS cement paste and compared to Portland equal RH levels are reached.

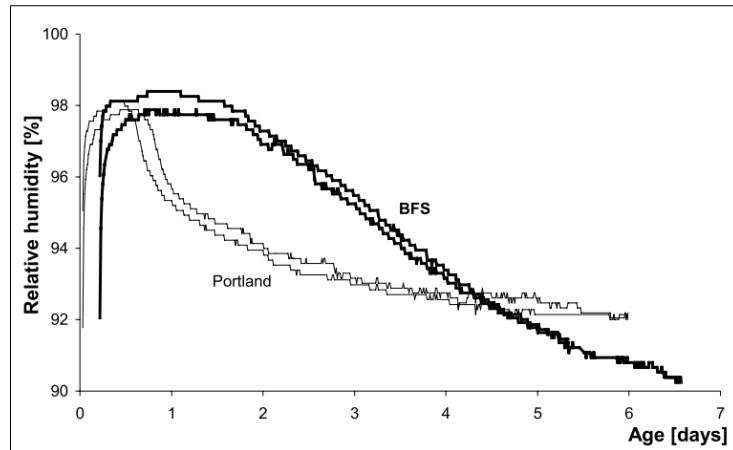


Figure 45. Internal relative humidity for Portland and BFS cement paste (Lura, 2003).

The shift in the peak of hydration can also be analyzed from the heat of evolution curves. A study on this topic is performed by Zhou and Breugel (Zhou et al., 2006). Their study included an ordinary Portland cement (OPC) paste as reference and cement pastes with 10, 30, 50, 70 and 90% of BFS replacement. An isothermal conduction calorimetry test was performed. The heat of evolution was measured together with the cumulative heat evolution. This is the total amount of heat produced during the isothermal hydration reaction. For BFS mixtures, this cumulative heat is lower compared to OPC which was seen for all BFS concentrations.

Similar to Portland cement, the reactivity is very dependent on the particle size of the material. A higher Fineness means a faster reaction with water. The fineness of cement is called the Blaine value in cement nomenclature (Jensen & Hansen, 1999)(Domone & Illston, 2010). Measured as specific surface area (m^2/kg) with a normal value of $400 m^2/kg$. Shrinkage of cement paste is increased in the autogenous phase with about 15% when the Blaine value is increased from $410 m^2/kg$ to $480 m^2/kg$ (L. Wu et al., 2017). This can be seen in Figure 46.

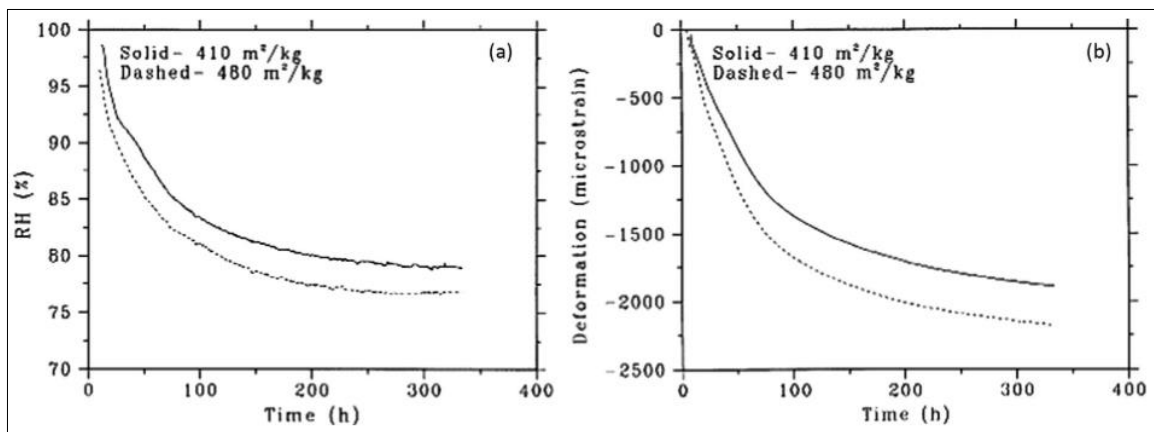


Figure 46. Effect of the Blaine specific surface value.
a) RH (%) b) autogenous microstrain ($\mu m/m$) (L. Wu et al., 2017).

With a finer particle size, a denser microstructure is formed. The internal capillary pressure in smaller voids is larger. Shrinkage can be further reduced by performing morphology studies and optimizing the shape of the cement particle. Spherical shapes form larger voids and reaching complete hydration takes longer. Increased hydration time will eventually lead to a higher degree of hydration (DOH). For these two reasons the drying shrinkage will be less when spherical particles are used.

To increase the strength of the concrete, Silica Fume (SF) can be added to the cement mixture. This byproduct of the steel industry is latent hydraulic and needs an activator. The small size of the particle, $<1\mu m$, improves the dense structure of the hardened cement paste. It is often used

as partial replacement of Portland cement in high strength concrete as it greatly improves the strength of concrete. Therefore it can reduce the amount of cement needed (Lura, 2003)(D.P. Bentz & Jensen, 2004). However, due to the fineness of this SCM, the autogenous shrinkage is increased up to a threefold for cement paste (L. Wu et al., 2017). The fine and round shape of these particles improve the workability of the concrete, lower water demand and therefore reduce drying shrinkage.

Cement mix design is a trade-off between early strength development for which fast reaction and hardening is required. Or a slower hydrating concrete with an overall higher strength on the long term.

The latter results in a reduction of drying shrinkage in concrete structures. Designing a concrete mixture for a required minimum strength at 90 days instead of the conventional 28 days, would result in less drying shrinkage.

1.6.3 Chemical admixtures

To improve the properties of concrete, admixtures can be added to mix. Admixtures are also known as additives or agents. These materials will affect the hardening process and the microstructure forming which has effect on strength, workability and durability. Many types of admixtures exist, the most important are: air-entraining, retarders, plasticizers, super-plasticizer, accelerator, expansive agent and shrinkage reducer. Most are used to improve general workability or durability. Shrinkage Reducing Additive (SRA) (also called shrinkage reducing agent or admixture) is specifically tasked to reduce shrinkage.

Different types of shrinkage reducing additives exist. They are all partly composed of alcohol. Alcohol has the effect of reducing the surface energy of water. Therefore, it changes the shape of the interaction surface between water and air. Known as the meniscus. When the surface energy is lowered in the pores in the hardening cement paste, shrinkage is reduced. The meniscus radius is increased and internal pore tensile stresses are therefore reduced.

SRA's can reduce surface tension of the pore solution by 50%. Similar numbers are published for reduction of shrinkage (Battaglia, Whited, & Swank, 2008). Holt mentions reduction of long-term drying shrinkage of 20-50% (Holt, 2001).

To have a clear understanding of the effect of all chemical admixtures on drying shrinkage, an extensive practical study should be performed. With special attention to of BFS and Alkali Activated Slag (AAS) as the market share of these cementitious materials is increasing. There is less understanding regarding the effect of SRA on these cement types. Bilek et al. published results based on experiments with AAS. They found a reduction in shrinkage when using SRA, but also a reduction in compressive strength and flexural strength (Bilek et al., 2016).

That multiple chemical admixtures, used in a single mix, might affect each other is studied by Wu et al. (L. Wu et al., 2017). For ordinary Portland cement they do claim a positive effect of SRA on tensile strength.

Interesting finding for industrial concrete floors having steel fibre reinforcement, is a potential suppression of shrinkage. Larger pores/voids at the interfacial transition zone (ITZ) were observed. This is the area between the surface of the fibre and the cement paste. An increase of the pore size will lead to lower capillary stresses (L. Wu et al., 2017).

Yoo et al., also found a positive effect of SRA on fibre reinforced concrete. Shrinkage strain was reduced. However, there study focussed on Ultra-High-Performance-Fibre-Reinforced-Concrete (UHPC). The extreme low water/cement-ratio effects the type of shrinkage. Shifting 90-95% of the contribution in the total shrinkage towards autogenous shrinkage (Yoo, Kim, & Kim, 2018).

In this thesis the focus is on drying shrinkage of moderate strength concrete. To get a clear understanding of the drying processes no chemical admixtures are included in this study.

1.6.4 Structural restraints

Crack formation in concrete is the result of locally exceeding tensile stresses due to applied loads or shrinkage under restrained conditions applied to the concrete floor. These restraints can be internally or externally.

External restraints result in (partial) restriction of movement in lateral direction. For floors on grade, the most dominant cause is the friction at interface level between the bottom of the concrete slab and the granulate subgrade. The local interface at the position of foundation piles also behaves as a restraint. The heads of these piles form a rigid support for the floor.

Internal restraints are formed by reinforcement and aggregates. As these are not shrinking themselves and have a different elastic material response than the cement paste. At the location of restraint, peak stress will occur which might lead to cracks.

The degree or level of restraint is expressed in r , this coefficient varies between 0 and 1. For a total restrained condition $r = 1$ and for zero restraint $r = 0$. In practice, structures are not fully restrained, thus: $0 \leq r \leq 1$ (Narin & Wiklund, 2012).

$$r = \frac{\text{actual imposed stress}}{\text{imposed stress at full restraint}} \quad (-) \quad 0 \leq r \leq 1$$

Determining the level of restraint is important as this parameter is needed in the analytical equations for calculating the time dependent stress development. As indicated by Breugel in his formula to calculate concrete stress by the superposition method. This formula is mentioned in part [I.5 Relaxation](#).

The degree of restraint is the key in quantifying the effect of deformation mechanisms on the total deformation.

1.6.4.1 Internal restraint

Reinforcement is the internal restraint preventing cracking due to restrained shrinkage. In the most general floor design, a fine-mesh top reinforcement of welded wire is applied. The top cover on this mesh is chosen relatively large so it can also act as tensile reinforcement under high point force in ultimate limit state.

This type of reinforcement design is used for two reasons:

-Reinforcement closely adjacent to each other, using small diameter bars, results in a uniform distribution of stresses. In this way, large individual crack formation can be prevented and the occurrence of small scattered cracks is stimulated. Smaller cracks are less likely to show spalling effects or crazing. Keeping the industrial floor flat and impenetrable for water.

-Top mesh reinforcement with a large cover helps to prevent the curling upward deflection of the slab, taking place in the corners. As a result of the nonuniform drying over the cross-section a gradient in shrinkage strain is present. By using reinforcement, this upward deflection can be limited.

A distinction between five types of reinforcement can be made based

1. Single steel welded wire mesh reinforcement
2. Bottom and top steel welded wire mesh reinforcement.
3. Steel fibre reinforced.
4. Steel fibre reinforced and a single steel welded wire mesh reinforcement.
5. Steel fibre reinforced and bottom and top steel welded wire mesh reinforcement.

1.6.4.1.1 Two way slab reinforcement

Most industrial floors are designed with steel welded wire mesh reinforcement.

In floors, they can be both at the top and bottom side or only at the top. Reason for the top location is the prevention of shrinkage cracks. At the bottom side, the soil friction helps to prevent shrinkage cracks. Furthermore, cracks are most unwanted at the top side from serviceability reasons.

For small stresses, it is the adhesive action between concrete and reinforcement steel describing the interaction. When stresses increase, shear-key effects become the contact force between the steel and concrete, as can be seen in Figure 47,

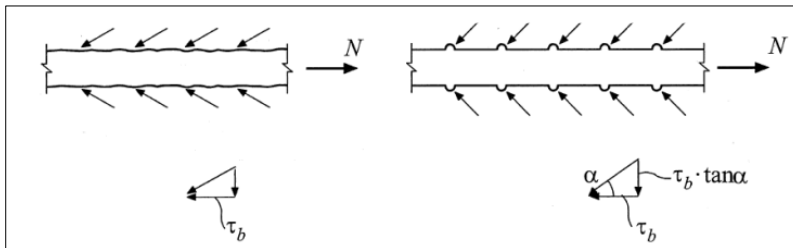


Figure 47. Shear-key force effect. (Narin & Wiklund, 2012)

1.6.4.1.2 Steel fibre reinforcement

Over the last decades, fibres have an increasing popularity in structural application. The application of steel fibres as reinforcement in concrete is called: Steel Fibre Reinforced Concrete (SFRC).

Numerous researches have shown the effectiveness in both Serviceability Limit States (SLS) and Ultimate Limit State (ULS) (Tiberti et al., 2015). Research has been done in the field of SFRC since modern use of steel fibers in the 1960s. Though, the scientific interest grew in the 1960s with the American Concrete Institute (ACI) researching the material characteristics (Abrishami & Mitchell, 1997). At the same time, the international union of experts in construction materials, RILEM, started the subject specific series of 'Symposium on Fibre-Reinforced Concretes (FRC) BEFIB'. The 'FIB'-part in the name refers to the involvement of the International Concrete Federation (FIB), the institution responsible for publishing the Model Code 2010. This code is frontrunner on design-codes regarding fibre application, whereas the Eurocode has yet to involve this in its concrete design-codes.

There are two mechanisms responsible for the improved structural properties of SFRC compared to normal reinforced concrete. The fibres give the structural residual strength and improve the stress strain behavior at the moment of cracking. The so called *tension softening*.

Residual strength is a stress that can be maintained within an element which has already passed its tensile strength. In other words; residual strength is maintained even when large strains or small cracks are present. This is a results of bonding of the fibre with the concrete. Bonding of the fibre-ends can be severely improved by the end-shape of the used fibres. The end-shape of the fibre is defined by their dimensional level of curvature. A straight steel fibre is one-dimensional: 1D, currently fibres are used up to '5D'. Extra dimensions of the fibres cause an increased level of interlocking with the concrete it is embedded in.

Steel fibres have a diameter of about 1 mm and a length between 30 and 60 mm. Tensile stresses that can be reached per type of fibre can be seen in Figure 48 as determined in a 'Pull-out' test of individual fibres.

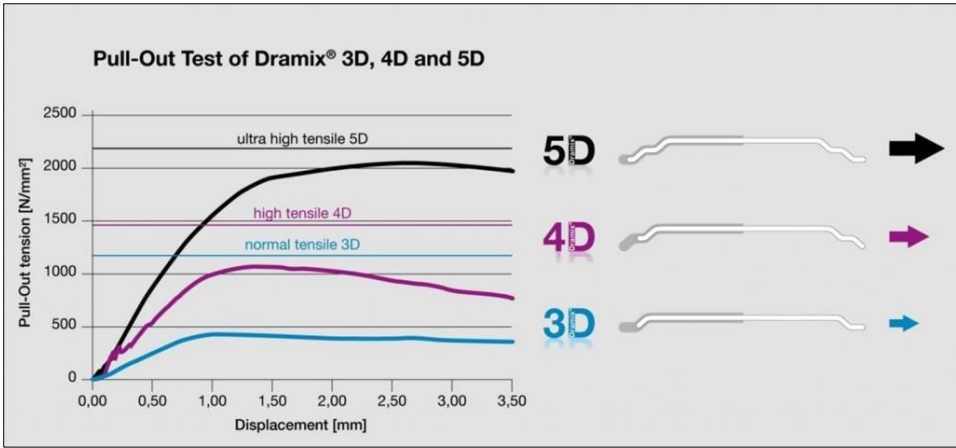


Figure 48. Bekeart fibres. Pull-out tension. (RCR Industrial Flooring, 2019)

The tensile behavior for the post-cracking phase of concrete has changed by the addition of steel fibers in the mixture. These randomly distributed steel parts can act as local reinforcement, resulting in a decrease of crack formation and crack propagation. Cracks are restrained in multiple direction because the fibres form a three-dimensional distribution of reinforcement.

The tensile strength of SFRC is expressed as residual flexural tensile strength.

To determine this residual flexural tensile strength, a three-point-bending test on a notched beam is performed. This procedure is described in the code NEN-EN 14651 (2005). The Model Code 2010, which describes fibre reinforced concrete better than the Eurocode, also refers to this specific method. Dutch based 'Civieltechnisch Centrum Uitvoering, Research en Regelgeving' (CUR) has written an recommendation on SFRC design (CUR - Commissie Staalvezelbeton, 2012).

The deformation of an SFRC element after cracking is presented in the 2012 CUR recommendation. For unreinforced concrete, a brittle crack is seen at the moment the applied stress reaches the tensile strength. SFRC shows a tension-softening and residual strength after cracking as effect of the fibres taking tensile stresses (Figure 49). Residual flexural strength is determined based on the outcome of an crack mouth opening displacement (CMOD). The method of determining the CMOD is described in the CUR-recommendation. The graph in Figure 50 is a typical CMOD-test result. The used ultimate design tensile strength is the found flexural tensile strength multiplied with a safety factor. The CMOD method is used for structures using SFRC according to the FIB Model Code 2010 or the RILEM code (Fib bulletin 65, 2012) (RILEM TC 162-TDF, 2003).

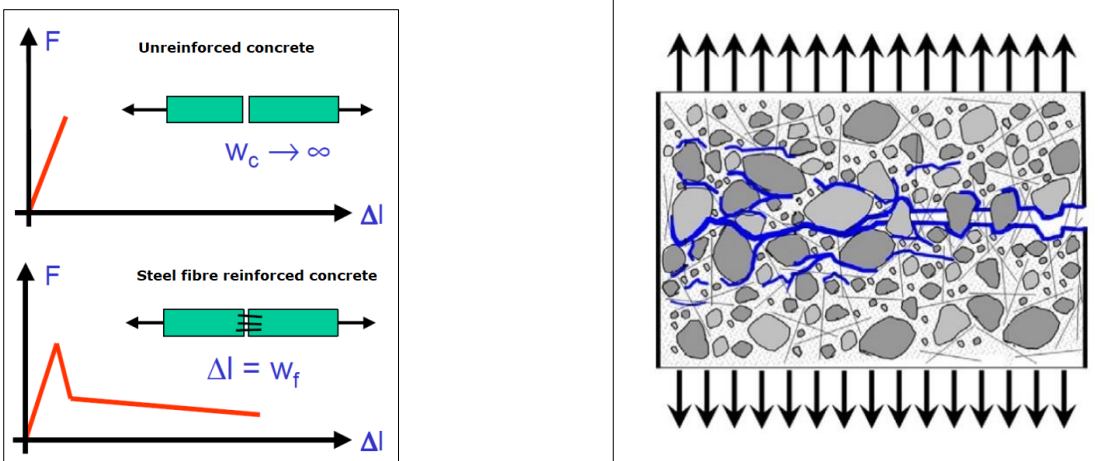


Figure 49. a) Effect of steel fibres on hardened concrete (CUR - Commissie Staalvezelbeton, 2012) b) Effect of steel fibres in macro-, and microcracking.

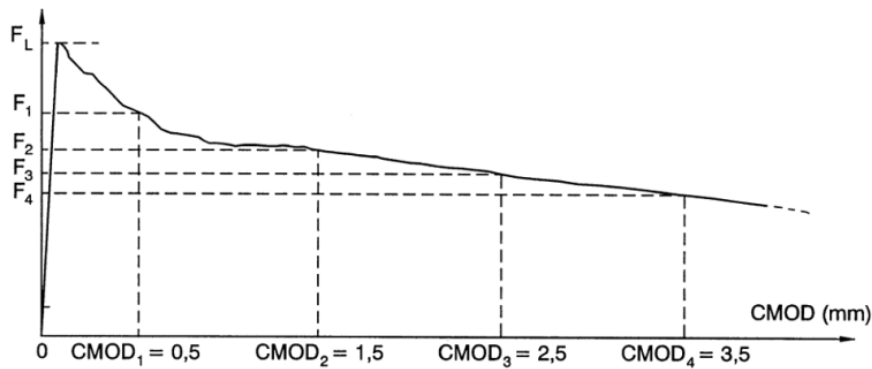


Figure 50. CMOD graph showing tension softening material behaviour. (CUR - Commissie Staalvezelbeton, 2012)

The steel fibres added to the concrete mixture will be around 1,5% of the total weight. ABT BV. uses 35 kg/m^3 for standard fibre reinforced hybrid floor design. Beside contributing to the ductility of the material and changing the stress-strain behaviour, these fibres have an influence on shrinkage effects. Especially autogenous shrinkage deformation is affected by the steel fibres.

Multiple researches have shown the ability to suppress shrinkage of concrete by fibres.

Two mechanisms can be held responsible.

Firstly, the stiffness of this local reinforcement. It has a high elastic modulus compared to the formation of the hardened skeleton. Link between the skeleton and the fibre is created through bond stress.

Secondly, in the young hardening concrete, a thin layer of water film, only a few micro-meter, is formed at the steel surface of the fibre. In this space, calcium hydroxide crystals grow without other constraints and form a reticular like structure at the interface area between the steel and concrete matrix (or hardened cement paste) (L. Wu et al., 2017).

Reported in a study by Yu and Zhao is the decline of contribution of steel fibres in the reduction of shrinkage when the cement paste has hardened. During the autogenous shrinkage phase, the contribution of steel fibres is beneficial. However, when the elastic modulus of the hardened concrete has increased, the contribution of steel fibres is decreasing accordingly (Yu & Zhao, 2013).

It can be concluded that reinforcement has a retaining effect, therefore reduces drying shrinkage. The gain of a better understanding in the hardening and drying process of cementitious materials and the retaining effect of reinforcement, will lead to better designs. The knowledge to include this in a structural design has to come from material understanding. Later on in this research, the drying shrinkage of a concrete unreinforced prism will be simulated using finite element modelling. The goal is to mimic the results which were obtained experimentally. A subsequent research should be performed on concrete (prisms) including the effects of reinforcement.

1.6.4.1.3 Influence of aggregates

The volume of aggregates can take up to 60% ~ 70% of the concrete mixture, making it a highly heterogenous material. This is reflected in the material parameters. The initial tangent or modulus of elasticity is about 2,5 times higher for aggregate compared to cement paste ($E_c = 40.000 \text{ MPa}$ and $E_a = 40.000 \sim 100.000 \text{ MPa}$) (Grassl et al., 2008).

These aggregates are preventing the shrinking matrix of deforming by devolving a stress field around and between these aggregates. Figure 51 is taken from a study performed in 2002 by researchers at Delft University of Technology and also used in the report by A.E. Idiart (Bisschop & Mier, 2002)(Idiart, 2006).

It can be clearly seen in the micrograph of Figure 51, taken from the dried specimen, that bond cracks between the aggregate and cement paste are produced and also radial cracks between the aggregates. These cracks are induced by the tensile stresses as a result of drying of the cement

paste. Bond cracks at the surface of the aggregate, the Interfacial Transition Zone (ITZ), are also called *abrasion* cracks (R. Liu, Xiao, Liu, Guo, & Pei, 2019). ITZ is important for permeability and diffusion properties of the material. In other words, the speed of drying and shrinkage development. Liu et. al. studied the beneficiary effects for the ITZ, when adding nano-sized silica to the concrete mixture. This resulted in a densification of the hydration products formed in the surface zone of the aggregates. A smaller 'gap' in the ITZ, as seen in Figure 51 (c), will result in lower oxygen diffusion, oxygen permeability and water sorptivity (Grassl et al., 2008). The numbers in Figure 51 (c) are indicating the spot of CaO/SiO₂ ratio-estimation. This is out of the scope of this thesis research. However, it can be said that the Ca/Si ratio is higher near the aggregate and in the ITZ, compared to the cement matrix. This is due to differences in concentration. The concentration of Ca(OH)₂, Portlandite crystals, is higher at the ITZ and the concentrations of calcium silicate hydrate (CSH) is less. As is in line with the findings in part [I.1.2 Hydration](#).

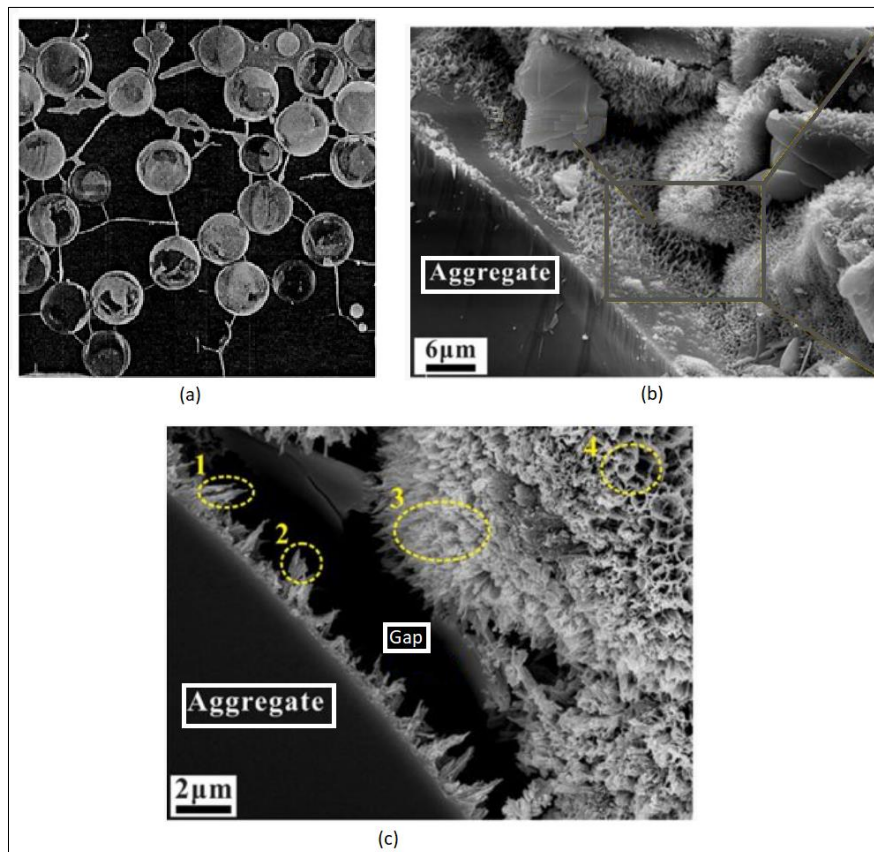


Figure 51. a) Cement paste with 6 mm glass spherical inclusions. Microcracking in radial direction and at the sphere surface. (Bisschop & Mier, 2002)(Idiart, 2006) b) Interfacial Transition Zone seen through a field emission scanning electron microscope (FE-SEM) c) Gap is seen between the aggregate and the cement matrix. (R. Liu et al., 2019)

Another outcome found by Bisschop and Mier was the fact that, the larger the size of the aggregates and the larger the volume fraction of aggregate present in the concrete, the greater the degree of internal restraint and amount of microcracking (Bisschop & Mier, 2002).

Microcracking is induced in the drying matrix as radial cracking and bond cracks on the aggregate surface are in the order of micrometres (Z. Wu, Mac, Wong, & Buenfeld, 2013).

In the study done by Z. Wu et. al., multiple samples of CEM I 32,5 R at a W/C of 0,5 were oven dried at 105 °C and normal dried at 21 °C with an 35% RH. Another set of specimen was stepwise dried at 21 °C with decreasing RH levels, from 100 % to 3%. They found microcracks occurring in the range of 1 μm to 60 μm. Their results showed that with an increased severity of drying, the amount of microcracks is more. The same is found for the widths and lengths of the microcracks. These microcracks contribute to the moisture transport capacity of the concrete. To minimize strain due to drying shrinkage, proper curing during hardening is needed.

In Table 7, the relation between the shrinkage at 6 months and the aggregate/cement ratio of the concrete mixture is shown. More aggregates will result in lower shrinkage which is due to the restraining effect and the relative lower presence of cement paste.

aggr./cem. Ratio	Shrinkage at 6 months ($\times 10^{-6}$) for w/c ratio of:			
	0,4	0,5	0,6	0,7
3	800	1200	----	----
4	550	850	1050	----
5	400	600	750	850
6	300	400	550	650
7	200	300	400	500

Table 7. Values of shrinkage in concrete. Prisms with a squared cross section of 127mm², exposed to 50% RH at a temperature of 21 °C. (Neville & Brooks, 1991)

The same researcher also presented a theory to relate the shrinkage of hardened cement paste (HCP) to concrete. In this expression, the HCP shrinkage is reduced by the volume fraction of the aggregate. Thereafter, it was corrected by an exponential correction factor (Neville & Brooks, 1991)(Idiart, 2006).

$$\varepsilon_c = (1 - a)^n \cdot \varepsilon_{HCP}$$

- ε_c =shrinkage of concrete
- ε_{HCP} =shrinkage of hardened cement paste
- a =aggregate volume fraction
- n =correction factor. Typically between 1.2 and 1.7 (Neville & Brooks, 1991).

An more accurate correction, based on the restraining effect of aggregates, is performed with Pickett's model (Pickett, 1956). As used by T. Lu and other researchers (Lu, 2019)(Lura, 2003)(E.I. Tazawa, R. Sato, E. Sakai, & S. Miyazawa, 2000). In the model of Pickett, the effect of a single spherical aggregate particle is calculated. This effect is interpolated over the concrete based on the relative content of aggregate particles. The correction factor based on Pickett's model is denoted by β .

$$\varepsilon_c = (1 - a)^\beta \cdot \varepsilon_{HCP}$$

- β =correction factor

$$\beta = \frac{3(1-v_p)}{1+v_p+2(1-v_s)\left(\frac{E_p}{E_s}\right)}$$

- v_p =Poisson's ratio of cement paste 0.2
- v_s =Poisson's ratio of aggregate particle 0.3 (Pichler et al., 2007)
- E_p =Elastic modulus of cement paste MPa
- E_s =Elastic modulus of aggregate particle 50000 MPa (Pichler et al., 2007)

This formula of Pickett will be used in the FE modelling part of this research. Modelling is performed based on the mechanics of cement paste. The level of shrinkage in cement paste is higher than for concrete due to the internal restraint. By applying this formula, a strain development of drying concrete should be found which is comparable to experimentally obtained data. The calculation is performed in chapter [2.5 Drying shrinkage at equilibrium](#).

I.6.4.2 External restraint

A concrete industrial floor is subjected to multiple structural restraints. These are primarily formed by the subgrade supporting the floor and by interruptions in the floor for structural columns carrying the roof structure.

Restraint by subgrade is valid for slab-on-grade design as well for slab-on-piles. Even though, most of the loads are transferred to the foundation piles. Both floor types are shrinking and have a shear interaction with the subgrade. The slab-on-piles has additional points of restraint due to monolithic connection with the foundation piles. A typical section of these floor types is seen in Figure 52 (Narin & Wiklund, 2012). The perimeter can also be executed without 'perimeter-strip'.

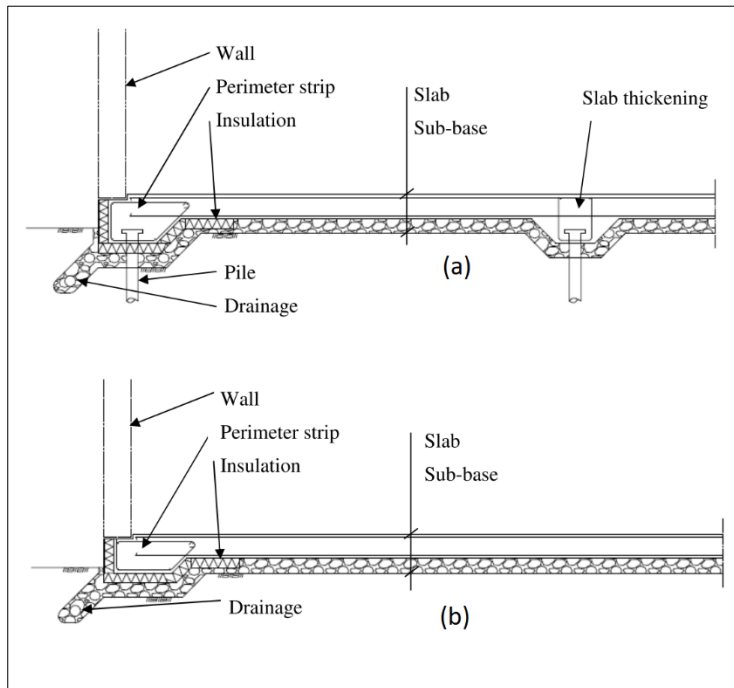


Figure 52. Section of industrial floor. (a) slab-on-pile (b) slab-on-grade.

Friction with the subgrade prevents free movement of the deforming concrete. This is caused by the slip resistance at the interface. The slip resistance can be seen as shear. Besides shear, bearing and adhesive stresses are present at the interface. This is illustrated in Figure 53.

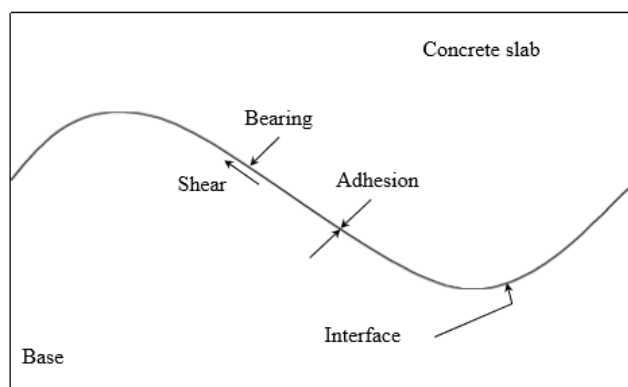


Figure 53. Interface stresses between concrete slab and subgrade (Wimsatt, McCullough, & Burns, 1987).

In the research of Vervoort on restrained shrinkage, a static friction coefficient (μ_s) is used in the calculation (Vervoort, 2015). The static friction force can be calculated by multiplying this coefficient by the force caused by shrinkage strain. The force due to shrinkage, perpendicular to the plane, is the strain multiplied with the stiffness of the material.

$$F_W = \mu_s \cdot F_N$$

F_W =static friction force

μ_s =static friction coefficient

F_N =Normal force perpendicular to the plane

The friction coefficient used by Vervoort is 0.08. This is equal to the $K_{winkler}$ value used in the research performed by Tiberti et al. (Tiberti et al., 2018). Tiberti is using the interfacial friction stress to model differences in shrinkage strain for the bottom and top side of a slab-on-grade.

The Winkler soil stiffness model for elastic response is used. This Winkler soil stiffness, $K_{Winkler}$, is estimated to be $K_{Winkler} = 0.08 \text{ N/mm}^3$. The estimated value is an average of loose sand (0.04 N/mm^3) and clay (0.12 N/mm^3) soil stiffness values (Wimsatt et al., 1987). The local interfacial friction behavior can be described by resistance models, as Mohr-Coulomb or Drucker-Prager, for finite element (FE) modelling. Also a stress-slippage friction relationship needs to be included in the FE-model. Studies have stated that the development of the stresses and related slippage of the slab-on-grade can be described with a bilinear stress-slippage relation. In the study performed by Tiberti et al., a bilinear curve is used until a predetermined slab slippage (δ_0, τ_0) point. An incremental elastic response is assumed up to this point followed by a constant ideal-perfect-plastic trajectory. The amount of drying shrinkage measured at the bottom of the slab-on-grade was 60% of the deformation on top.

It should be noted that these values differ for slab-on-pile type of floors. As a result of the pile foundation supporting the floor, the distribution of forces differ. Especially the internal moment-line. It is likely to have a higher tensile stress at the top section of the floor due to the force exerted by the piles. Combined with an higher drying shrinkage at the top side, more cracks are likely to occur in this floor type.

In this thesis research, the focus is on jointless industrial floors. Floors which do have joints are divided in sections. The aim of this design is to 'release' the build-up stress due to shrinkage in the joints. Making these intentionally made saw cuts wider instead of causing local excess tensile stresses. Which might form unwanted cracks. However, saw-cuts or full section joints are local weaknesses. At these positions, wear and tear is predominantly reducing the serviceability level of the industrial floor. Therefore, a jointless floor is preferred from user perspective.

1.7 Concluding remarks on response of materials

This theoretical part on shrinkage has introduced the mechanisms behind time- and stress-(in)dependent strains. It can be concluded that drying shrinkage is the most profound type of deformation, causing a reduction in serviceability of a concrete floor slab.

As was also the conclusion of the Concrete Society in their 34th report on 'concrete industrial floors' (Concrete Society, 2014).

Creep and relaxation are very complex mechanisms. The true behavior of a concrete member cannot be analyzed without these mechanisms. However, to be able to give an accurate judgement on the key component drying shrinkage, creep and relaxation need to be excluded from the analysis. In this way, a better understanding is gained in the exact physics behind drying shrinkage.

The Appendix II of this thesis the construction codes on shrinkage calculation are covered.

Appendix II: Codes & Structural conditions

In this appendix the background of the Eurocode and Model code is presented. The focus is on the accuracy of the shrinkage calculation prescribed in the codes. After this introduction, the concrete object studied in the research is introduced with the related structural conditions. Thereafter, the shrinkage of the concrete object is calculated according to the standards.

II.1 Eurocode 2 and Model code 2010

Concrete structures are designed according to the governing rules and legislation for the specific project and location. Pleadable construction standards are present in most developed countries. In the Netherlands, first civil engineering publications were issued by the Royal Institute for Engineers (KIVI) (KIVI, 2019). In 2012, the Dutch national building degree has been rewritten including the European Union centralized codes, known as the Eurocode.

The Comité Européen de Normalisation (CEN) is the institute in Europe responsible for distributing a coherent set of standards and specifications. The code applicable to concrete structures is the Eurocode 2 (NEN, 2011). Uniform codes are needed to ensure safe and durable structures. The codes are a product of expert panels and advisory groups of the CEN. Concrete has been studied in great detail regarding structural behavior and characteristic of the material components. This has been done by numerous researchers and multiple institutions. Findings have been published in journals as 'Cement and Concrete Research', by Elsevier since 1971 (American Concrete Institute, 1971). Another professional group active in research and publishing guidelines is the Fédération Internationale du Béton (FIB). FIB is known for publishing the Model codes. The most recent version of this code is the Model code 2010, the shrinkage calculation of this version is used in this thesis to predict the development of drying shrinkage (Fib bulletin 65, 2012).

In this chapter the calculation procedure of shrinkage according to the Eurocode is covered (NEN, 2011). The valid Eurocode documentation, at moment of writing this thesis research, is 'Eurocode 2: Design of concrete structures – Part 1-1: General rules and rules for buildings'. Officially titled: 'NEN-EN 1992-1-1' 2011 publication (NEN, 2011). This publication is used hereafter.

The Eurocode is currently under revision, a renewed version is expected to be published in 2020. A specific Task Group, TG7 of the committee: CEN/TC 250/SC2, is responsible for *time dependent effects*. This CEN-committee is responsible for the revision of the Eurocode structural design codes. The soundness and overall modelling consistency will be improved with the renewed version. According to a 2016 document of The Concrete Society in the UK, the current calculation method for drying shrinkage is up to 50% off and for creep up to 5% off (The Concrete Centre, 2016).

In an update of the Task Group in 2015 by Müller and Acosta, it became clear that the creep and shrinkage calculations in the Eurocode will be changed. The new shrinkage model will be based on the Model code 2010. Using this method, a uniform approach is set for both normal- and high-strength-concrete.

While the background of the Eurocode shrinkage calculations are not known (Müller & Acosta, 2015). For the Model code, this is documented well. The shrinkage formulas behind drying shrinkage are based on the sound theory of thermodynamics. The diffusion of heat and moisture are based on equal theory, both substantiated on Fick's law of diffusion. In this research thesis, the drying of concrete is modelled based on this theory. Background theory is given in part [2.6 Diffusion](#) and is used for the finite element model.

II.2 Structural conditions

The shrinkage strain is calculated for a prism. At ABT, a series of concrete prisms has been measured on weight change and deformation due to shrinkage.

The scope of the research question in this thesis is on industrial floors. Prior to efficiently reflect drying shrinkage in a slab, the theory is tested on a smaller scale. Therefore, the shrinkage behaviour of the measured prisms is researched. These elements are 150 mm by 150 mm and 600 mm in length, as in Figure 54. The finite element(FE) model that is used in this thesis to simulate drying, is based on the same prisms. In this way the outcomes of the FE-method can be compared with the Eurocode calculation. This concrete prism will be referred to as *test beam*.

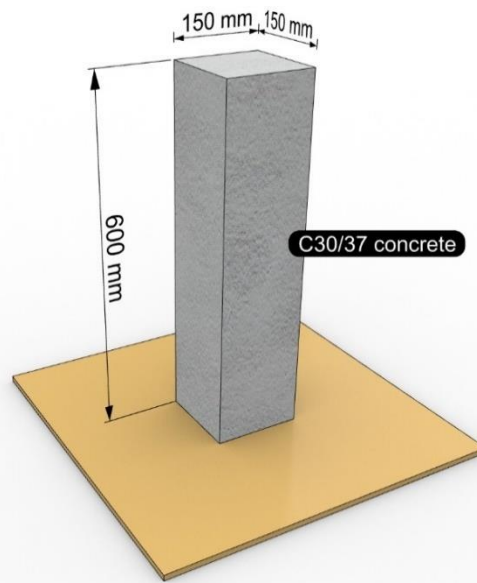


Figure 54. Dimension of the concrete prism.

Parameters used to calculate the total shrinkage strain can be found in Table 8. The coefficients are based on normal hardening cement (type-N).

factors		Concrete C30/37	
f_{ck}	$N/mm^2(= MPa)$	30	Characteristic compressive strength
$f_{ck,cube}$	MPa	37	Characteristic cube strength
f_{cm}	MPa	38	Mean compressive strength
f_{cm0}	MPa	10	Initial strength
$\epsilon_{ca}(\infty)$	$\mu m/m$	50	Nominal autogenous shrinkage
$\epsilon_{cd,0}(\infty)$	$\mu m/m$	400	Nominal drying shrinkage
$\beta_{as}(t)$	(-)		Time coefficient autogenous
$\beta_{ds}(t, t_s)$	(-)		Time coefficient drying
h_0	mm	75	Notional size
A_c	mm^2	22.500	Cross-sectional area
u	mm	600	Perimeter of <i>test beam</i> exposed to drying
k_h	(-)	1	Coefficient based on h_0
t_s	$days$	28	End of curing and start of drying
RH	%	65	Ambient relative humidity
RH_0	%	95	Moisture cured concrete
β_{RH}	(-)	1,12	Coefficient based on relative humidity
α_{ds1}	(-)	4	Coefficient depending of cement type
α_{ds2}	(-)	0,12	Coefficient depending of cement type

Table 8. Parameters for Eurocode shrinkage strain calculation.

All the shrinkage strain formulas in the Eurocode are based on the strength properties of concrete, besides time and ambient relative humidity. In these calculations, the effect of cement type, water/cement-ratio, aggregate content, supplementary cementitious materials and ambient temperature are not specifically included. The future Eurocode is expected to have additional parameters concerning these parameters.

At ABT, the prisms were kept in a climate room with controlled temperature and humidity for 28-days. Temperature was kept at 20 °C and relative humidity of the air at 100%. During these days, the hardening took place. The prisms have been measured on strain on a weekly basis. Measurements started at the 28th day and stopped at the 112th day.

Table 9 shows the concrete mix design for the concrete prisms at ABT.

Mix design				
mix quantity			material density	
w/c-ratio	0,5	(-) kg/kg		
cement	350	kg/m ³	3150	kg/m ³
water	175	kg/m ³	1000	kg/m ³
aggregate	1180	kg/m ³	2650	kg/m ³
sand	685,31	kg/m ³	2650	kg/m ³
air	1	%		
concrete density	2390	kg/m ³		
aggregate + sand=			1865,31	kg
aggregate/cement-ratio=			5,33	(-)
aggregate ratio on total volume=			0,70	m ³ /m ³

Table 9. Concrete mix design ABT prisms.

II.3 Shrinkage calculation based on the Eurocode 2

In the Eurocode 2, section 3.1.4, shrinkage is calculated. The total shrinkage strain (ε_{cs}) is the superposition of drying shrinkage strain (ε_{cd}) and autogenous shrinkage strain (ε_{ca}).

$$\varepsilon_{cs} = \varepsilon_{cd} + \varepsilon_{ca}$$

Autogenous strain is the nominal strain value ($\varepsilon_{ca}(\infty)$), based on characteristic strength, multiplied with a time-dependency factor ($\beta_{as}(t)$).

$$\varepsilon_{ca}(t) = \beta_{as}(t) \cdot \varepsilon_{ca}(\infty)$$

Where:

$$\varepsilon_{ca}(\infty) = 2.5 \cdot (f_{ck} - 10) \cdot 10^{-6}$$

$$\beta_{as}(t) = 1 - \exp(-0.2 \cdot t^{0.5})$$

Drying shrinkage strain is the nominal unrestrained drying strain, multiplied with a time-dependency factor and a coefficient depending on the notional size.

$$\varepsilon_{cd}(t) = \beta_{ds}(t, t_s) \cdot k_h \cdot \varepsilon_{cd,0}$$

Where:

$$\beta_{ds}(t, t_s) = \frac{t - t_s}{(t - t_s) + 0.04 \cdot \sqrt{h_0^3}}$$

$$k_h = 1 \text{ (-)} \quad (\text{as } h_0 < 100 \text{ mm})$$

$$h_0 = \frac{2A_c}{u}$$

$$\varepsilon_{cd,0} = 0.85 \left[(220 + 110 \cdot \alpha_{ds1}) \cdot \exp(-\alpha_{ds2} \cdot \frac{f_{cm}}{f_{cm0}}) \right] \cdot 10^{-6} \cdot \beta_{RH_{EC2}}$$

$$\beta_{RH_{EC2}} = 1.55 \left[1 - \left(\frac{RH}{RH_0} \right)^3 \right]$$

For the initial relative pore humidity, RH_0 , a value of 100% is suggested. This is true for concrete subjected to drying after pouring. However, the concrete prisms at ABT were cured for 28-days in a climate chamber. An initial 5% decrease of internal RH-level is assumed due to water consumption by hydration. Substantiation on this assumption is given in chapter [2.4.2 Degree of hydration](#).

The graphical result of the Eurocode calculation on these prisms is seen in Figure 55.

In the graph, it is seen that in the first 28-days 65% of the nominal autogenous shrinkage has developed. After 28-days the prisms are subjected to drying. The drying shrinkage will start to develop. A steep increase in total strain during the first days of drying is present.

During 84 days, the concrete *test beam* was subjected to drying.

Based on the Eurocode, the total strain due to shrinkage is $330 \mu\text{m}/\text{m}$ after 84 days of drying. Autogenous shrinkage accounts for 13% of the total shrinkage at the final calculation step.

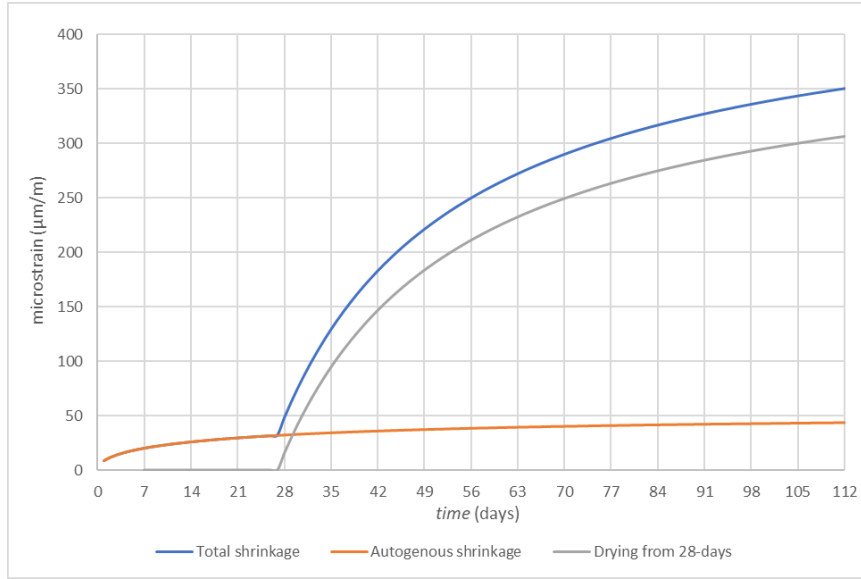


Figure 55. Shrinkage strain of concrete prism. According to the Eurocode (NEN, 2011).

The aggregate/cement-ratio was used by Neville & Brooks to estimate the amount of shrinkage after 6-months of drying (Neville & Brooks, 1991). Their results can be seen in Table 7. Interpolating these values for an aggregate/cement ratio of 5.33, gives a microstrain of 534 $\mu m/m$. This is more than what is calculated using the Eurocode. The overestimation of shrinkage strain by Neville & Brook could be linked to the time of their research. Between the year 1991 and the time of publication of the NEN, developments have been made on material research. Especially on supplementary cementitious materials (SCM), with abilities to refine the material structure and reduce shrinkage.

II.4 Shrinkage calculation based on the Mode code 2010.

In the CEB-FIB Model code 2010, section 5.1.9.4.4, shrinkage is calculated for isothermal conditions. The total shrinkage strain (ϵ_{CS}) is the superposition of drying shrinkage strain (ϵ_{cds}) and autogenous shrinkage strain (ϵ_{cas}).

$$\epsilon_{CS}(t, t_s) = \epsilon_{cds}(t, t_s) + \epsilon_{cas}(t)$$

Autogenous strain is the notional autogenous coefficient ($\epsilon_{cas0}(f_{cm})$), based on the mean compressive strength, multiplied with a time-dependency factor ($\beta_{as}(t)$).

$$\epsilon_{cas}(t) = \epsilon_{cas0}(f_{cm}) \cdot \beta_{as}(t)$$

Where:

$$\epsilon_{cas0}(f_{cm}) = -\alpha_{as} \left(\frac{f_{cm}/10}{6+f_{cm}/10} \right)^{2.5} \cdot 10^{-6}$$

$$\beta_{as}(t) = 1 - \exp(-0.2 \cdot t^{0.5}) \quad \beta_{as}(t) = \text{equal to the Eurocode 2}$$

Where:

α_{as} = coefficient depending on the cement type

Drying shrinkage strain is the notional drying coefficient, based on the mean compressive strength ($\epsilon_{cds0}(f_{cm})$), a coefficient for the ambient RH ($\beta_{RH_{MC}}(RH)$) and a time-dependency factor ($\beta_{ds}(t - t_s)$).

$$\epsilon_{cds}(t, t_s) = \epsilon_{cds0}(f_{cm}) \cdot \beta_{RH_{MC}}(RH) \cdot \beta_{ds}(t - t_s)$$

With:

$$\varepsilon_{cds0}(f_{cm}) = [(220 + 110 \cdot \alpha_{ds1}) \cdot \exp(-\alpha_{ds2} \cdot f_{cm})] \cdot 10^{-6}$$

$$\beta_{RH_{MC}}(RH) = \begin{cases} -1.55 \cdot \left[1 - \left(\frac{RH}{100}\right)^3\right] & \text{for } 40 \leq RH < 99\% \cdot \beta_{s1} \\ 0.25 & \text{for } RH \geq 99\% \cdot \beta_{s1} \end{cases}$$

$$\beta_{ds}(t - t_s) = \left(\frac{(t - t_s)}{0.035 \cdot h_0^2 + (t - t_s)}\right)^{0.5}$$

$$\beta_{s1} = \left(\frac{35}{f_{cm}}\right)^{0.1} \leq 1.0$$

Where:

α_{ds1} & α_{ds2} = coefficient depending on the cement type (type 'N'[Normal] is used)

t = concrete age in days

t_s = concrete age at the beginning of drying in days

Between the design codes of the Eurocode 2 and the Model code 2010 there are similarities in the formulas to calculate drying shrinkage. The (β_{RH}) coefficient describing the effect of ambient relative humidity is exactly the same in both codes: ($\beta_{RH_{EC2}} = \beta_{RH_{MC}}$). However, the coefficients accountable for the influence of time and concrete strength are slightly different.

The shrinkage calculation according the Model code 2010 is plotted in a graph with the Eurocode result in Figure 56.

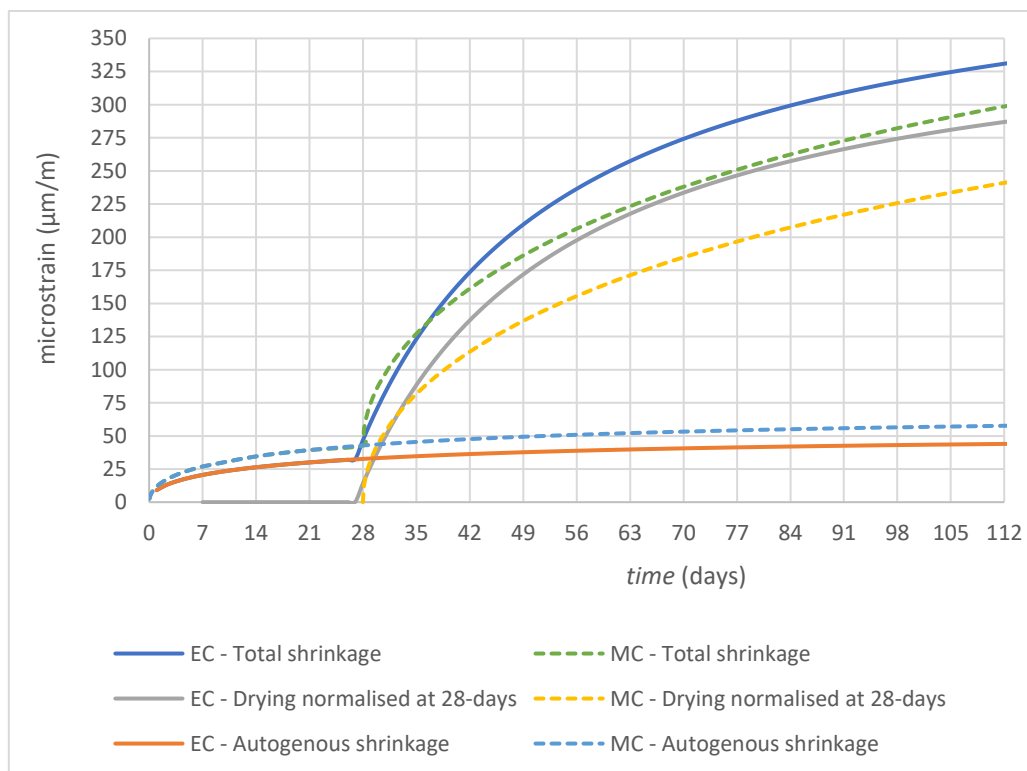


Figure 56. Shrinkage strain of concrete prism. Calculated using the Model code 2010 and the Eurocode 2.

II.5 Concluding remarks on Codes & Structural conditions

Drying shrinkage according to the Eurocode and the Model code are developing according to a similar shaped trajectory. However, after 84 days of drying, the Eurocode calculation gives $287 \mu\text{m}/\text{m}$. This is 19 % more than the outcome of the Model code.

The influence of the ambient relative humidity during drying is included using the same formula in both codes. Thus, there is no difference in the theoretical approach of drying based on relative humidity levels.

A study by Tiberti et al., focussed on implementation the Eurocode 2 shrinkage calculation in a FEM model of an industrial slab floor (Tiberti et al., 2018). This is interesting from structural modelling perspective. However, the true origin of shrinkage is left behind. The amount of shrinkage is modelled as an pre-determined deformation.

The research question states that the goal is to produce a parametric FEM model efficiently reflecting shrinkage behaviour. For this, the source of drying shrinkage should be understood. First step will be to model the drying and resulting strain of the material before advancing to a full structural model including the simulation of cracks. In this research thesis, the drying strain of concrete prisms will be simulated in a finite element model. When proven successfully, this can be included in a full structural model.

In part [3.3.2 Drying shrinkage strain](#), the results of the finite element model are compared with the measured deformations of the concrete prisms. Furthermore, in this comparison the outcome of the Eurocode and Model code on shrinkage will be included. Resulting in a judgement about the performance of the Eurocode and the Model code.

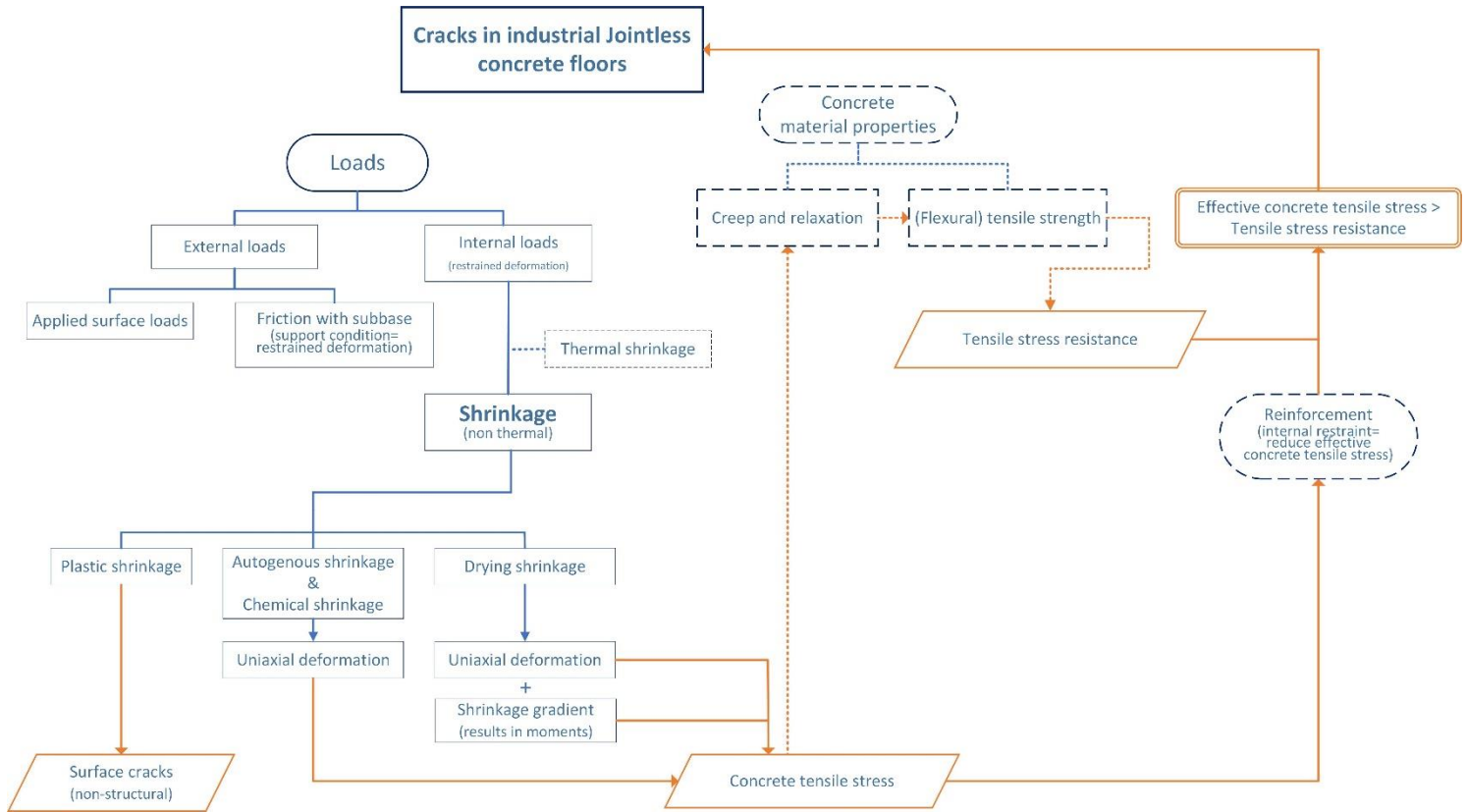


Figure 57. Cracks in jointless concrete floor, originating from shrinkage.

Appendix B

Environmental impact of the construction industry is significant. Energy is consumed in the mining industry for retrieving raw materials, transport and processing. The ongoing urbanization and will for better infrastructure is driving the demand for concrete structures and therefore cement production. In the chart in Figure 58 this increase is clearly seen. In the assessment report published in 2014 by the intergovernmental panel on climate change (IPCC) it has become clear that the growing demand for cement has increased and surpasses the general growth tendency for minerals (UNEP; WMO, 2014).

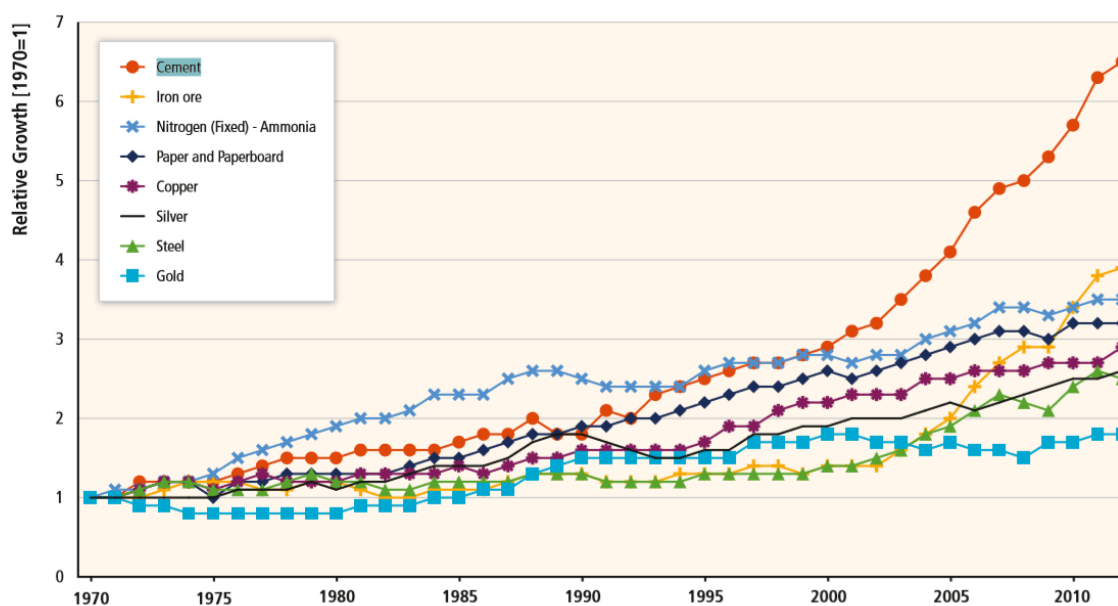


Figure 58. World's growth of minerals and manufacturing products (1970=1) (UNEP; WMO, 2014).

Large amount of energy is needed for drying of the raw material and in the kiln for the clinkering, pyro-processing, stage of cement production. Temperatures of 1400 to 1500°C are needed for the process in which calcium carbonate reacts with silica-bearing minerals to form calcium silicates. (Domone & Illston, 2010)

Different kind of kiln exist, in simple these are wet-, and dry-process kilns. The general used method in modern times is the dry process. Here the raw material entering the kiln is pre-heated in a heater-tower, this is a more energy efficient method for producing clinker. For the production of one ton of Portland cement on average 3.4GJ/t is needed. To be able to match with the Sustainable development Scenario (SDS) for 2030, this number should decrease by 0,5 GJ/t per year. In Russia and Caspian countries the cement production is mostly still done according the less energy effective wet-kiln process having a thermal energy demand of 5.4 GJ/t (Vass et al., 2019).

In 2009 the global average for CO₂ emission per ton of cementitious product was 633 kg, a decline of 16% since 1990 (Klee, Hunziker, van der Meer, & Westaway, 2011). This improvement in efficiency is exceeded by the growth in demand (as can be seen in Figure 59).

The total amount of greenhouse gas emissions as a result of cement production has grown the most relative to other industries, as can be seen in Figure 59.

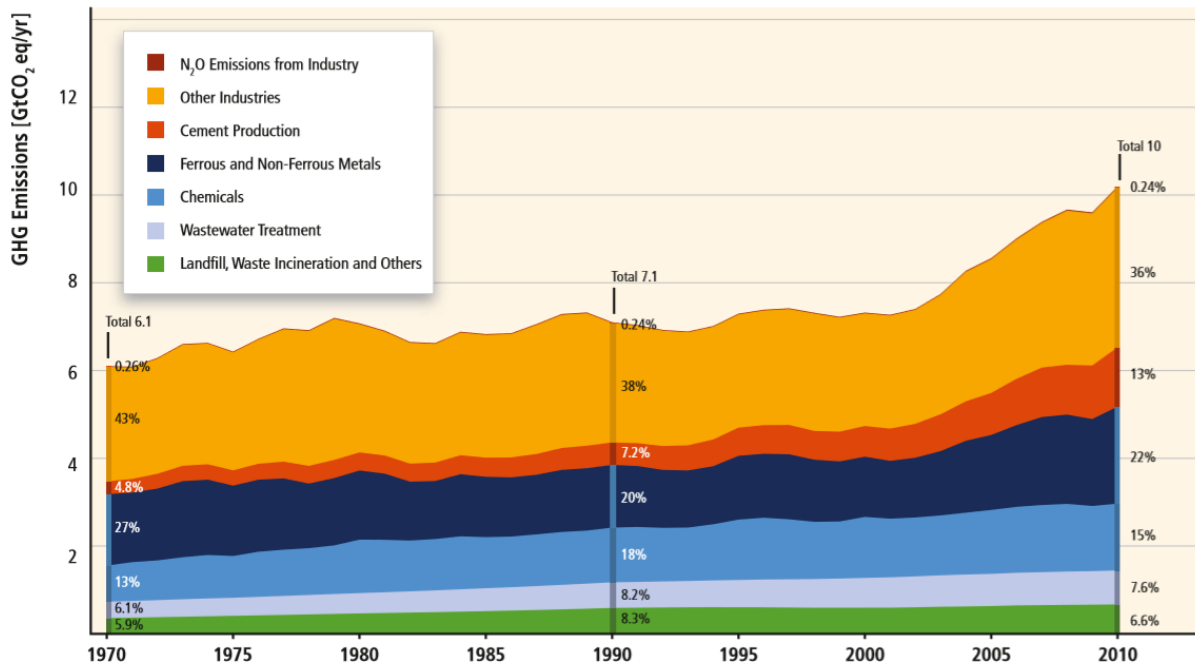


Figure 59. Greenhouse gas emissions per industry. (1970-2010) (UNEP; WMO, 2014).

It is clear that the footprint of the cement industry is significant. In the Netherlands relative large amount of blast furnace slag cement is used as (partly) substitution to ordinary Portland cement, this decrease the environmental footprint.

However, to reach the set Sustainable Development Goals there is still a lot to be done. Research to concrete structures and improving their design is a method of reducing the concrete needed.

Appendix C

In this appendix the theory behind Fick's laws of diffusion is explained.

Fick's 2nd law:

$$\frac{\partial H}{\partial t} = \frac{\partial}{\partial x} \left(D(H) \frac{\partial H}{\partial x} \right) \quad (1)$$

Fick's 1st law:

$$J = f * (\varphi_s - \varphi_{en}) \quad (2)$$

Fick's 2nd law.

Fick developed two laws that describe flux and diffusion of mass through a medium. These are analogous to the heat equation, or Fourier's law of heat conduction. Difference in these equations is the flux type the equation describes (Van den Akker & Mudde, 2014).

There exist two methods to derive the formula's. First one is based on the theory of the divergence theorem and continuity. Second method is to derive the formula analytically by analysing a graphical representation of a flux, this way first the 1st law of Fick is derived followed by the 2nd law.

Both methods are based on the conservation of mass principle. In a system the change inside the volume being analysed is equal to the change through the boundary of the system.

This theory, also known as Gauss's theorem or Green's theorem for 2D analysis, is based on vector calculus and states that the flux through a surface is equal to the volume integral of the divergence over the region inside the surface. The flux of the surface is the surface integral of a vector field in normal direction n over the closed surface.

This theorem is based on three dimensions and suitable for fluid dynamics (Strang & Herman, 2018).

Formula (3) hold the mathematical notation of the divergence theorem. In which, V is the body volume, S the piecewise smooth boundary of the body surface and \vec{F} is the continuously differentiable vector field.

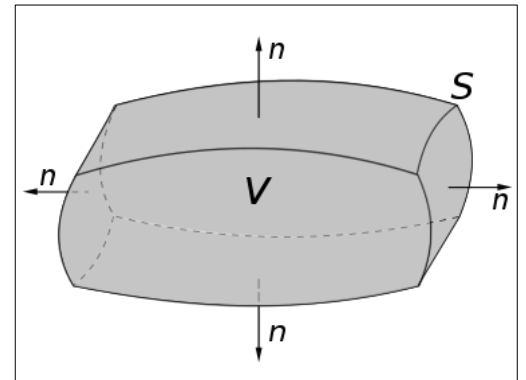


Figure 60. A volume V bounded by the surface S and the surface normal n .

$$\iiint_D \text{div}(\vec{F}) dV = \oiint_S \vec{F} \cdot \hat{n} dS \quad (3)$$

The right-hand-side of this equation, the surface integral can also be written as:

$$\oiint_S \vec{F} \cdot \hat{n} dS = \oiint_S \mathbf{j} dS \quad (4)$$

with flux \mathbf{j} of quantity q flowing through imaginary surface S

In this thesis the heat equation is used which is analogue to mass equation for fluids. Both equations have a concentration gradient which is multiplied with a (non-linear) coefficient. For these cases the vector field is the temperature flux in heat equation or flux of water for this thesis.

Regarding the amount of water in diffusion dynamics the variable is:

$$u = \text{concentration of quantity at given point } (x, y, z, t)$$

making the flux:

$$\mathbf{j} = C\mathbf{u} \quad (5)$$

C = amount of quantity q per unit. Being the water density at each point.

\mathbf{u} = velocity field of the relevant flow.

Goal is to get the equation which describes the change of water concentration over time for a change in space. The divergence theorem with continuity equation will lead to following partial differential equation:

$$\frac{\partial c}{\partial t} + \nabla \cdot \mathbf{j} = R \quad (6)$$

∇ = divergence.

t = time in seconds

R = source or sink. (The generation or destruction of q per unit time.)

This differential form is similar to the convection-diffusion equation. In this thesis the formula used for diffusion of internal moisture is kept separate from convection, hence: surface evaporation. The convection-diffusion equation can be derived from the differential equation (6).

With flux \mathbf{j} and R being the net volumetric source or sink for c . The flux can be divided into two types, diffusive flux and advective flux. The diffusive flux as a result of diffusion is known as Fick's first law for mass flux:

$$\mathbf{j}_{\text{diff}} = -D\nabla c \quad (7)$$

The diffusive flux is proportional to the concentration gradient. D is diffusion coefficient in (m^2/s).

secondly there is de advective flux:

$$\mathbf{j}_{\text{adv}} = \mathbf{v}c \quad (8)$$

making the total flux:

$$\mathbf{j}_{\text{total}} = \mathbf{j}_{\text{diff}} + \mathbf{j}_{\text{adv}} = -D\nabla c + \mathbf{v}c \quad (9)$$

Implementing flux (9) in equation(6):

$$\frac{\partial c}{\partial t} = \nabla \cdot (D\nabla c - \mathbf{vc}) + R \quad (10)$$

In chapter 63 of the DIANA 10.2 manual, background theory to the 'Potential Flow Analysis' is given. Starting with the general convection-diffusion equation towards the finite element implementation of this theory using the before mentioned Gauss or Divergence Theorem.

The general equation for convection-diffusion is compared to the used equation for transient heat analysis in DIANA FEA (DIANA - Finite Element Analysis, n.d.).

Convection-diffusion equation

$$\frac{\partial c}{\partial t} = \nabla \cdot (D\nabla c - \mathbf{vc}) + R \quad (10)$$

c = concentration
t = time
D = diffusion coefficient
 \mathbf{vc} = convective flux
R = source or sink

Energy balance equation

$$c \frac{\partial T}{\partial t} = \text{div}(k \vec{\text{grad}} T + \vec{\mathbf{v}}T) + q_v \quad (11)$$

c = thermal capacity
T = temperature
t = time
k = thermal conductivity
 $\vec{\mathbf{v}}T$ = convective flux
 q_v = source or sink

In the diffusion part of the analysis performed in this research the convective flux is left out of consideration. As this is solely done in the boundary flow elements at the surface of the model. Sources or sinks are not present in the model. The internal relative humidity is being simulated. This has an initial value, which is different than the environmental or external relative humidity. During the simulation no additional moisture is being inserted or extracted directly from the concrete. When the convective part and source part are excluded from the calculation, the formulas (10) and (11) will change to (12) and (13).

Convection-diffusion equation
no convection, no source

$$\frac{\partial c}{\partial t} = \nabla \cdot (D\nabla c) \quad (12)$$

c = concentration (kg/m³)
t = time (s)
D = diffusion coefficient (m²/s)

Energy balance equation
no convection, no source

$$c \frac{\partial T}{\partial t} = \text{div}(k \vec{\text{grad}} T) \quad (13)$$

c = thermal capacity (J/m³K)
T = temperature (K)
t = time (s)
k = thermal conductivity (W/mK)

The now found diffusion equation is valid for unsteady-state conditions. Describing concentration profiles over time. As stated in the 'Transport phenomena' by Akker, equation 4.43 (Van den Akker & Mudde, 2014).

For two sided diffusion the concentrations profiles of a certain quantity over time will evolve as in Figure 61. At t_0 the whole section has a concentration equal to C_{A_0} . In equilibrium at t_∞ the full section has a concentration equal to the externally exerted concentration level C_{A_1} .

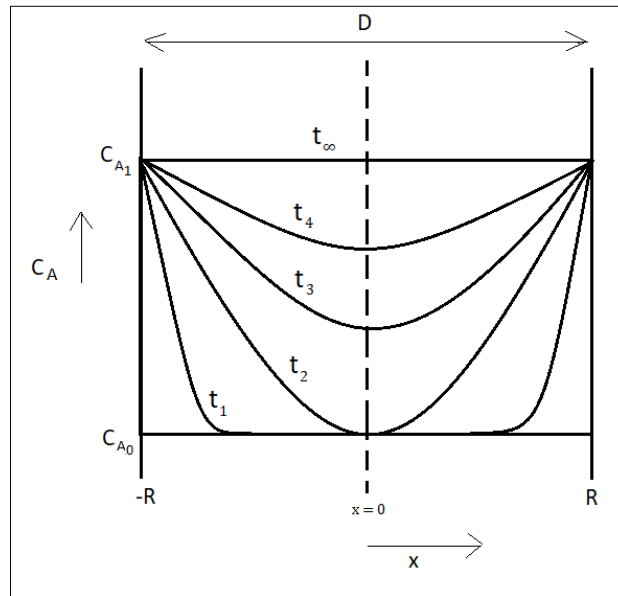


Figure 61. Cross-sectional distribution of temperature or moisture due to diffusion over time.

the unsteady diffusion equations hold:

$$\frac{\partial c_A}{\partial t} = D \frac{\partial^2 c_A}{\partial x^2} \quad (14)$$

This is Fick's second law. As used to describe moisture diffusion in concrete by Holmes and West (Holmes & West, 2003). In their work they refer to the mathematical formulation by J. Crank (Crank, 1979).

The formula is a simplification of the full equation into a one directional field.

$$\frac{\partial c}{\partial t} = D \left(\frac{\partial^2 c}{\partial x^2} + \frac{\partial^2 c}{\partial y^2} + \frac{\partial^2 c}{\partial z^2} \right) \quad (15)$$

Concrete pores have an internal relative humidity (RH). The diffusion coefficient is dependent of this RH. Making the 2nd equation of Fick:

$$\frac{\partial RH}{\partial t} = \frac{\partial}{\partial x} \left(D(RH) \frac{\partial RH}{\partial x} \right) \quad (16)$$

- $RH = \text{Relative Humidity}$ (-)
- $t = \text{time}$ (s)
- $x = \text{distance}$ (m)
- $D(RH) = \text{diffusion coefficient}$ (m^2/s)

Analytical derivation

The laws of mass transfer based on diffusion can be derived by analysing the graphical representation of change in concentration over space and time.

In the graph in Figure 62, there is a difference in concentration over Δx . This will start a flux, flow of particles, in the direction of the concentration difference. Flux is directed from high to the low concentration. The flux is directly proportional to the concentration gradient by the diffusion coefficient. As in formula (17).

$$\text{Fick's 1st law} \quad J_x = -D \frac{dc}{dx} \quad (17)$$

The flux is Fick's first law, taking into account the change of the flux over time results in Fick's second law.

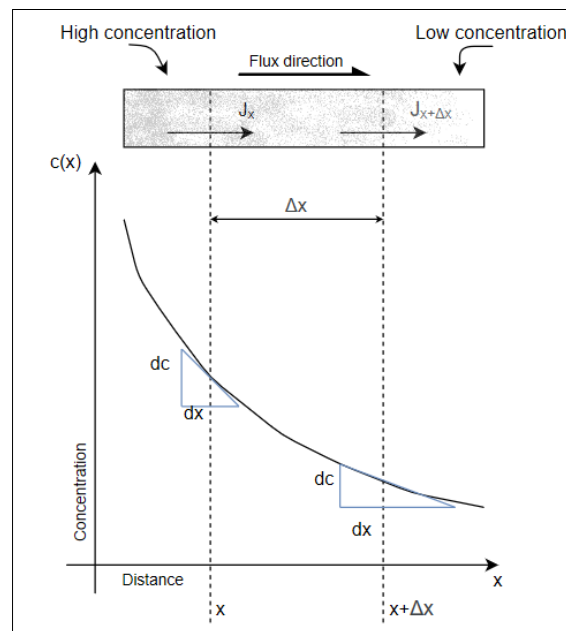


Figure 62. Flux due to differences in concentration

Mass entering volume $\Delta V (= A\Delta x)$ at x in time interval Δt :

$$m_x = J_x \cdot A \cdot \Delta t$$

Mass leaving ΔV at $x + \Delta x$ at time interval Δt :

$$m_{x+\Delta x} = J_{x+\Delta x} \cdot A \cdot \Delta t$$

Mass accumulating:

$$\Delta m = m_x - m_{x+\Delta x}$$

$$\Delta m = J_x A \Delta t - J_{x+\Delta x} A \Delta t = (J_x - J_{x+\Delta x}) \cdot A \Delta t = -(J_{x+\Delta x} - J_x) \cdot A \Delta t$$

$$\Delta m = -\Delta J A \Delta t$$

Concentration change in volume ΔV over time Δt :

$$\Delta c = \frac{\Delta m}{\Delta V} = -\frac{\Delta J A \Delta t}{A \Delta x} = -\frac{\Delta J}{\Delta x} \cdot \Delta t$$

$$\frac{\Delta c}{\Delta t} = -\frac{\Delta J}{\Delta x} \text{ setting the increment close to zero}$$

$$\lim_{\Delta t \rightarrow 0} \left(\frac{\Delta c}{\Delta t} \right) = -\lim_{\Delta x \rightarrow 0} \left(\frac{\Delta J}{\Delta x} \right) \Rightarrow \frac{\partial c}{\partial t} = -\frac{\partial J}{\partial x}$$

Now we replace J by Fick's first law, see equation (17).

$$\frac{\partial c}{\partial t} = -\frac{\partial}{\partial x} \left(-D \frac{dc}{dx} \right) = \frac{\partial}{\partial x} \left(D \frac{dc}{dx} \right)$$

resulting in the 2nd law:

$$\text{Fick's 2nd law} \quad \frac{\partial c}{\partial t} = \frac{\partial}{\partial x} \left(D \frac{dc}{dx} \right) \quad (18)$$

The here derived formula (18) is equal to the derivation which led to equations (1), (12), (15) and (17).

Concerning diffusion of mass a unit check is performed.

$$c = \text{mass (capacity)} \text{ (kg/m}^3\text{)}$$

$$t = \text{time (s)}$$

$$x = \text{distance (m)}$$

$$D = \text{diffusion coefficient (m}^2\text{/s)}$$

$$\frac{\text{kg/m}^3}{\text{s}} = \frac{1}{\text{m}} \left(\frac{\text{m}^2}{\text{s}} \cdot \frac{\text{kg/m}^3}{\text{m}} \right) \Rightarrow \frac{\text{kg/m}^3}{\text{s}} = \frac{\text{kg/m}^3}{\text{s}}$$

When using relative humidity, the unit check holds:

$$c = \text{mass (capacity)} \text{ (kg/m}^3\text{)}$$

$$t = \text{time (s)}$$

$$x = \text{distance (m)}$$

$$D = \text{diffusion coefficient (m}^2\text{/s)}$$

$$\frac{(-)}{\text{s}} = \frac{1}{\text{m}} \left(\frac{\text{m}^2}{\text{s}} \cdot \frac{(-)}{\text{m}} \right) \Rightarrow \frac{1}{\text{s}} = \frac{1}{\text{s}}$$

Appendix D

Crack formation in FEM

A structure can have internal tensile stresses as a result of being loaded by shrinkage, tensile forces or bending moments. Cracks occur when the tensile strength is exceeded by the tensile stress. This can happen on a local scale. In this case, (micro)cracks arise on the point of high tensile stresses. Local material imperfections are prone to initiate a crack. Once a crack is formed, deformation will concentrate there and the crack will propagate.

In this appendix the material properties of concrete are described. The formation of cracks can be formulated in finite element modelling. Two main models to describe the crack behavior are substantiated, being the *smear-* and *total strain cracking model*.

Concrete is a quasibrittle material with a fracture behaviour partly determined by its structural size, aggregate content and aggregate size (Zdeněk P. Bažant & Oh, 1983). When a structure becomes relatively large compared to the material inhomogeneities, the structure becomes perfectly brittle. On the other hand, when a structure is relatively small, the zone in which fracture process takes place can include the full cross section. In this situation the material is regarded non-brittle (Mier, 2013).

Once a crack is formed, the stress and strain values will change. Crack propagation in reinforced concrete is characterised by tension softening. Tension softening is the opposite mechanism of tension hardening. These mechanisms describe the development of the stress-strain curve, an important indicator of the crack development. Whereas perfect brittle material has no residual strength at the moment the tensile strength is reached. Reinforced concrete can show a residual stress-strain behaviour. This is strongly influenced by presence of reinforcement in the shape of bars or fibres.

The ductile behaviour can be modelled with a (bi)linear or non-linear descending part, describing the tension-softening. In the finite element analysis software DIANA, multiple stress-strain relations are possible to model. Depending on the constitutive model used for determining the total strain. The Model code 2010 uses a multi-linear model in their total strain crack model approach.

The influence of shrinkage by drying on tension softening has been researched in 1988 by Thelandersson et al., They discovered that the softening region grows inwards from the beginning and tends to not last over the entire drying time. "Affected regions are subsequently unloaded and cracks are closing" (Thelandersson, Martensson, & Dahlblom, 1988). It is likely they witnessed a delayed hardening of these regions in combination with creep and relaxation.

To include crack formation in a general Finite Element (FE) model, a predefined crack model needs to be used. In previous research, a multi-directional fixed crack model was used (Tiberti et al., 2018). In this type of model, every crack has a coordinate system aligned with the crack direction.

The latter mentioned crack model is categorized as a *smeard cracking model*. It is based on the decomposition of the total strain (ε) in an elastic strain (ε^e) and a crack strain (ε^{cr}), within the discontinuity area (Rots, 1988)(DIANA - Finite Element Analysis, 2017).

Publication by the Civil Engineering Department of the University of Porto, suggests that the smeared crack model can be used on concrete slabs submitted to point loads resulting in punching shear (Moreno & Sarmiento, 2013). Their statement is based on the concept of strain decomposition (SD) and total strain with fixed orthogonal cracks approach (TSF).

This approach of crack modelling was successfully applied by Tiberti et al., for a numerical parametric study focussed on shrinkage cracking in slabs-on-grade (Tiberti et al., 2018).

In combination with bi-linear tension-softening for post-cracking behaviour.

However, their study includes simplifications of true concrete and cement mechanics. Creep and relaxation effects were not included. The deformations due to shrinkage were fixed in advance, based on the Eurocode calculation.

Another type of model is the *total strain cracking model*. This stress-strain relation is analysed in detail by Vecchio and Collins in 1986 (Vecchio & Collins, 1986).

The type of model can be subdivided into a rotational model or a non-rotational model. Regarding a slab floor, in which cracks are propagating predominantly in transverse direction, a non-rotational model could be opted for. This is sufficient over the more computational expensive rotational model and could be used when modelling the slab as shell elements. Shell element further reduce computational time compared to solid elements, having more integration nodes. The used elements in this research are motivated in part [5.1 Model setup](#).

The total strain crack model is based on fracture energy. Fracture energy is the total of potential energy, stored in the strained system under tensile stress. This energy is equal to the area under the trajectory of the stress-strain graph. The amount of energy defines the trajectory of the tension-softening part.

The fracture process zone, is a zone in which the maximum stress is decreasing and the maximum strain is increasing. These are located at. These microcracks are mechanisms at micro-level, which do not necessarily coincides with the effect at macroscopic level. Internal restraints form hotspots for microcracks. This is explaining the complex relation between cement paste shrinkage and concrete shrinkage.

Appendix E

Analogy between the moisture evaporation at the concrete surface and the surface discharge of heat by convective flow is explained. This is done by comparing the equation and units.

both equations are composed of a coefficient, or rate, stating the speed of the exchange, multiplied with the differences in concentrations.

Equations

Heat flow, surface convection:

Convective discharge at a boundary flow element is calculated in the used transient heat analysis. See chapter 46.2.1 in the DIANA FEA 10.2 manual. (DIANA - Finite Element Analysis, 2017)

Main parameter: h Heat transfer coefficient ($W/m^2 \cdot K$)

$$q_c = -h(T_b - T_E)^N$$

q_c = convective discharge
 h = heat transfer coefficient
 T_B and T_E = Temperature at boundary and environmental temperature
 N = Convective power (=1)

Moisture flow, surface evaporation:

Main parameter: f Surface evaporation rate ($kg/m^2 \cdot s$)

$$J_s = f * (\varphi_s - \varphi_{en})$$

J_s = Surface moisture flux
 f = Surface evaporation rate
 φ_s and φ_{en} = Surface relative humidity and environmental relative humidity

Units

Heat flow:

$$q_c = -h(T_b - T_E)^N \rightarrow \frac{W}{m^2} = -\frac{W}{m^2 \cdot K} (K - K)^1 = -\frac{J}{s \cdot m^2 \cdot K} (K - K)^1 = -\frac{J}{s \cdot m^2} = \frac{W}{m^2}$$

Moisture flow:

In the FEM model outcome the relative humidity (RH) is temperature (K) and mass (kg) is joule (J). Analogy is shown by using the rate of surface evaporation as heat transfer coefficient, $f = h$.

$$J_s = f * (\varphi_s - \varphi_{en}) \rightarrow \frac{kg}{m^2 \cdot s} = \frac{kg}{m^2 \cdot s} (RH - RH)$$
$$\text{in Diana} \rightarrow \frac{W}{m^2 \cdot K} (K - K) = \frac{J}{m^2 \cdot s} \text{ with } J = kg \rightarrow J_s = \frac{kg}{m^2 \cdot s}$$

Based on these derivations, the surface moisture flux can be determined using the transient heat analysis. For this, the value of the surface evaporation rate should be given to the heat transfer coefficient.

Appendix F

Difference method

The method of Binder-Schmidt, as suggested by Breugel, is based on a finite difference method (K. van Breugel et al., 1996). In finite difference, the value of a certain point at a certain moment in time, is found by averaging the values of the adjacent integration points. The integration points are the result of discretization of the element.

A common finite difference method is the 'Forward-Time Central-Space' method (FTCS-method) (Reybrouck et al., 2009).

For an discretized element in one dimensional(1D) space, the finite difference FTCS-method in formula form is:

$$\frac{u(x, t + \Delta t) - u(x, t)}{\Delta t} = D \frac{u(x + \Delta x, t) - 2u(x, t) + u(x - \Delta x, t)}{\Delta x^2}$$

This can be rewritten to:

$$u(x, t + \Delta t) = u(x, t) + \frac{D\Delta t}{\Delta x^2}(u(x + \Delta x, t) - 2u(x, t) + u(x - \Delta x, t))$$

Based on linear algebra notation, the formula is written as:

$$u_{i,j+1} = u_{i,j} + r(u_{i+1,j} - 2u_{i,j} + u_{i-1,j}) \quad \text{Illustration of the coordinates is show in Figure 63.}$$

For stability of the solution: $r = \frac{D\Delta t}{\Delta x^2} < \frac{1}{2}$ (for 1D problem) gives $\Delta t \leq \frac{\Delta x^2}{2D}$

When the time steps (Δt) are too large, no stable solution can be found.

This same method is used by Reybrouck et al. in their study to shape correction factors, based on numerical analysis of drying concrete (Reybrouck et al., 2009).

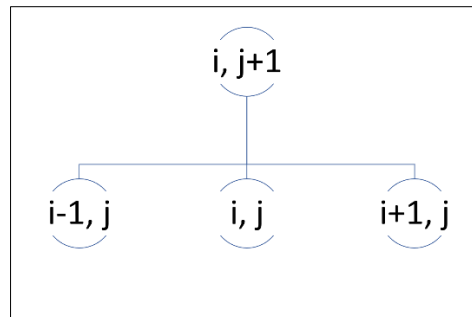


Figure 63. Finite difference method for numerical analysis

for solving $u_t = Du_{xx} + Du_{yy}$ in two dimensional(2D) space the discretization is:

$$u_{i,j,k+1} = u_{i,j,k} + r(u_{i+1,j,k} - 2u_{i,j,k} + u_{i-1,j,k}) + r(u_{i,j+1,k} - 2u_{i,j,k} + u_{i,j-1,k})$$

with $r = \frac{D\Delta t}{\Delta x^2} < \frac{1}{4}$ (for 2D problem) gives $\Delta t \leq \frac{\Delta x^2}{4D}$ for $\Delta x = \Delta y$

Appendix G

In Figure 64 the effect of mesh refinement is seen in the outcome of the RH-simulation. The result for time-step 1 (time= 1 hour) are shown.

When the mesh-size is set to 0.0015 m , the mesh does not influence the outcome of the simulation. The result of the RH-simulation for multiple time-steps is seen on the next page in Figure 65 till Figure 68.

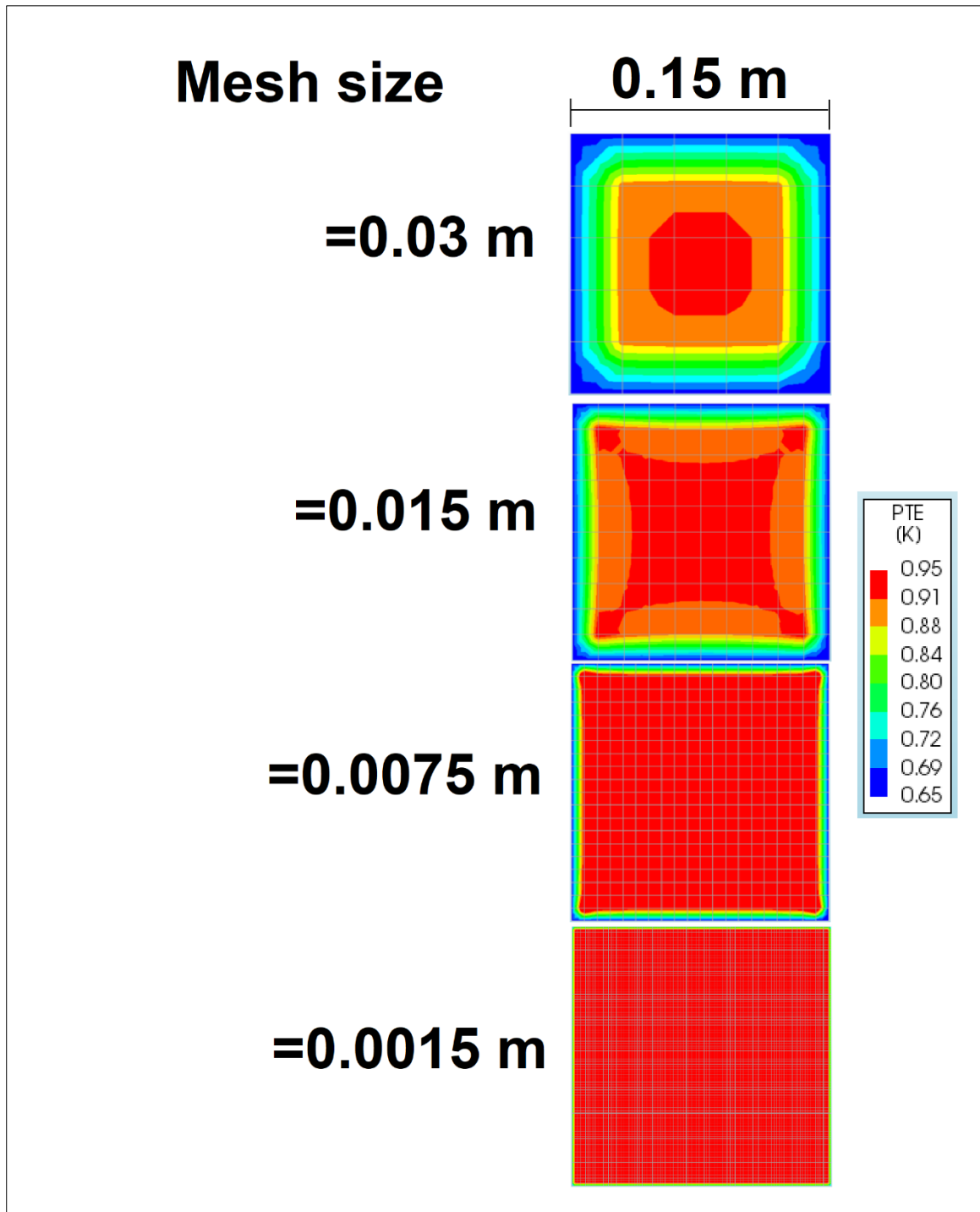


Figure 64. Mesh optimisation.

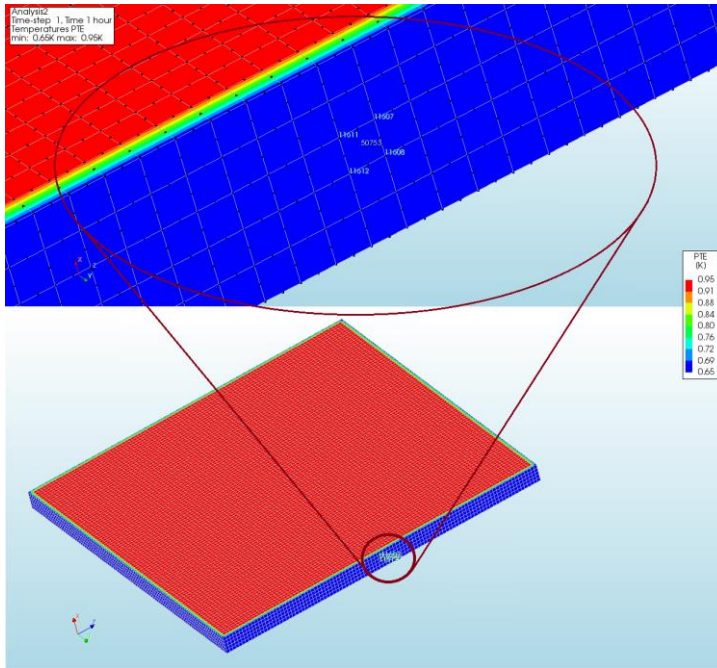


Figure 65. $t=1$ hour

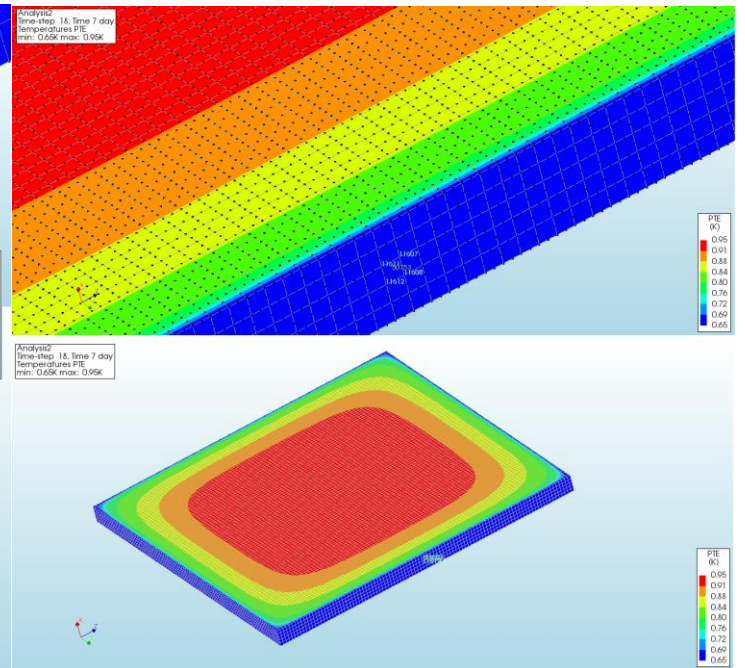


Figure 66. $t=7$ days

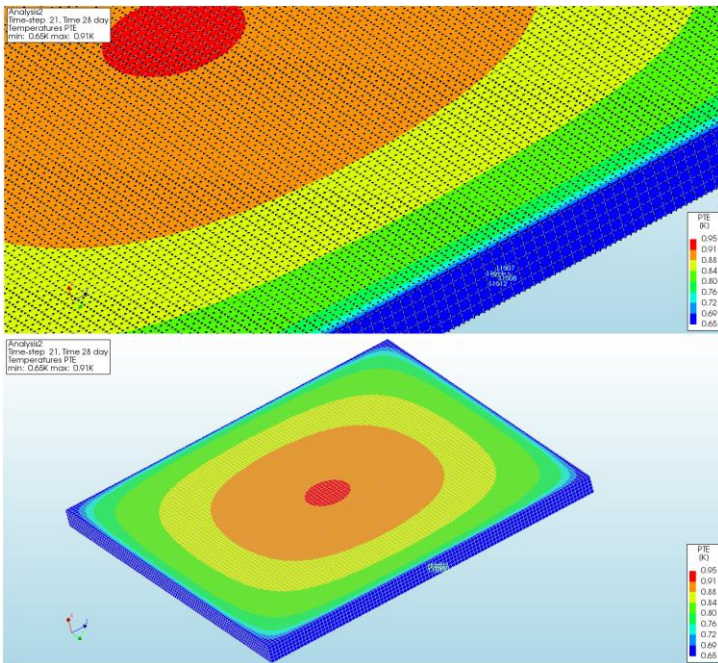


Figure 67. $t=28$ days

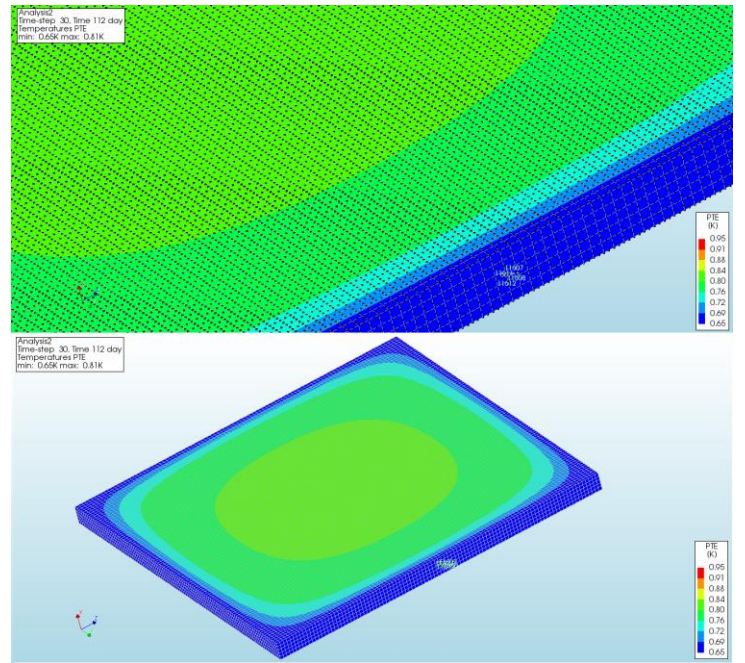


Figure 68. $t=112$ days

Appendix H

Figure 69, the result of the Finite Element simulation of the *test beam* is seen. This screenshot of DIANA FEA shows the temperature distribution over time, for 100 nodes. As explained in chapter 5, the relative humidity is modelled as a temperature [K]. This graphical result is based on a simulation with an initial internal RH-level of 95% and an ambient RH-level of 65%. The nodes are positioned on the straight line crossing the 150 mm thick concrete specimen, see Figure 71. By symmetry, two nodes at the same distance of the centre have the exact same result.

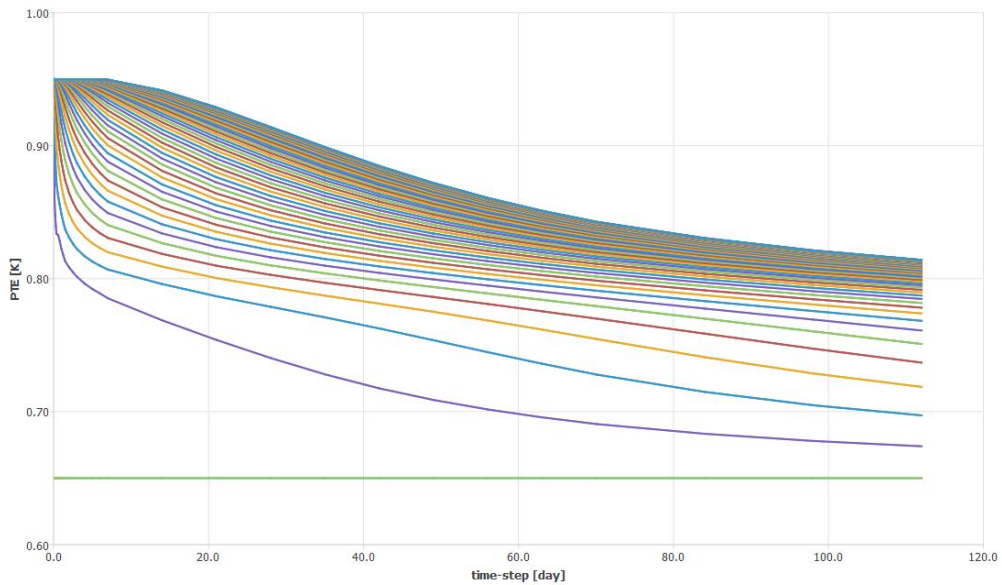


Figure 69. Temperature distribution at cross-sectional nodes. The nodes are located on the straight section-cut as seen in Figure 71 (top).

Four representative nodes are determined based on the average value at multiple moments in time. A graph showing the results of these nodes is seen in Figure 70. These nodes are at the surface, centre and two nodes as average on a straight cut through the model and a diagonal cut.

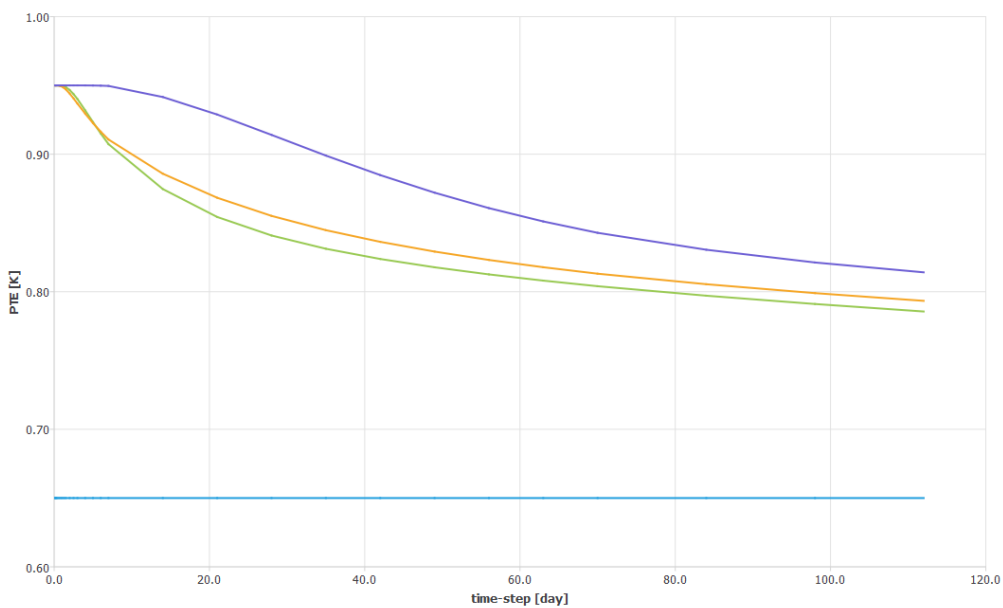
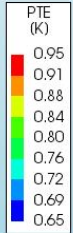
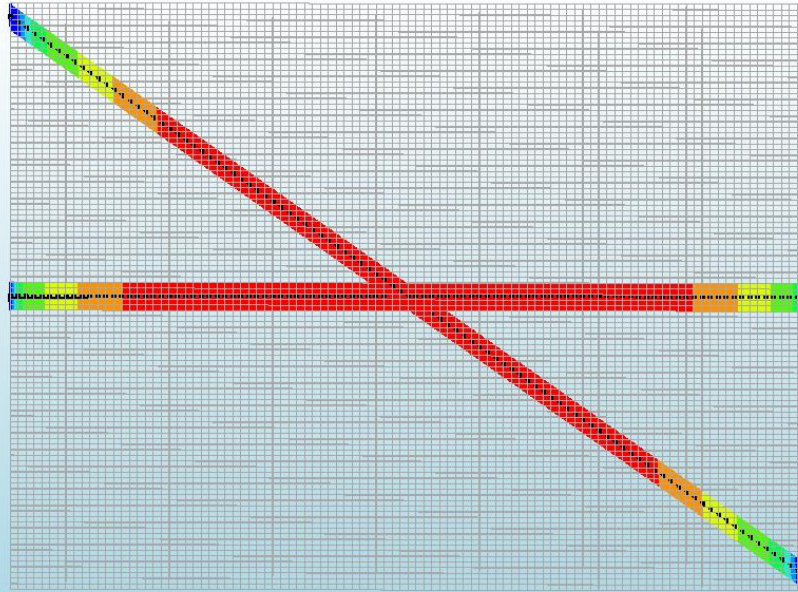


Figure 70. Temperature distribution at mean nodes on cross-sections.

The position of the mean nodes is illustrated on the next page.

Analysis2
 Time-step 17, Time 6 day
 Temperatures PTE
 min: 0.65K max: 0.95K



Analysis2
 Time-step 17, Time 6 day
 Temperatures PTE
 min: 0.65K max: 0.95K

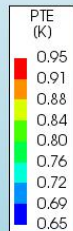
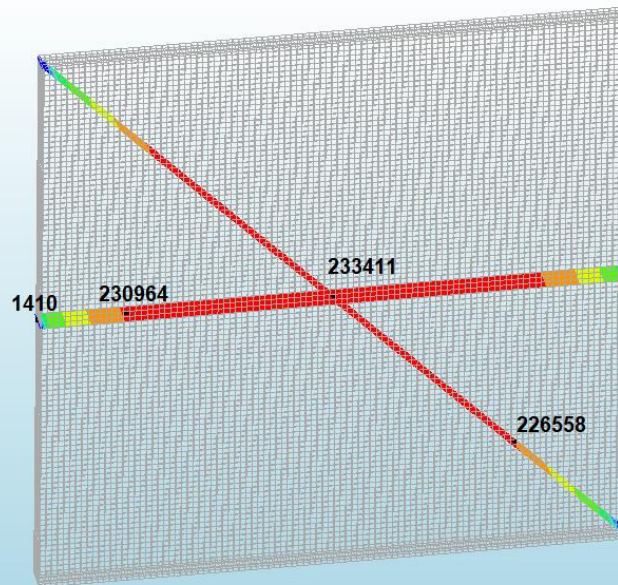


Figure 71. Position of nodes on the straight- and diagonal-cross-section.
 top) All nodes on the cutting-plane, middle element on the plane is used.
 bottom) Position of the four mean nodes used to illustrate the mean distribution of relative humidity through the cross section.

The general average RH of the cross section is the average of the two mean nodes 230964 and 226558. This values is used to calculated the drying shrinkage strain over time.

This 'slab' shaped model represents a slice of a the concrete *test beam*. Contact with the ambient environment is only present at the outer surfaces of the model.
 The mean nodes are chosen on the middle of the visible section cuts. However, due to the latter mentioned reason, results are the same when positioned at the slice surface (this is the surface not modelled to ambient exposure)

Appendix I

```
'MATERI'  
1 NAME "cementpasta transient "  
  MCNAME CONCR  
  MATMDL LEI  
  YOUNG 3.00000E+10  
  POISON 2.00000E-01  
  DENSIT 1.00000E+03  
  ASPECT HEATFL THERMA  
  CONDUCT 2.50000E-08  
  CAPACI 7.50000E+01  
  TEMCND 6.50000E-01 1.26000E-09 6.60000E-01 1.26000E-09  
    6.70000E-01 1.26000E-09 6.80000E-01 1.27000E-09  
    6.90000E-01 1.28000E-09 7.00000E-01 1.30000E-09  
    7.10000E-01 1.34000E-09 7.20000E-01 1.40000E-09  
    7.30000E-01 1.51000E-09 7.40000E-01 1.71000E-09  
    7.50000E-01 2.06000E-09 7.60000E-01 2.70000E-09  
    7.70000E-01 3.85000E-09 7.80000E-01 5.84000E-09  
    7.90000E-01 8.96000E-09 8.00000E-01 1.31000E-08  
    8.10000E-01 1.75000E-08 8.20000E-01 2.09000E-08  
    8.30000E-01 2.31000E-08 8.40000E-01 2.42000E-08  
    8.50000E-01 2.47000E-08 8.60000E-01 2.49000E-08  
    8.70000E-01 2.50000E-08 8.80000E-01 2.50000E-08  
    8.90000E-01 2.50000E-08 9.00000E-01 2.50000E-08  
    9.10000E-01 2.50000E-08 9.20000E-01 2.50000E-08  
    9.30000E-01 2.50000E-08 9.40000E-01 2.50000E-08  
    9.50000E-01 2.50000E-08  
2 NAME "cementpasta boundary"  
  MCNAME INTERF  
  MATMDL FLBOUN  
  FLUXTY CONVEC  
  CONPOW 1.00000E+00  
  CONVEC 3.00000E-01  
  ASPECT THERMA
```

```
MATERIAL 2  
'BOUNDA'  
CASE 1  
NAME "Ex Environment"  
ELEMEN  
/ "Boundary" /  
  EXTEMP 6.50000E-01  
'TIMEBO'  
BOUNDA 1  
TIMES 0.00000E+00 4.73040E+08 /  
FACTOR 1.00000E+00 1.00000E+00 /  
'INIVAR'  
TEMPER 1  
/ 1-233411 / 0.950000  
'END'
```

Appendix J

Table for the mean nodes used to export RH values out of the DIANA FEA model.

	Name of node	Node ID	x (m)	y (m)	z (m)
1	Upper bound avg.	230964	0.00375	0.0225	0.0750
2	Lower bound avg.	226558	0.00375	0.1215	0.0285
3	Surface	1410	0.00300	0.0000	0.0750
4	Centre	233411	0.00375	0.0750	0.0750

Table 10. Coordinates of mean nodes used for RH-distribution.

To make the data Microsoft Excel compatible, the following export commands are used to extrude the required data in a tabular format.

```
[ n1 ] = findNearestNodes( [ ( 0.00375, 0.0225, 0.075 ) ] )
exportResultsToCSV( "C:/Users/d.klusener/Documents/test
beam/V7_RH95_65_MC_n230964.csv",
    [ "Analysis2",
      "Analysis output",
      "Temperatures",
      "PTE" ],
    resultCases( "Analysis2", "Analysis output" ),
    [n1] )
```

```
[ n1 ] = findNearestNodes( [ ( 0.00375, 0.1215, 0.0285 ) ] )
exportResultsToCSV( "C:/Users/d.klusener/Documents/test
beam/V7_RH95_65_MC_n226558.csv",
    [ "Analysis2",
      "Analysis output",
      "Temperatures",
      "PTE" ],
    resultCases( "Analysis2", "Analysis output" ),
    [n1] )
```

```
[ n1 ] = findNearestNodes( [ ( 0.003, 0, 0.075 ) ] )
exportResultsToCSV( "C:/Users/d.klusener/Documents/test
beam/V7_RH95_65_MC_n1410.csv",
    [ "Analysis2",
      "Analysis output",
      "Temperatures",
      "PTE" ],
    resultCases( "Analysis2", "Analysis output" ),
    [n1] )
```

```
[ n1 ] = findNearestNodes( [ ( 0.00375, 0.075, 0.075 ) ] )
exportResultsToCSV( "C:/Users/d.klusener/Documents/test
beam/V7_RH95_65_MC_n233411.csv",
    [ "Analysis2",
      "Analysis output",
      "Temperatures",
      "PTE" ],
    resultCases( "Analysis2", "Analysis output" ),
    [n1] )
```